NATIONAL TECHNICAL UNIVERSITY OF ATHENS

SCHOOL OF CIVIL ENGINEERING

Department of Water Resources and Environmental Engineering

DIPLOMA THESIS

NATURAL VARIABILITY AND PERSISTENCE IN OCEANIC VARIABLES

EVANGELOS MOSCHOS

Supervisor: Demetris Koutsoyiannis
Professor, NTUA

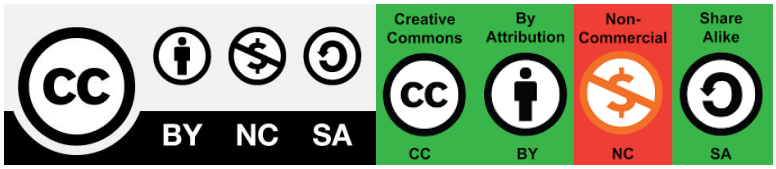

"Κόσμον τόνδε, τὸν αὐτὸν ἁπάντων,
οὔτε τις θεῶν οὔτε ἀνθρώπων ἐποίησεν,
ἀλλ᾽ ἦν ἀεὶ καὶ ἔστιν καὶ ἔσται πῦρ ἀείζωον
ἁπτόμενον μέτρα καὶ ἀποσβεννύμενον μέτρα".

Ηράκλειτος, Απόσπασμα Β30

That which always was,
and is, and will be everlasting fire,
the same for all, the cosmos,
made neither by god nor man,
replenishes in measure
as it burns away.

Heraclitus, Fragment B30

Translated by Brooks Haxton

This page is intentionally left blank

Abstract

Long records and reconstructions of oceanic variables as the Sea Level (SL) and the Sea Surface Temperature (SST) portray the intrinsic variability they inhibit through multiple time scales. In this study we examine the Long Term Persistence (or Long Range Dependence) that these variables exhibit by using observed and reconstructed proxies on time scales spanning from 1 month to 10 million years. We also associate their variability with periodic or oscillation processes such as the Milankovitch cycles for the SL variable and the ENSO phenomenon for the SST variable. Simple and parsimonious tools derived from Stochastic Methods, such as the climacogram and the Hurst exponent, which can be easily reproduced with basic elements of probabilities and statistics, are utilized for the purposes of this study.

Keywords:

Sea Level · Sea Surface Temperature · Natural Variability · Long Term Persistence · Hurst-Kolmogorov · Long Range Dependence · Stochastic Methods · Climacogram · Milankovitch Cycles · ENSO

This page is intentionally left blank

Εκτενής Περίληψη στα Ελληνικά
Extended Abstract in Greek

Η μεταβολή (ή «αλλαγή») των γεωφυσικών κλιματικών μεταβλητών είναι μια διεργασία που διεξάγεται από τη στιγμή της ύπαρξης του πλανήτη μας. Η μεταβολή αυτή λαμβάνει χώρα εντός πολλαπλών διακριτών κλιμάκων χρόνου, η οποία καθορίζει την μεταβολή που εμείς, ως ανθρώπινο είδος, ερχόμαστε να παρατηρήσουμε στην κλίμακα χρόνου που ορίζει η βιολογική και φυσικο-ιστορική μας υπόσταση. Η προσπάθεια μας να εκτιμήσουμε (ή να «προβλέψουμε») την μελλοντική εξέλιξη των φυσικών μεταβλητών αυτών, προκειμένου να κατανοήσουμε την συνολική εξέλιξη του κλιματικού συστήματος του πλανήτη μας, σκοντάφτει πολλές φορές πάνω στην εγγενή αβεβαιότητα που εμπεριέχεται στη μεταβολή που λαμβάνει χώρα εντός πολλαπλών κλιμάκων. Σε αντίθεση με την κοινά διαδεδομένη μεθοδολογία, που «χωρίζει» την εξέλιξη των διεργασιών σε ένα ντετερμινιστικό (ντετερμινιστικά προβλέψιμο) και ένα στοχαστικό («τυχαίο») μέρος, αντιμετωπίζουμε την αβεβαιότητα με στοχαστικό τρόπο, ως το όριο του ορίζοντα της πρόγνωσης, καθοριζόμενο από το χρονικό μήκος του ορίζοντα καθώς και την χρονική κλίμακα στην οποία εκτυλίσσεται η διεργασία.

Για να μπορέσουμε να εφαρμόσουμε αυτήν την λογική διερεύνησης σε δεδομένες παρατηρήσεις του φυσικού κόσμου, αξιοποιούμε τα πιθανοτικά εργαλεία των Στοχαστικών Μεθόδων καθώς και την έννοια της Μακροπρόθεσμης Εμμονής (Long Term Persistance – LTP). Οι πρώτες χρησιμοποιούν απλά και φειδωλά εργαλεία για την μοντελοποίηση τυχαίων μεταβλητών, μέσω του δείγματος παρατηρήσεων που είναι διαθέσιμες. Η δεύτερη, μας επιτρέπει την διερεύνηση της μακροπρόθεσμης δομής αυτό-συσχέτισης στην χρονική εξέλιξη μιας διεργασίας, δίνοντας σημαντικά στοιχεία για την εκτίμηση του ορίζοντα της αβεβαιότητάς της στην μελλοντική της εξέλιξη.

Σε αυτήν την εργασία, αξιοποιούμε την παραπάνω μεθοδολογία για την μελέτη καταγεγραμμένων και ανακατασκευασμένων παρατηρήσεων ωκεάνιων μεταβλητών όπως είναι η στάθμη της θάλασσας (Sea Level) και η επιφανειακή θαλάσσια θερμοκρασία (Sea Surface Temperature – SST). Μελετάμε παρατηρήσεις της χρονικής εξέλιξης των παραπάνω μεταβλητών μέσω δορυφορικών μετρήσεων αλλά και ανακατασκευασμένα παλαιοκλιματικά δεδομένα που αναπαριστούν την εξέλιξη των μεταβλητών εντός πολλαπλών χρονικών κλιμάκων.

Για την μελέτη των παραπάνω δειγμάτων χρησιμοποιούνται βασικές έννοιες, εξισώσεις και εργαλεία των στοχαστικών μεθόδων. Δίνονται οι ορισμοί εννοιών όπως η τυχαία μεταβλητή και η στοχαστική διεργασία Στη συνέχεια αναφέρονται βασικές έννοιες των πιθανοτήτων και της στατιστικής οι οποίες χρησιμοποιούνται για την περιγραφή της δομής μιας στοχαστικής διεργασίας. Οι συναρτήσεις της συνδιασποράς (εξ a.1) και της αυτοσυσχέτισης (εξ a.2) είναι δύο εξ' αυτών που χρησιμοποιούνται κατά κόρον στην μεθοδολογία της εργασίας.

$$Var\left(\underline{x}(t)\right) = C(t,t) = E\left[\left(\underline{x}(t) - \mu_x(t)\right)^2\right] \qquad (a.1)$$

$$\rho(t_1,t_2) = \frac{C(t_1,t_2)}{\sqrt{C(t_1,t_1)}\sqrt{C(t_2,t_2)}} \quad with \quad |\rho(t_1,t_2)| \leq 1 \qquad (a.2)$$

Αναλύονται δύο επιπλέον βασικές έννοιες, αυτές της στασιμότητας και της εργοδικότητας μιας στοχαστικής διεργασίας. Γίνεται η παραδοχή της ικανοποίησης του κριτηρίου τόσο της στασιμότητας όσο και της εργοδικότητας για τις στοχαστικές διεργασίες που αναλύονται στην παρούσα εργασία.

Το κλιμακόγραμμα, το βασικό εργαλείο που χρησιμοποιείται στην εργασία για τη μοντελοποίηση των χρονοσειρών, ορίζεται ως το γράφημα της διασποράς μιας στοχαστικής διεργασίας x(t), ως προς την χρονική κλίμακα k και συμβολίζεται με τον όρο $\gamma(k)$ (Koutsoyiannis 2013a). Το κλιμακόγραμμα είναι ένα ιδιαίτερα απλό, στη χρήση και στην αναπαραγωγή, εργαλείο, μέσω του οποίου είναι δυνατή η εκτίμηση της μακροπρόθεσμης εμμονής αλλά και της κυκλοστασιμότητας (ή περιοδικότητας) που εμπεριέχει μια διεργασία.

Το *εμπειρικό* κλιμακόγραμμα μπορεί να απεικονιστεί υπολογίζοντας την διασπορά (ή την τυπική απόκλιση) μιας χρονοσειράς, συναθροισμένης σε πολλαπλές κλίμακες k, για κάθε μια κλίμακα k, και εμφανίζοντας το διπλό λογαριθμικό διάγραμμα διασποράς-κλίμακας (ή τυπικής απόκλισης-κλίμακας). Το *θεωρητικό* κλιμακόγραμμα μιας στοχαστικής διεργασίας υπολογίζεται μέσω της εξίσωσης κλιμακογράμματος για την εκάστοτε διεργασία. Στη συνέχεια αναλύονται δύο βασικές κατηγορίες διεργασιών, οι διεργασίες Markov και οι διεργασίες Hurst-Kolmogorov, και ορίζονται οι εξισώσεις των θεωρητικών τους κλιμακογραμμάτων.

Η εξίσωση υπολογισμού του εμπειρικού κλιμακογράμματος μιας διεργασίας συναθροισμένης σε κλίμακα k δίνεται ως (Dimitriadis and Koutsoyiannis, 2015):

$$\gamma_k^{(\Delta)}(k) := \frac{Var\left[\sum_{l=k(i-1)+1}^{ki} \underline{x}_l^{(\Delta)}\right]}{k^2} = \frac{Var\left[\sum_{l=1}^{k} \underline{x}_l^{(\Delta)}\right]}{k^2} \qquad (a.3)$$

Οι διεργασίες Markov, αποτελούν κατηγορία διεργασιών στις οποίες το μέλλον δεν εξαρτάται από το παρελθόν, όταν το παρελθόν είναι γνωστό (Papoulis, 1991). Στοχαστικά μοντέλα που αντιστοιχούν σε διεργασίες Markov, όπως για παράδειγμα το μοντέλο AR(1) , λόγω του παραπάνω απλοποιητικού τους αξιώματος σε σχέση με την πραγματικότητα της φυσικής αλλαγής, δεν είναι δυνατόν να μοντελοποιήσουν τις φυσικές διεργασίες, ιδίως τη δομή αυτοσυσχέτισης που τις περιγράφει, παρά μόνο σε πολύ συγκεκριμένες απλοποιήσεις τους. Για να επιτευχθεί η μοντελοποίηση της μακροπρόθεσμης δομής αυτοσυσχέτισης που παρουσιάζουν οι φυσικές διεργασίες και δη οι κλιματικές, ορίζονται παρακάτω οι στοχαστικές διεργασίες Hurst-Kolmogorov.

Εν αντιθέσει με τις διεργασίες Markov, στις διεργασίες Hurst-Kolmogorov (HK), το μέλλον εξαρτάται από το καταγεγραμμένο παρελθόν. Ο μαθηματικός ορισμός αυτών των διεργασιών γίνεται μέσω της εξίσωσης του κλιμακογράμματος τους (εξίσωση α.4) (Koutsoyiannis 2016). Στην εξίσωση (α.4) οι συντελεστές λ και α αποτελούν αδιάστατους συντελεστές του κλιμακογράμματος, ενώ ο συντελεστής H που βρίσκεται στον εκθέτη της εξίσωσης ονομάζεται συντελεστής Hurst, και περιγράφει την μακροπρόθεσμη συμπεριφορά της δομής αυτοσυσχέτισης, αλλιώς την ύπαρξη εμμονής σε μια διεργασία, όπως περιγράφεται από το φαινόμενο Hurst.

$$\gamma(k) = \lambda(\alpha/k)^{2-2H} \qquad (a.4)$$

Ειδική μνεία γίνεται για το τελευταίο φαινόμενο αυτό το οποίο πήρε το όνομα του προς τιμήν του υδρολόγου Harold Edwin Hurst (1880-1978). Ο βρετανός υδρολόγος, με τη μελέτη της ιστορικής καταγραφής της στάθμης του Νείλου όρισε το φαινόμενο της μακροπρόθεσμης εμμονής σε μια φυσική διεργασία, που περιγράφεται μαθηματικά μέσω του συντελεστή Η.

Συγκεκριμένα οι διεργασίες κατηγοριοποιούνται με βάση την τιμή του συντελεστή Η ως εξής:

- Για Η=0.5 η διεργασία συμπεριφέρεται ως *λευκός θόρυβος*
- Για τιμές 0.5 < Η < 1 η διεργασία εμφανίζει μακροπρόθεσμη εμμονή (αλλιώς μακροπρόθεσμη εξάρτηση) και ονομάζεται *εμμονική διεργασία.*
- Για τιμές 0 < Η < 0.5 η διεργασία ονομάζεται *αντι-εμμονική διεργασία.*

Οι τιμές του συντελεστή Η, αναπαρίστανται από την κλίση του κλιμακογράμματος μιας χρονοσειράς, η οποία είναι 2-2Η, στην περίπτωση του κλιμακογράμματος διασποράς και 1-Η στην περίπτωση του κλιμακογράμματος τυπικής απόκλισης όπως φαίνεται και στην εξίσωση (Α2.2). Μια εμμονική διεργασία εμφανίζει θετική μακροπρόθεσμη αυτοσυσχέτιση, η οποία περιγράφει την χρονικά παράλληλη εμφάνιση των μέγιστων και ελάχιστων τιμών. Αυτό σημαίνει ότι μια υψηλή τιμή πιθανότατα θα ακολουθηθεί από μια άλλη υψηλή τιμή και οι επόμενες τιμές για ένα μεγάλο μελλοντικό χρονικό διάστημα θα τείνουν επίσης να είναι υψηλές. Στον αντίποδα, σε μια αντι-εμμονική διεργασία, μια υψηλή τιμή πιθανότατα θα ακολουθηθεί από μια χαμηλή, ενώ για ένα μεγάλο μελλοντικό χρονικό διάστημα θα τείνει να ακολουθείται αυτή η «αντιστροφή» μεταξύ υψηλών και χαμηλών τιμών. Μια διεργασία με Η=0.5 περιγράφει την πλήρη απουσία αυτοσυσχέτισης (λευκός θόρυβος). Στην πραγματικότητα, μια διεργασία με Η κοντά στην τιμή 0.5 μπορεί να εμφανίζει μη-μηδενικές τιμές του συντελεστή αυτοσυσχέτισης για πολύ μικρές τιμές βήματος (lag), η οποία όμως εκθετικά και γρήγορα θα τείνει να μηδενιστεί. Οι διεργασίες Markov, λειτουργούν κατά αυτόν ακριβώς τον τρόπο, επιτρέποντας να θεωρηθούν μια υποπερίπτωση των διεργασιών ΗΚ (Koutsoyiannis, 2002).

Έχοντας περιγράψει τις δύο παραπάνω κατηγορίες στοχαστικών διεργασιών, ορίζονται δύο στοχαστικά μοντέλα που απορρέουν αντίστοιχα από αυτές, για την παραγωγή συνθετικών χρονοσειρών[1]. Το μοντέλο AR(1), οι τιμές X_i του οποίου υπολογίζονται μέσω της εξίσωσης (α.5), αντιστοιχεί σε διεργασία Markov.

$$X_i = \rho X_{i-1} + V_i \qquad (\alpha.5)$$

όπου ρ ο συντελεστής αυτοσυσχέτισης πρώτης τάξης και V_i ένας τυχαίος λευκός θόρυβος.

Οι συνθετικές χρονοσειρές που παράγονται από το μοντέλο AR(1) διατηρούν τα στατιστικά χαρακτηριστικά πρώτου βαθμού της ιστορικής χρονοσειράς, καθώς και τον συντελεστή αυτοσυσχέτισης πρώτης τάξης. Αδυνατούν όμως να αναπαράξουν τη δομή αυτοσυσχέτισης για μεγαλύτερα χρονικά βήματα (lag), αλλά και για συνάθροιση της χρονοσειρά σε μεγαλύτερες από την κανονική της, χρονικές κλίμακες. Υπό αυτήν την έννοια το μοντέλο AR(1) αδυνατεί

[1] Συνθετικές ονομάζονται οι χρονοσειρές που έχουν παραχθεί από ένα στοχαστικό μοντέλο με βάση ένα καταγεγραμμένο δείγμα (ιστορική χρονοσειρά).

να αναπαράξει την μακροπρόθεσμη δομή αυτοσυσχέτισης της ιστορικής χρονοσειράς και για αυτό το λόγο, παρά την απλότητα του, κρίνεται ακατάλληλο για τη μοντελοποίηση των φυσικών διεργασιών.

Για να γίνει εφικτή η διατήρηση της μακροπρόθεσμης δομής αυτοσυσχέτισης και η αναπαράσταση του φαινομένου της μακροπρόθεσμης εμμονής, από παραχθείσες συνθετικές χρονοσειρές, χρησιμοποιείται το μοντέλο FGN (Fractional Gaussian Noise), που αποτελείται από ένα άθροισμα τριών διεργασιών AR(1). Ο υπολογισμός των τιμών W_i του μοντέλου γίνεται μέσω της εξίσωσης (α.6), όπου X_i^n οι τιμές των τριών μοντέλων (n=1,2,3) AR(1) και μ η μέση τιμή της ιστορικής χρονοσειράς, ενώ ο υπολογισμός του συντελεστή αυτοσυσχέτισης βήματος j και κλίμακας k γίνεται μέσω της εξίσωσης (α.7), για μικρές τιμές j -για μεγάλες τιμές εξ. 2.29 κύριας εργασίας- (Koutsoyiannis, 2002).

$$W_i = X_i^1 + X_i^2 + X_i^3 + \mu \qquad (a.6)$$

$$\rho_j^{(k)} = \rho_j = H(2H-1)j^{2H-2} \qquad (a.7)$$

Ο συντελεστής H της εξίσωσης (α.7) είναι ο συντελεστής Hurst της ιστορικής χρονοσειράς και χρησιμοποιείται για την αναπαραγωγή της μακροπρόθεσμης εμμονής της ιστορικής χρονοσειράς.

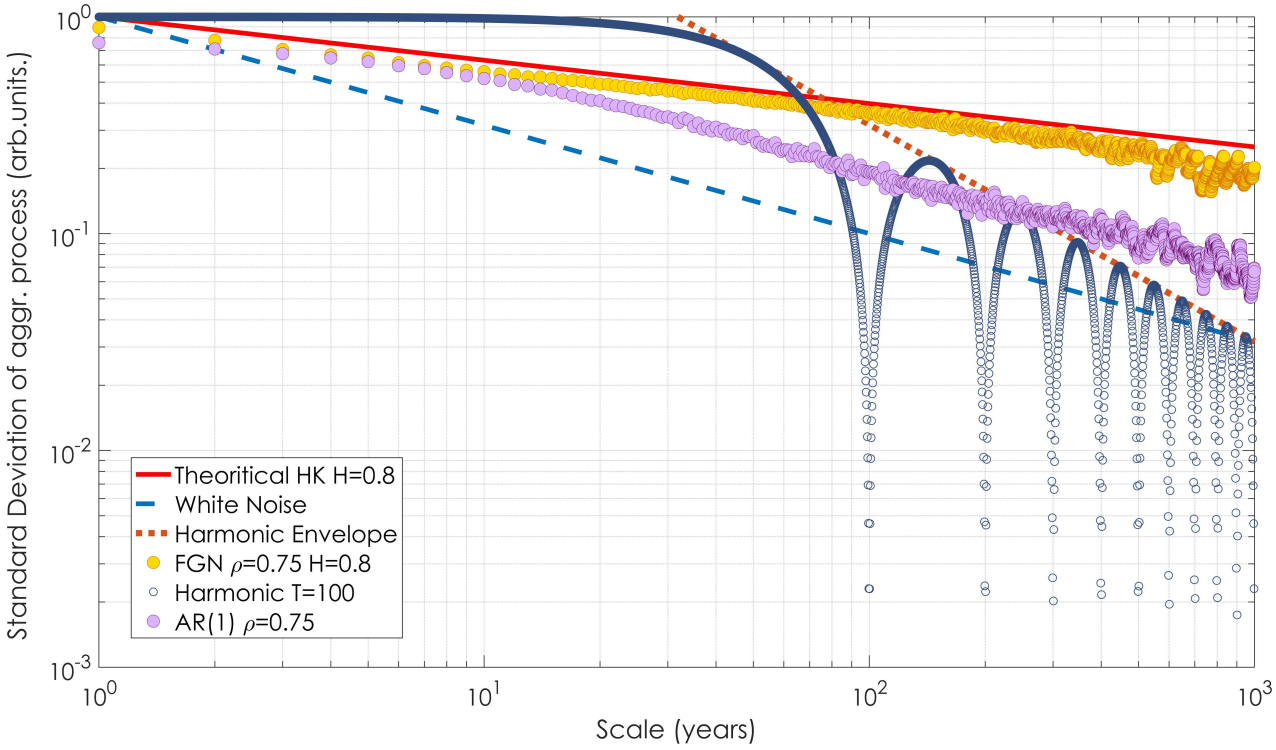

Εικόνα 1: Διάγραμμα συγκριτικής απεικόνισης των κλιμακογραμμάτων, τριών θεωρητικών διεργασιών (HK, Λευκός Θόρυβος, Αρμονική Συνάρτηση), και δύο συνθετικών χρονοσειρών (μοντέλα FGN, AR(1))

Στο διάγραμμα της Εικόνας 1 γίνεται μια συγκριτική αναπαράσταση των θεωρητικών κλιμακογραμμάτων (διπλή λογαριθμική απεικόνιση τυπικής απόκλισης χρονοσειράς συναθροισμένης σε κλίμακα *k,* ως προς την χρονική κλίμακα *k*) μιας διεργασίας Hurst-Kolmogorov με H=0.8 και μιας διεργασίας Λευκού Θορύβου (H=0.5), των εμπειρικών κλιμακογραμμάτων μιας συνθετικής χρονοσειράς μήκους n=10000 στοιχείων και χρονικού βήματος 1 χρόνου, παραχθείσα από μοντέλο AR(1) με συντελεστή αυτοσυσχέτισης 1ης τάξης $\rho_1 = 0.75$ και μιας ίδιου μήκους συνθετικής παραχθείσα από μοντέλο FGN με $\rho_1 = 0.75$ και H=0.8. Γίνεται επίσης αναπαράσταση του κλιμακογράμματος μιας αρμονικής περιοδικής συνάρτησης με περίοδο T = 100 χρόνια. Το θεωρητικό κλιμακόγραμμα μιας αρμονικής περιοδικής συνάρτησης δίνεται στην εξίσωση (α.8), όπου $\sigma^{(k)}$ η τυπική απόκλιση σε χρονική κλίμακα *k,* και *T* η χρονική περίοδος.

$$\sigma^{(k)} = \left|sinc\left(\frac{k}{T}\right)\right| = \left[\frac{T}{(\pi k)}\right]\left|\sin\left(\frac{\pi k}{T}\right)\right| \qquad (\alpha.8)$$

Στο ίδιο διάγραμμα, γίνεται εμφανές πως το μοντέλο AR(1) (μοβ κύκλοι), ενώ διατηρεί την κλίση (συντελεστή H) της ιστορικής χρονοσειράς μόνο για λίγες τιμές μικρών χρονικών κλιμάκων, η συμπεριφορά σε μεγαλύτερες κλίμακες προσεγγίζει αυτή του θεωρητικού κλιμακογράμματος του λευκού θορύβου (μπλε διακεκομμένη γραμμή). Αντιθέτως, το μοντέλο FGN (κίτρινοι κύκλοι) παρουσιάζει μια καλή αναπαραγωγή του συντελεστή H=0.8 του θεωρητικού μοντέλου HK (δηλαδή την κλίση της αρχικής ιστορικής χρονοσειράς με υποτιθέμενο H=0.8) αφού προσεγγίζει την κλίση της κόκκινης γραμμής του διαγράμματος. Το κλιμακόγραμμα της θεωρητικής αρμονικής συνάρτησης δείχνει το πως απεικονίζεται η απόλυτα περιοδική συμπεριφορά εντός του εργαλείου του κλιμακογράμματος, γεγονός που χρησιμοποιείται μετέπειτα για την ανάλυση χρονοσειρών με εσωτερική περιοδικότητα.

Μεταβλητότητα και εμμονή στη στάθμη της θάλασσας

Η εξέλιξη της παγκόσμιας στάθμης της θάλασσας αποτελεί σημαντικό κλιματικό παράγοντα, καθώς επηρεάζει την γενική κλιματική και ωκεάνια κυκλοφορία αλλά και το φυσικό και ανθρώπινο περιβάλλον, με χαρακτηριστική επίπτωση αυτή της μεταβολής της μορφολογίας των ακτών. Δορυφορικές μετρήσεις της στάθμης της θάλασσας από τα τέλη του 20ου αιώνα μέχρι και σήμερα φανερώνουν σταθερή αύξηση της μεταβλητής αυτής τόσο σε παγκόσμιο όσο και σε τοπικό επίπεδο. Όσον αφορά την παγκόσμια μεταβολή, σύμφωνα με τη Διακυβερνητική Επιτροπή για την Αλλαγή του Κλίματος (IPCC, 2013) η στάθμη της θάλασσάς ανέβηκε με μέση τιμή 1.7 [1.5 με 1.9] mm yr^{-1} την περίδο 1900-2010 και μέση τιμή 3.2 [2.8 και 3.6] mm yr^{-1} την περίοδο 1993-2010.

Η μεταβολή αυτή συσχετίζεται από την ίδια μελέτη με τη γενικότερη επιρροή της ανθρωπογενούς διεργασίας στην κλιματική ισορροπία του πλανήτη, με άμεση συσχέτιση με την παρατηρούμενη αύξηση της επιφανειακής θαλάσσιας θερμοκρασίας και της αποθηκευμένης θερμότητας εντός των ωκεάνιων μαζών, αλλά και με το φαινόμενων της τήξης των παγωμένων μαζών. Μελέτες όπως αυτές των Dangendorf et al. 2015 και των Marcos et al. 2017, διερεύνησαν την ύπαρξη μακροπρόθεσμης εμμονής στην μεταβλητή της στάθμης της θάλασσας, τόσο σε παγκόσμιο όσο και σε τοπικό επίπεδο. Η μέθοδος DFA2 που χρησιμοποιούν, διαχωρίζει τα σήματα εντός των διεργασιών σε αυτό που αιτιολογείται από την ύπαρξη φυσικής μακροπρόθεσμης εμμονής και στο υπολειπόμενο το οποίο καταλογίζεται σε βραχυπρόθεσμη μεταβλητότητα από φυσικά και ανθρωπογενή αίτια. Μέσω της μεθόδου

αυτής εμφανίζεται σημαντική μακροπρόθεσμη εμμονή στις παρατηρήσεις της στάθμης της θάλασσας σε τοπικό και παγκόσμιο επίπεδο. Παρ' όλα αυτά, οι μελετητές διακρίνουν ένα σημαντικό ποσοστιαίο «σήμα» το οποίο δεν μπορεί να αποδοθεί σε φυσική εμμονή και επομένως αποδίδεται κατ'αυτούς σε εξωγενείς παράγοντες, προβλέποντας μελλοντική συνέχεια της παρατηρούμενης αυξητικής τάσης της μεταβλητής.

Σε αυτήν την εργασία εξετάζουμε την ύπαρξη μακροπρόθεσμης εμμονής (ή αλλιώς τη μακροπρόθεσμη δομή αυτοσυσχέτισης) στη μεταβλητή της στάθμης της θάλασσας εντός πολλαπλών χρονικών κλιμάκων κυμαινόμενες από μήνες μέχρι και δεκάδες εκατομμύρια χρόνια. Χρησιμοποιούμε δορυφορικές μετρήσεις αλλά και πλήθος δειγμάτων από παλαιωκεανογραφικές ανακατασκευές της παγκόσμιας στάθμης της θάλασσας, τα οποία αναπαριστούν την εξέλιξη της μεταβλητής σε πολλές διαφορετικές χρονικές κλίμακες. Στον Πίνακα Α.1 παρουσιάζονται όλα τα δεδομένα της μεταβλητής της στάθμης της θάλασσας που χρησιμοποιούνται, μαζί με τον αριθμό τιμών, το χρονικό βήμα (αρχικό και κανονικοποιημένο με γραμμική παρεμβολή), το συνολικό μήκος, τον παράγοντα *α* που χρησιμοποιείται για την προσαρμογή του κλιμακογράμματος, καθώς και την βιβλογραφική τους αναφορά. Γραφήματα των χρονοσειρών παρατίθενται στην κύρια εργασία. Τα δείγματα ανακατασκευών τα οποία χρησιμοποιούνται διαθέτουν άριστη ετεροσυσχέτιση μεταξύ τους, και μάλιστα εντός πολλαπλών χρονικών κλιμάκων αφού αυτή σε καμία περίπτωση δεν πέφτει κάτω του 0.7.

Η μελέτη της μεταβολής της στάθμη της θάλασσας σε παλαιωκεανογραφικό επίπεδο όπως και ευρύτερα των παλαιοκλιματικών διεργασιών, μπορούν να συνδυάσουν την στοχαστική θεωρία με την τροχιακή θεωρία της Γης. Από την τελευταία, οι περιοδικοί κύκλοι Milankovitch, που οφείλονται στις κινήσεις του πλανήτη, εμφανίζονται στις παλαιοκλιματικές ανακατασκευές και επηρεάζουν σημαντικά την εξέλιξη της στάθμης της θάλασσας. Συγκεκριμένα η μετάπτωση των ισημεριών ή μεταβολή στην κατεύθυνση του γήινου άξονα της περιστροφής με περίοδο $T \approx 21{,}000$ χρόνια, οι αλλαγές στην λόξωση της εκλειπτικής ή στην αξονική κλίση με περίοδο $T \approx 41{,}000$ χρόνια και οι μεταβολές στην εκκεντρότητα με περίοδο $T \approx 100{,}000$ χρόνια, εμφανίζονται στην φασματική ανάλυση των χρονοσειρών που μελετώνται στην εργασία, με έντονο μάλιστα σήμα, και συνεπώς μοντελοποιούνται αναλόγως για την εξέταση της μεταβλητότητας και της εμμονής. Οι κινήσεις των κύκλων αυτών αναπαρίστανται στις τρεις φιγούρες της Εικόνας 2.

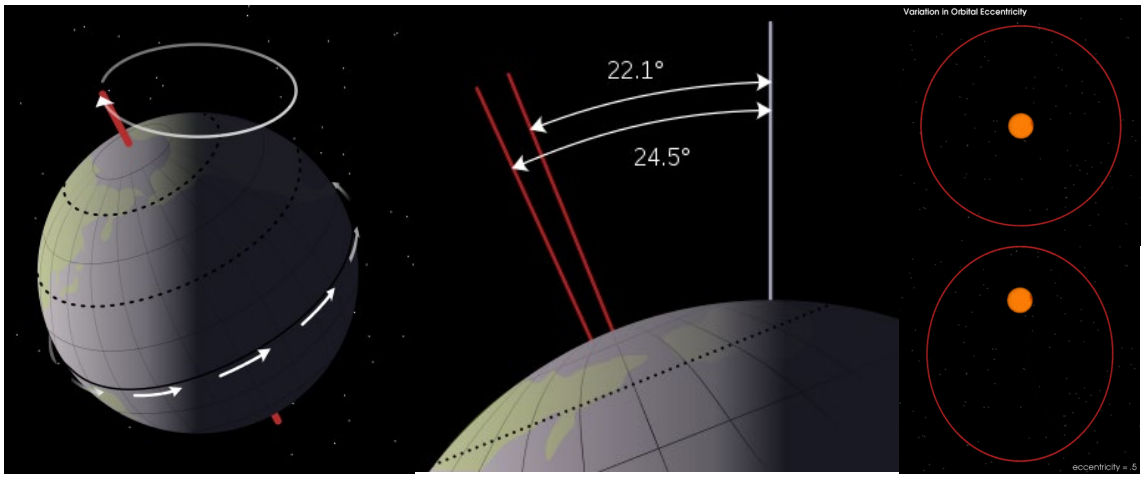

Εικόνα 2: Σχηματική αναπαράσταση των τριών Κύκλων Milankovitch

Συντομογραφία	Αριθμός τιμών *n*	Αρχικό εύρος βήματος (χρόνια)	Κανονικοποιημένο βήμα *Δ* (χρόνια) *	Συνολικό Μήκος *L* (χρόνια)	Παράγοντας Κλιμακογράμματος *α*	Βιβλιογραφική Αναφορά
Satellite Data	915	21/773	21/773	24.86	0.046	Benada (1997) Aviso (2003),CNES (2009)
Church and White	1608	1/12	1/12	134	0.0157	Church and White (2011)
Jevrejeva	2436	1/12	112	203	0.0118	Jevrejeva et al. (2014)
Kemp	211	0.1-73.1	10 (49%)	2,110	9.5	Kemp et al. (2011)
Grant	503	100-5,635	250 (28%)	125,750	0.0345	Grant et al. (2012)
Siddall	125	147-7,660	300 (6.57%)	375,000	0.033	Siddall et al. (2003)
Waelbroeck	287	1500	1500	430,500	0.0268	Waelbroeck et al. (2002)
Spratt	799	1000	1000	799,000	0.03	Spratt et al. (2016)
Deboer	53001	100	100	5,300,100	0.0382	De Boer et al. (2013)
Miller (short)	1801	1,000-5,000	5,000 (0%)	9,005,000	0.041	Miller et al. (2011)
Miller (long)	910	100,000	100,000	91,000,000	0.0315	Miller et al. (2005)
Kominz	984	100,000	100,000	98,400,000	0.023	Kominz et al. (2008)

Πίνακας Α.1: Στοιχεία χρονοσειρών στάθμης της θάλασσας

Για την θεώρηση της μεταβλητότητας και της μακροπρόθεσμης εμμονής μιας ενιαίας μεταβλητής της στάθμης της θάλασσας εντός πολλαπλών κλιμάκων, χρησιμοποιείται το εργαλείο του συνδυαστικού κλιμακογράμματος. Για την αναπαράσταση του συνδυαστικού κλιμακογράμματος, υπολογίζεται αρχικά το εμπειρικό κλιμακόγραμμα $\sigma_x^{(k)}$ τις κάθε μιας από τις χρονοσειρές $x_i(t)$, για διαφορετικές χρονικές κλίμακες k, ανάλογα με το μέγεθος και το βήμα της κάθε χρονοσειράς. Τα εμπειρικά κλιμακογράμματα σχεδιάζονται για κλίμακες $k < L/10$, όπου L το συνολικό μήκος της κάθε χρονοσειράς. Τα κλιμακόγραμμα, πολλαπλασιάζονται με ένα δείκτη βάρους a_x (ο δείκτης της κάθε χρονοσειράς παρατίθεται στον πίνακα Α.1) δημιουργώντας ένα συνδυαστικό κλιμακόγραμμα της μεταβλητής όπου:

$$\sigma_y^{(k)} = a_x \sigma_x^{(k)} \qquad (a.9)$$

Με αυτόν τον τρόπο (με την παραδοχή της γραμμικής σχέσης των εμπειρικών κλιμακογραμμάτων $\sigma_x^{(k)}$) το συνδιαστικό εμπερικό κλιμακόγραμμα εμφανίζει μια ενιαία μεταβλητή $\underline{y}(t)$ που απεικονίζει την εξέλιξη της παγκόσμιας στάθμης της θάλασσας σε πολλαπλές κλίμακες. Το εμπειρικό κλιμακόγραμμα εμφανίζεται με την γραμμή που ορίζει το

σύνολο των κλιμακογραμμάτων των διαφόρων μοντελοποιημένων χρονοσειρών (κύκλοι διαφορετικών χρωμάτων) στην Εικόνα 3.

Το συνδυαστικό θεωρητικό κλιμακόγραμμα, ρυθμίζεται έτσι ώστε να προσαρμόζεται στην καμπύλη του συνδυαστικού εμπειρικού κλιμακογράμματος. Το θεωρητικό κλιμακόγραμμα υπολογίζεται ως συνδυασμός ενός μοντέλου HK, και τεσσάρων αρμονικών συναρτήσεων. Το μοντέλο HK ρυθμίζεται με συντελεστή H = 0.995 για την προσέγγιση της κλίσης του εμπειρικού κλιμακογράμματος, με την παραδοχή της μεγιστοποίησης της εμμονής και της αβεβαιότητας. Τα μοντέλα των αρμονικών συναρτήσεων ρυθμίζονται με περιοδικότητες 21,000, 41,000 και 100,000 χρόνων που ανταποκρίνονται στους κύκλους Milankovitch, οι οποίοι εμφανίζονται και στην πτώση της κλίσης του εμπειρικού κλιμακογράμματος, για τις χρονικές κλίμακες 10^4-10^5 χρόνων. Μια επιπλέον αρμονική συνάρτηση με χρονική περίοδο 1,200,000 χρόνων προστίθεται στο θεωρητικό μοντέλο, για να το προσαρμόσει στην επόμενη πτώση του εμπειρικού κλιμακογράμματος (για k > 10^6) η οποία οφείλεται πιθανά σε ευστατικούς κύκλους του πλανήτη. Η εξίσωση (α.10) περιγράφει τον υπολογισμό του θεωρητικού κλιμακογράμματος ως το σύνολο των παραπάνω διεργασιών, ενώ ο πίνακας Α.2, παραθέτει τις τιμές των παραμέτρων και των συντελεστών του θεωρητικού μοντέλου. Το συνδυαστικό θεωρητικό κλιμακόγραμμα εμφανίζεται στην Εικόνα 4, με ενιαία κόκκινη γραμμή.

$$\sigma_{th}^{(k)} = \omega_1\sigma_{T_1}^{(k)} + \omega_2\sigma_{T_2}^{(k)} + \omega_3\,\sigma_{T_3}^{(k)} + \omega_4\,\sigma_{T_4}^{(k)} + \omega_5\sigma_{th}^{(k)} \qquad (\alpha.10)$$

Μοντέλο	Τιμή Παραμέτρου	Συντελεστής	Τιμή Συντελεστή
Αρμονική T_1	T_1 = 21,000	ω_1	0.02
Αρμονική T_2	T_2 = 41,000	ω_2	0.05
Αρμονική T_3	T_3 = 100,000	ω_3	0.10
Αρμονική T_4	T_4 = 1,200,000	ω_4	0.05
Hurst-Kolmogorov	**H = 0.995**	ω_5	0.78

Πίνακας Α.2: Παράμετροι μοντέλου του θεωρητικού κλιμακογράμματος

Οι τιμές της τυπικής απόκλισης του συνδυαστικού κλιμακογράμματος της Εικόνας 3, διαφέρουν μόνο κατά μία τάξη μεγέθους. Η τυπική απόκλιση στην κλίμακα των 10 εκατομμυρίων ετών είναι μόλις κατά 65% μικρότερη από αυτήν της κλίμακας του ενός μήνα, κάνοντας εμφανές τη μεγάλου μεγέθους μακροπρόθεσμη εμμονή που εμπεριέχεται στην μεταβλητή της παγκόσμιας στάθμης της θάλασσας. Συγκριτικά, μια τυχαία διεργασία λευκού θορύβου (H=0.5, μπλε διακεκομμένη γραμμή στην Εικόνα 3), εμφανίζει την ίδια πτώση τυπικής απόκλισης (65%) στην κλίμακα των 3 μηνών. Η πτώση του κλιμακογράμματος στις χρονικές κλίμακες 10^4 με 10^5 έτη αλλά και στις χρονικές κλίμακες 10^6 με 10^7 έτη, εμφανίζει πιθανή εσωτερική περιοδικότητα της μεταβλητής. Στην πρώτη περίπτωση, αυτή οφείλεται στους κύκλους Milankovitch, ενώ στη δεύτερη περίπτωση οφείλεται πιθανά σε μεγαλύτερης περιόδου ευστατικούς κύκλους (Miller, 2011). Για ελεγχθεί αν το θεωρητικό κλιμακόγραμμα (κόκκινη γραμμή, Εικόνα 3) είναι συμβατό με την πτώση του κλιμακογράμματος οφειλόμενη σε εσωτερική περιοδικότητα, κατασκευάζεται ένα στοχαστικό μοντέλο τύπου FGN, για την αναπαραγωγή συνθετικής χρονοσειράς βάση της εξίσωσης του θεωρητικού μοντέλου που κατασκευάστικε προηγουμένως (α.10). Με βάση την εξίσωση (α.10) αλλά και τις παραμέτρους του Πίνακα Α.2, παράγεται συνθετική χρονοσειρά μέσω μοντέλου FGN, στις οποίας το κλιμακόγραμμα αθροίζονται τα κλιμακογράμματα των τεσσάρων αρμονικών

συναρτήσεων. Το μήκος και το βήμα της συνθετικής χρονοσειράς λαμβάνονται ίσα με τη χρονοσειρά «Spratt» για την προσομοίωση του θεωρητικού μοντέλου στην περιοχή όπου το εμπειρικό κλιμακόγραμμα εμφανίζει απότομη πτώση κλίσης. Πράγματι, όπως φαίνεται στην Εικόνα 4, το κλιμακόγραμμα της παραχθείσας συνθετικής χρονοσειράς μέσω του θεωρητικού μοντέλου (κόκκινοι γεμισμένοι κύκλοι) συμβαδίζει με την πτωτική κλίση του εμπειρικού κλιμακογράμματος. Το κατασκευασθέν θεωρητικό μοντέλο συμβαδίζει με το εμπειρικό κλιμακόγραμμα της παγκόσμιας στάθμης της θάλασσας, για εύρος χρονικών κλιμάκων από 1 μήνα έως 10 εκατομμύρια χρόνια, εμφανίζοντας τη μεγάλη μακροπρόθεσμη εμμονή που εμπεριέχεται στη μεταβλητή καθώς και την εσωτερική περιοδικότητα που εμφανίζει εντός συγκεκριμένων χρονικών κλιμάκων.

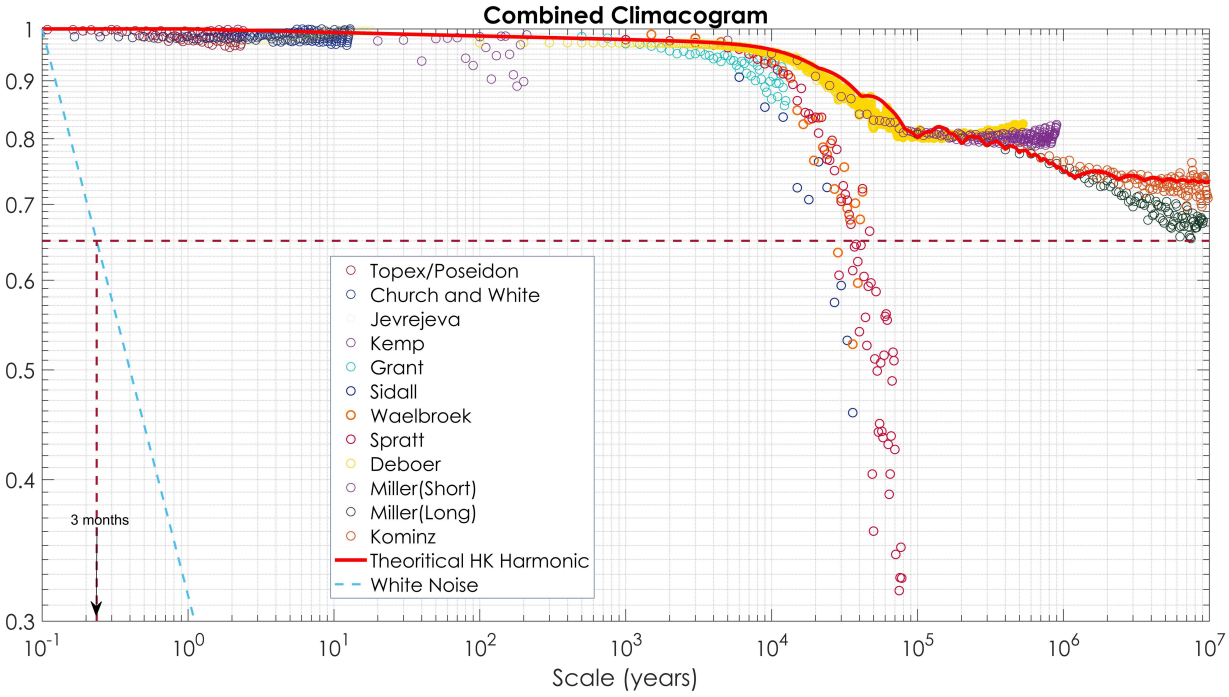

Εικόνα 3: Εμπειρικό και θεωρητικό συνδυαστικό κλιμακόγραμμα.

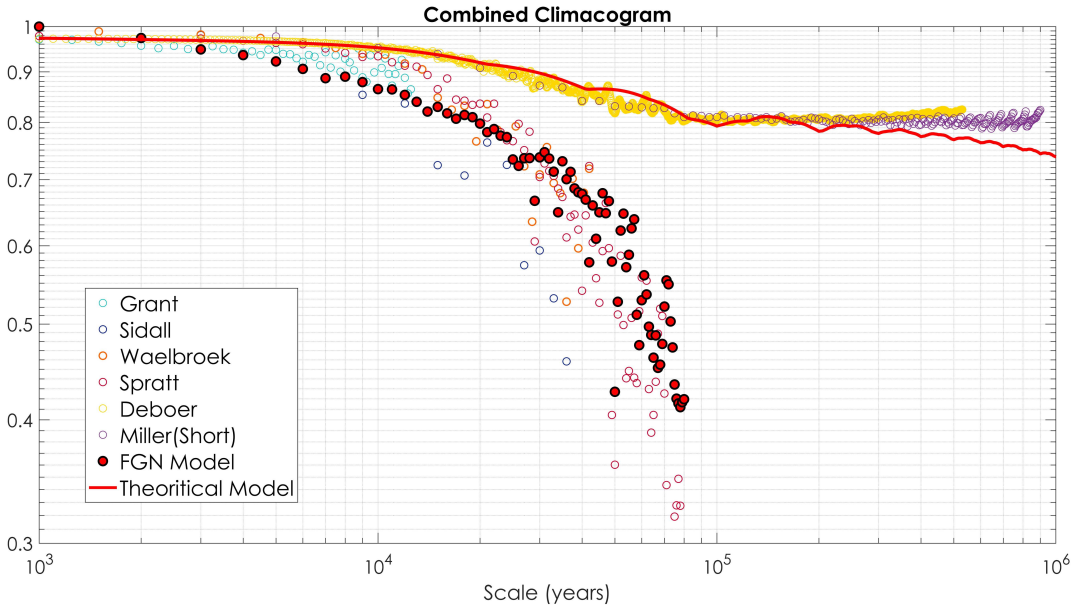

Εικόνα 4: Προσομοίωση συνθετικής χρονοσειράς στο κλιμακόγραμμα με μοντέλο FGN

Μεταβλητότητα και εμμονή στην επιφανειακή θαλάσσια θερμοκρασία και στο φαινόμενο El Niño

Το φαινόμενο El Niño – Νότια Ταλάντωση (ENSO) είναι μια περιοδική διακύμανση της επιφανειακής θαλάσσιας θερμοκρασίας και της πίεσης του αέρα της υπερκείμενής ατμόσφαιρας, στην περιοχή του Ισημερινού του Ειρηνικού Ωκεανού. Το ωκεανογραφικό φαινόμενο, εμφανίζεται σε μια θερμή (El Niño) και μια ψυχρή (La Niña) φάση, οι οποίες αναταράσσουν την ωκεάνια και ατμοσφαιρική κυκλοφορία τόσο του Ειρηνικού Ωκεανού αλλά και όλου του πλανήτη, προκαλώντας σημαντικές μεταβολές της θερμοκρασίας και της στάθμης της θάλασσας καθώς και κλιματικά φαινόμενα, όπως έντονες βροχοπτώσεις και ξηρασίες σε διαφορετικά μέρη του πλανήτη. Το φαινόμενο μετράτε μέσω δεικτών όπως ο δείκτης SOI, ο οποίος μετράει την διαφορά της ατμοσφαιρικής πίεσης μεταξύ των σταθμών Tahiti και Darwin, ή ο δείκτης ONI, ο οποίος μετράει της διακυμάνσης της επιφανειακής θαλάσσιας θερμοκρασίας στην περιοχή Niño. Οι γεωγραφικές περιοχές μελέτης του φαινομένου ENSO αναπαρίστανται στην Εικόνα 5, με κυριότερη την περιοχή Niño 3.4.

Για την μελέτη της μεταβλητότητας και της ύπαρξης εμμονής στη μεταβλητή της επιφανειακής θαλάσσιας θερμοκρασίας, μελετάμε αρχικά μετρήσεις και ανακατασκευές των δεικτών του φαινομένου ENSO, με τη χρήση του εργαλείου του κλιμακογράμματος. Στη συνέχεια, υπολογίζουμε την δομή αυτοσυσχέτισης της καταγεγραμμένης παγκόσμιας επιφανειακής θαλάσσιας θερμοκρασίας (SST), εξετάζοντας επίσης τη συσχέτιση της διακύμανσης της με τη συμπεριφορά του φαινομένου ENSO.

Τα χαρακτηριστικά στοιχεία των μελετηθέντων δεικτών εμφανίζονται στον Πίνακα Α.3. Οι τρεις πρώτες σειρές του πίνακα αφορούν δείκτες που πηγάζουν από μετρήσεις, θερμοκρασιών και πιέσεων, ενώ οι τρεις τελευταίες δείκτες που παρήχθησαν από παλαιοκλιματικές ανακατασκευές. Στον πίνακα εμφανίζονται οι συντελεστές Hurst, οι οποίοι υπολογίζονται μέσω τις κλίσης των κλιμακογραμμάτων (τα διαγράμματα των κλιμακογραμμάτων είναι διαθέσιμα στην κύρια εργασία). Το φαινόμενο ENSO παρουσιάζει για μικρές κλίμακες χρόνου, μικρότερες των 100 ετών, έντονη αντι-εμμονική συμπεριφορά, όπως φαίνεται από του συντελεστές Hurst (<0.5) των πρώτων πέντε σειρών του Πίνακα Α.3. Για μεγαλύτερες χρονικές κλίμακες, με βάση την ανακατασκευή του Moy et al. (2012), το φαινόμενο φαίνεται να παρουσιάζει, έντονη εμμονική συμπεριφορά για μεσαίου μήκους κλίμακες (100-500 χρόνια), ενώ επιστρέφει σε αντι-εμμονική συμπεριφορά σε χρονικές κλίμακες μεταξύ 500 και 1000 ετών.

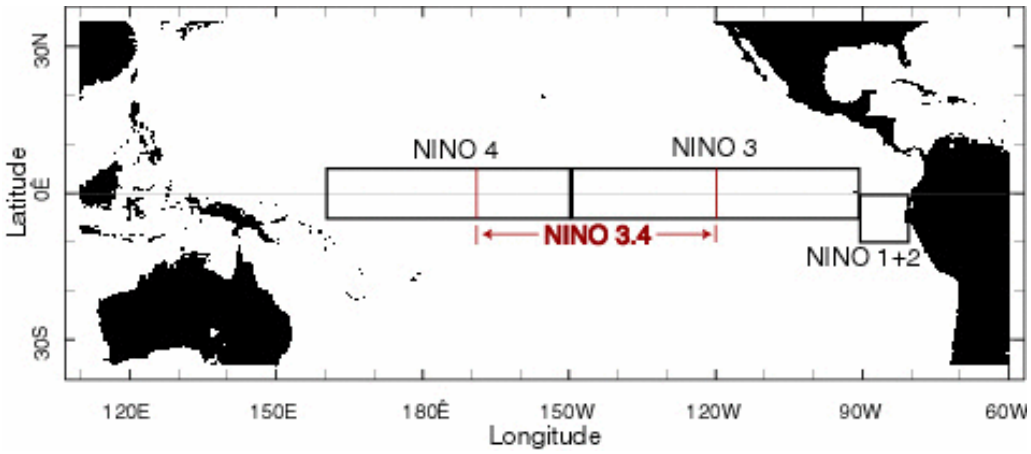

Εικόνα 5: Περιοχές μελέτης του φαινομένου ENSO (πηγή: NOAA)

Χρονοσειρά και πηγή	Μήκος (*L*) (χρόνια)	Αρχικό (O) ή Κανονικοποιημένο (R) Βήμα (*Δ*) (χρόνια)	Συντελεστής Hurst (*H*)
NOAA (ONI)	68	1/12 (O)	**0.166**
BMC Australia	141	1/12 (O)	**0.398**
Uni. East Anglia	151	1/12 (O)	**0.462**
Li et al. (2013)	1100	1 (O)	**0.384**
McGregor et al. (2010)	327	1 (O)	**0.225**
Moy et al. (2002)	11,000	1 (R)	**0.84** (*k*=10-300) **0.08** (*k*=500-1100)

Πίνακας Α.3: Στοιχεία χρονοσειρών δεικτών ENSO και συντελεστές Hurst

Για την μελέτη της μεταβλητότητας της επιφανειακής θαλάσσιας θερμοκρασίας (SST) χρησιμοποιείται ο παγκόσμιος κάνναβος ERSSTv5 (Huang et al. 2017), που αποτελεί ανακατασκευή της θερμοκρασίας, βάση δορυφορικών μετρήσεων για το χρονικό διάστημα 1854-2018 με μηνιαίο χρονικά βήμα. Η χρονοσειρά σε μορφή καννάβου, μετατρέπεται επίσης σε ετήσια χρονοσειρά (μέσω κυλιόμενου μέσου) καθώς και διακριτοποιείται σε 12 χρονοσειρές για καθένα από τους 12 μήνες του έτους, έτσι ώστε να αφαιρεθεί η εσωτερική κυκλοστασιμότητα της μεταβλητής. Με βάση τα δεδομένα του καννάβου και την εξίσωση (α.2) υπολογίζονται οι τιμές του συντελεστή αυτοσυσχέτισης για κάθε σημείο του καννάβου. Αντίστοιχα, με έναν σύντομο αλγόριθμο υπολογίζονται οι τιμές του συντελεστή Hurst, ως η κλίση του κλιμακογράμματος, επίσης για κάθε σημείο.

Παρουσιάζονται εδώ μερικά από τα αποτελέσματα καθώς και τα βασικά συμπεράσματα τους. Στην Εικόνα 6, εμφανίζεται ο παγκόσμιος συντελεστής Hurst για την ετήσια χρονοσειρά ERSSTv5. Στις περιοχές Nino 3.4, 3, 2 και 1 εμφανίζεται έντονη αντι-εμμονική συμπεριφορά, γεγονός που συνάδει με τα ευρήματα της αντι-εμμονικής συμπεριφοράς στις μετρήσεις και τις ανακατασκευές των δεικτών του φαινομένου ENSO. Παράλληλα, στις υπόλοιπες περιοχές του πλανήτη η επιφανειακή θαλάσσια θερμοκρασία εμφανίζει τιμές H > 0.75, οι οποίες δείχνουν έντονη εμμονική συμπεριφορά της μεταβλητής. Παρόμοια συμπεριφορά εμφανίζεται στην Εικόνα 7, όπου αναπαρίσταται ο συντελεστής αυτοσυσχέτισης $1^{ης}$ τάξης (lag 1) για τις 12 διακριτοποιημένες χρονοσειρές που αντιστοιχούν στους δώδεκα μήνες του έτους. Οι μικρές τιμές του συντελεστή αυτοσυσχέτισης -κατ' αντιστοιχία των μικρών τιμών του συντελεστή Hurst, εμφανίζονται στις ίδιες γεωγραφικές περιοχές με την Εικόνα 6. Παράλληλα, η διακύμανση των τιμών του συντελεστή αυτοσυσχέτισης στην περιοχή Niño, μαρτυρά την αντίστοιχη διακύμανση της εμφάνισης του φαινομένου αυτού ανάμεσα στους μήνες του έτους.

Συμπερασματικά, τα ευρήματα αυτού του κομματιού της εργασίας δείχνουν αντι-εμμονική συμπεριφορά της επιφανειακής θαλάσσιας θερμοκρασίας στην περιοχή Niño και ταυτόχρονα εμμονική γενική συμπεριφορά της μεταβλητής σε παγκόσμια κλίμακα. Παρ' ότι η συμπεριφορά στην περιοχή Niño μπορεί να συνεπάγεται μειωμένη αβεβαιότητα του φαινομένου ENSO, τα ευρήματα της εξέτασης των δεικτών του δείχνουν ότι σε μεγαλύτερες χρονικές κλίμακες αυτό παύει να ισχύει καθώς το φαινόμενο επιστρέφει σε εμμονική συμπεριφορά. Η διαθεσιμότητα δειγμάτων μεγαλύτερης χρονικής κλίμακας, τόσο των δεικτών του φαινομένου ENSO, όσο και της παγκόσμιας επιφανειακής θαλάσσιας θερμοκρασίας μπορούν να διαλευκάνουν περαιτέρω την φυσική εμμονή που εμφανίζουν οι μεταβλητές αυτές.

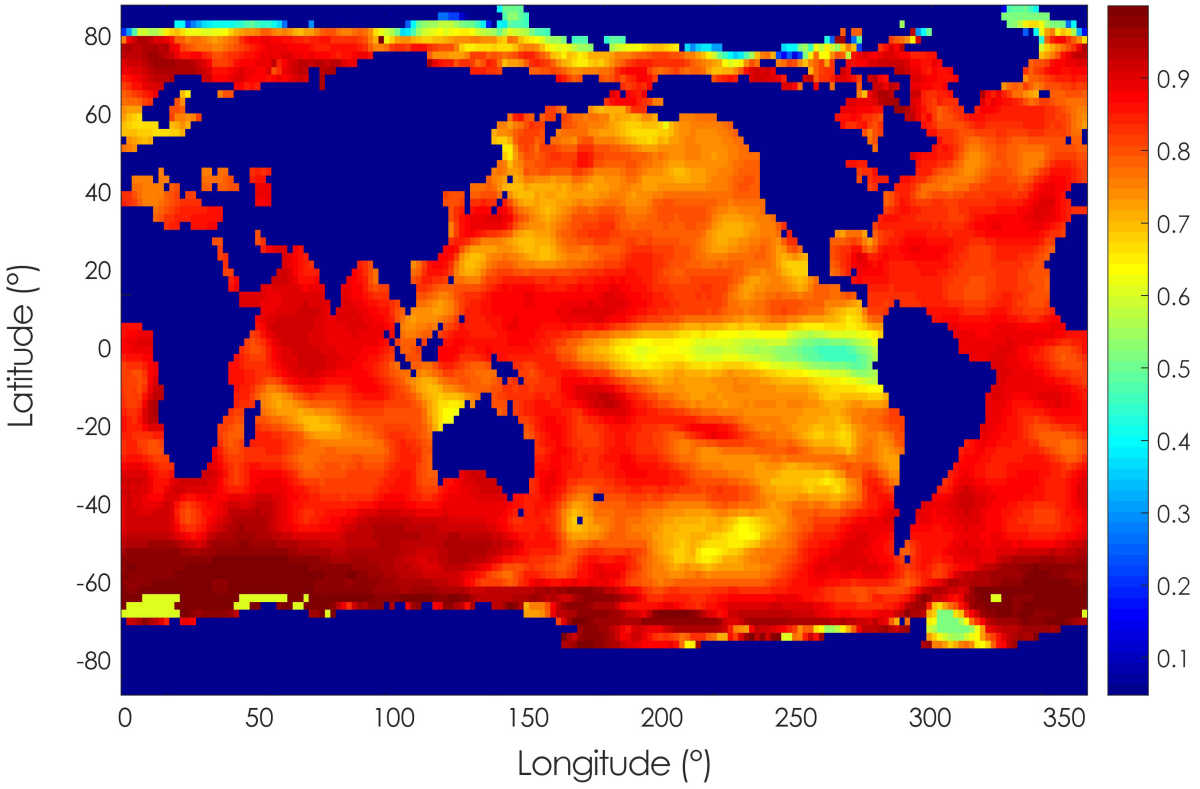

Εικόνα 6: Παγκόσμια κατανομή του συντελεστή Hurst για την ετήσια χρονοσειρά επιφανειακής θαλάσσιας θερμοκρασίας (SST)

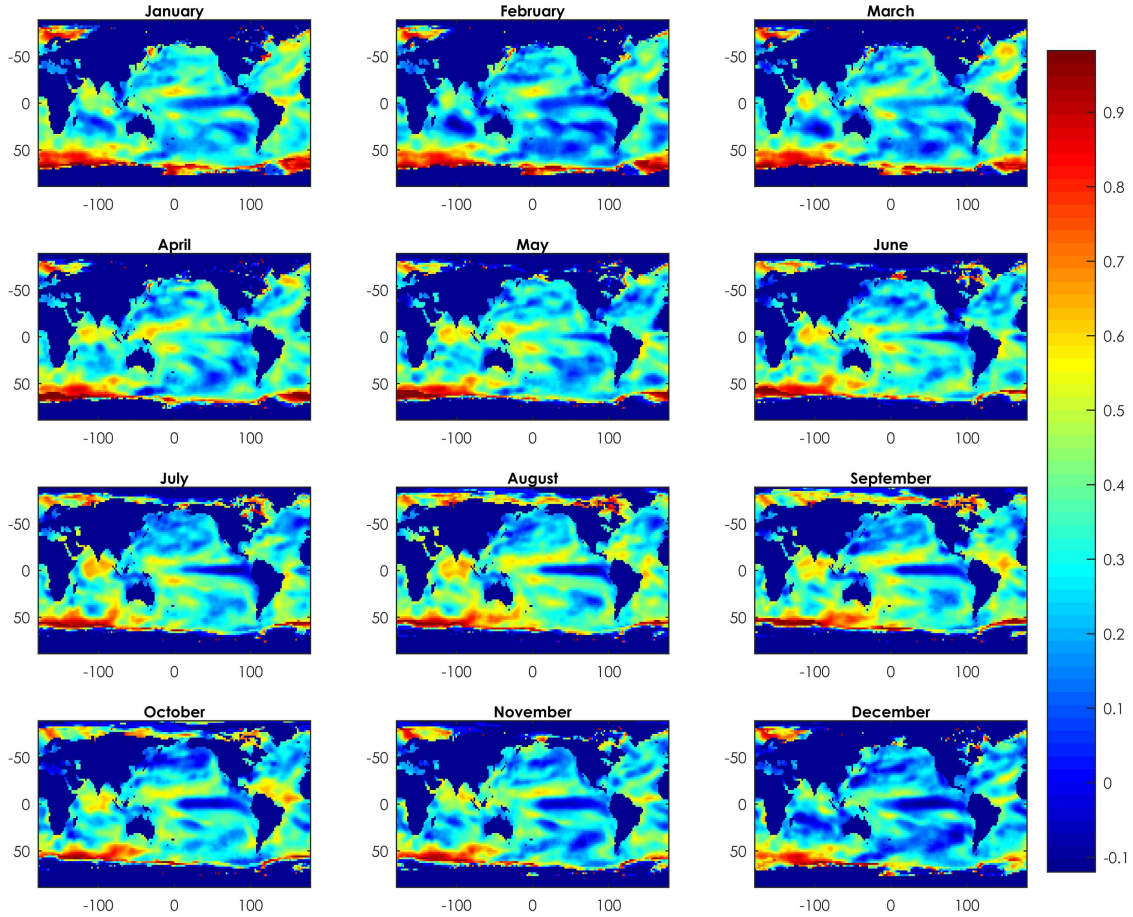

Εικόνα 7: Συντελεστής αυτοσυσχέτισης (lag 1) για την ετήσια χρονοσειρά επιφανειακής θαλάσσιας θερμοκρασίας (SST) κατανεμημένης σε 12 μήνες του έτους

Table of Contents

Chapter 1: Natural Processes and change

Change is, philosophically, an intrinsic law of the universe. This concept is commonly shared among most of the philosophical thinkers in Ancient Greece. It is especially depicted in the infamous "*τὰ πάντα ῥεῖ" (panta rhei), everything flows,* quote attributed Heraclitus of Ephesus, a pre-Socratic Greek Philosopher, as noted in Plato's Cratylus, 339–340, used to describe the omnipresence of change. Heraclitus notes even more the concept unity of opposites expressed through dialectic dipoles like "summer-winter", "war-peace", "the way up-the way down". This unity, antithesis and struggle between the opposites (αντίθετα, antitheta), is for him the driving law -the potential- of change. (Kirk, 1951)

Time as an essence of change is discussed in Plato, where it is defined as the moving image of eternity or of the idea that time is in some other way the appearance of some unchanging thing. For Plato, the change of reality, that is implicated through time, is caused by what he calls *the flux,* which is the same as a moving but ever-present time. Aristotle, variates Plato's view defining time as motion, and thus including the element of the omnipresence of change. (Lieb 1991)

Aristotle notably quotes that through a natural example in Meteorologica 353a14-24, concerning the sea level, a variable of interest in this study. For the essence of natural change depicted here, but also for the coincidence of variables we refer the quote:

> φανερὸν τοίνυν, ἐπεὶ ὅ τε χρόνος οὐχ ὑπολείψει καὶ τὸ ὅλον ἀίδιον, ὅτι οὔτε ὁ Τάναϊς οὔτε ὁ Νεῖλος ἀεὶ ἔρρει, ἀλλ' ἦν ποτε ξηρὸς ὁ τόπος ὅθεν ῥέουσιν· τὸ γὰρ ἔργον ἔχει αὐτῶν πέρας, ὁ δὲ χρόνος οὐκ ἔχει. ὁμοίως δὲ τοῦτο καὶ ἐπὶ τῶν ἄλλων ἁρμόσει ποταμῶν λέγειν. ἀλλὰ μὴν εἴπερ καὶ οἱ ποταμοὶ γίγνονται καὶ φθείρονται καὶ μὴ ἀεὶ οἱ αὐτοὶ τόποι τῆς γῆς ἔνυδροι, καὶ τὴν θάλατταν ἀνάγκη μεταβάλλειν ὁμοίως. τῆς δὲ θαλάττης τὰ μὲν ἀπολειπούσης τὰ δ' ἐπιούσης ἀεὶ φανερὸν ὅτι τῆς πάσης γῆς οὐκ ἀεὶ τὰ αὐτὰ τὰ μέν ἐστιν θάλαττα τὰ δ' ἤπειρος, ἀλλὰ μεταβάλλει τῷ χρόνῳ πάντα.
>
> "So it is clear, since there will be no end to time and the world is eternal, that neither the Tanais nor the Nile has always been flowing, but that the region whence they flow was once dry: for their effect may be fulfilled, but time cannot. And this will be equally true of all other rivers. But if rivers come into existence and perish and the same parts of the earth were not always moist, the sea must needs change correspondingly. And if the sea is always advancing in one place and receding in another it is clear that the same parts of the whole earth are not always either sea or land, but that all this changes in course of time.. "

Science, from ancient times to the modern days, has come to reaffirm the philosophical thesis of change. The philosophical perception of the omnipresence of change did not arrive arbitrarily; it has been founded on the human observation of nature. As can be noted in the previous quote, the observation of the flow of the Nile river but also the change in the sea level, acted as natural stimuli to evoke the philosophical position. Natural sciences, which take this observation into the level of experimentation and scientific knowledge have long accepted this

thesis as an axiom. It is inherent in the laws and study of Physics, whether they are Newtonian Quantic, or Geophysics.

In this first chapter we restrict ourselves to a basic philosophical discussion and definition of concepts and aspects surrounding change, so as to describe the line of thought of the author behind the chapters that follow, which present an applied scientific methodology on natural variables.

1.1 Some aspects of change

The concept of change becomes application-wise useful in natural sciences, when certain aspects of it are acknowledged and defined. They will be discussed in this chapter in a generic sense, the perception of which leads to the specific applications in geophysical processes discussed in the following chapters.

1.1.1 The spiral motion

The shape of a spiralling seashell depicts in a natural and simple, yet full of complexity, way the trajectory of change. Heraclitus used another aquatic metaphor, to depict the same trajectory: *"ποταμοῖσι τοῖσιν αὐτοῖσιν ἐμβαίνουσιν, ἕτερα καὶ ἕτερα ὕδατα ἐπιρρεῖ"*[2], meaning *"Ever-newer waters flow on those who step into the same rivers".* Through these two images one can derive not only the impossible of a repetition of a past state, but also the way that change progresses forward.

If a sea-worm of change were to walk on the inside of the spiralling seashell and observed from the outside on a 2-D plane, top view, there would be a point where the observer would guess that the worm has completed a full circle of motion and arrived to its starting point. In reality, if another observer watched the seashell from a side-view, as a spiralling staircase, he/she would realise that the worm has reached what seemed to be the same point, but on *a higher level of the spiral.*

Another limited perception, of the sea-worm's trajectory, would exist through an observer watching the worm for a limited period of time. Then he might guess that the worm is walking on a straight line, which is only a proportion of the total trajectory, as shown also in Leibniz's calculus.

1.1.2 The dependence of the future on the past

The future and the past can only be defined relatively to the present. When measuring a certain natural variable, the present could be defined as the actual moment of the measurement of the value of the variable, defining the past as all the moments of known (by natural reality, and observed by the human observer) values that came before it and future the moments of the unknown (both by natural reality and the human observer) evolution of the measured variable.

As it can be seen through the previous concept, the future does not have the same essence as the past and the present do, on a variable value. If the future variable is considered to behave randomly, the past and the present are not as they are already measured. Applying this logic

[2] DK22B12, quoted in Arius Didymus apud Eusebius, Praeparatio Evangelica, 15.20.2

into the previous example, if we could assume a random movement for the future positions of the worm in the spiral, all its previous positions would be known.

Complete randomness, in the sense of an independent future evolution of the variable can be found only on isolated experiments, as is a drop of a dice. In a complex natural environment, every future evolution would be dependent on the past values of the measured or other variables. No one could imagine a real sea worm making its next step in the bottom of the spiral when it has reached its top, except if it were to fall by a toppling of the sea shell itself. Even in the latest case, the move of the worm would depend on a certain present act on the examined natural system.

In the above sense the concept of memory (or long-term) memory in process been discussed, in natural phenomena and mathematics (Klemeš, 1974; Beran, 1994). Indeed, treating memory as "dependence" on the past natural processes have been shown to have an inertial capability of depending on their past evolution. However, Koutsoyiannis (2002) has discussed the possibility of a concept of "absence of memory" in natural process in contrast to the "long-term memory" concept, meaning that a system "forgets" not only its past values but also its past means. The omnipresent dependency (depicted through autocorrelation in stochastic analysis) in natural process, and specifically the long-term one, arrives, for Koutsoyiannis, through random fluctuations occurring on different scales and creating variability of different frequency signals in the process. The concepts of "randomness" and "scales" will be discussed here onwards.

1.1.3 The aspect of time scales

Processes are simultaneously occurring on multiple scales, of both time and space. To keep the previous paradigm, if the sea-worm were to operate in a seashell trajectory, this movement would have happened on the course of a broader movement, in temporal and spatial terms, the one of the earth in a trajectory around the sun. Even if we can isolate a process, from all the others in broader and narrower level, in order to observe it, it is still being affected by the ongoing change on different scales.

Natural processes occur on multiple time scales but are only measured on specific ones. That means that the measured variable on a certain time scale, incorporates inside it «*signals»* of different frequencies, which are causing its fluctuations and are caused by the past evolution of the variable on different time scales. Large time scales would produce low-frequency signals, while small time scales would produce high-frequency ones.

1.2 The concept of randomness. Predictability and uncertainty.

The notions of random events and random variables have been defined by the Russian mathematician A.N Kolmogorov in his fundamental work (Kolmogorov, 1963) – for the latter notion see Chapter 2. In spite of his rigid mathematic definitions on these concepts that served as a base for the modern theory of probability, he did not define the concept of randomness early on. Later, in about 1965, A. N. Kolmogorov and G. J. Chaitin independently proposed a

definition of randomness based on complexity or absence of regularities or patterns -which could be reproduced by an algorithm- (Chaitin, 1975; Kolmogorov, 1965).

These definitions seek the concept of randomness into mathematical word, outside of the physical phenomena. When the notion of randomness is introduced into the physical world, the cosmos, it is always paired with its sister pole, the one of determinism, forming the dialectic dipole of "necessity-chance", both on epistemological and ontological level (Mpitsakis, 2003). The epistemological approach of classical Newtonian physics considers randomness only as the not-yet understandable part of a process, or in other terms, the real "demon" limiting humans of achieving the intellect, as portrayed in the infamous Laplace's demon (Laplace, 2012).

The survival of this conception applied in modern physical sciences as geophysics, leads to the separation of a "deterministic" and "random" process or "parts", in natural processes, which in their term produce cause-effect relations on the first case and "noise" on the second, the last of which should be dispelled, according to this conception, by scientists to reveal the true movement of nature. Two physical examples that picture in an absolute sense the deterministic or Newtonian conception of nature, is the total antithesis between the absolute predictable of the movement of the planets and the absolute random of the roll of a dice. Through the survival of this conception, even after the foundation of modern probabilities, the field of science in probabilities/statistics/stochastic methods and their applcation in natural processes has existed mainly as a supporting tool to deterministic scientific methods, giving them the ability to be able to quantify probabilistically, what cannot be predict deterministically (due to lack of data or tools).

Here we present a conception divernget and constrasting to the previous. We refer two works scientists, among many, who formulate it, in the field of natural systems. It is portrayed in the work of physical chemist I. Prigogine and notably in Prigogine and Stegners (1985), where the authors research the implementation of the aforementioned dipole of necessity-chance in the physical world, the creation of order out of chaotic systems. They show that systems tend to arrive at certain points of instability, where random, irreversible changes of state occur leading to a new creation of order in the system, through an auto-organization process. This conception cancels out the dichotomy between the concepts of randomness of determinism. Rather, it shows the unity in its opposite in the sense of Heraclitus discussed above here, and thus the appearance of these two concepts as the two sides of the same coin.

In a same motive, hydrologist D. Koutsoyiannis has supported that the element of randomness, can be actually identified through the notion of "unpredictability" or "uncertainty". In this sense, randomness exists in processes that we may understand, we may explain, but we cannot predict. This notion also leads to a disruption of the dichotomy, not seeing determinism and randomness as two different (separate or additive) parts of the same process, but rather as a unity of opposites, where the dominance of the one or the other pole depends on the time horizon and the scale of prediction (Koutsoyiannis, 2010). In the same study Koutsoyiannis proves the possibility of creation of random dynamics (e.g. uncertainty) from a completely deterministic system, arriving to common conclusions with Prigogine. It is also important that both authors note the concept of entropy (and its derivative concepts: irreversibility and arrow of time) as the driving force of change in physical system but also as a measure of the behavior of the system in terms of the uncertainty in its behaviour. These concepts will not be analyzed

furtherly here and the reader is referenced to Prigogine and Stegners (1997), Ben-Naim (2008), Theodoratos (2012) and Koutsoyiannis (2017).

Following the latter motive, this study aims to seek uncertainty in the variability of physical processes, by utilizing probability theory, statistics and stochastic methods and tools as means to examine change (in terms of variability and persistence, see next section) in their past evolution and quantify uncertainty in their future prediction.

1.3 Long Term Persistence in natural processes

The internal "dependency on the past" of natural processes is mathematically depicted through the autocorrelation structure of the stochastic process that represents it (see Chapter 2). The famous work of Hurst (1951), which examined the long-term variability of the Nile river flow records in order to calculate the long-term storage capacity of reservoirs. Through this examination he came across a stumbling discovery, later termed the "Hurst Phenomenon" or "Long Term Persistence" (LTP), or "Long Range Dependence", of a long-term (else large-scale) high autocorrelation of the Nile river time-series, appearing through the grouping of maximum and minimum values on high scale aggregations of the time-series (for more see Chapter 2). This phenomenon has been studied and revalidated on modern Nile river records (Awadallah, 2014) but also observed by Hurst himself in climatic and other geophysical records (Sutcliffe, 2016).

The Long-Term Persistence or Hurst Phenomenon portrays the multi-scale fluctuation of natural processes, adapting to the criteria discussed early on in this chapter. The same behaviour is observed in the long-term evolution of various geophysical parameters, such as atmospheric temperature, wind speed, river flows, precipitation and evaporation small-scale and large-scale turbulence, tree ring data and a lot more (Dimitriadis, 2017; Koutsoyiannis, 2018). On oceanic variables, long-term persistence has been examined and observed in data of sea surface and oceanic temperatures (Fraedrich and Blender, 2003; Monetti et al., 2003; Alvarez-Ramirez et al., 2008), Pacific Decadal Oscillation, North Atlantic Oscillation, and El Niño-Southern Oscillation indices (Stephenson, 2002; Wang and Tsonis, 2008; Khaliq, 2010), wave height (Moschos et al. 2017a and 2017b), sea level (Dangendorf et al., 2014; Dangendorf et al. 2015, Marcos et al. 2014), as well as other parameters.

The long-term persistent behaviour is examined in this study in the evolution of geophysical time-series depicting oceanic variables of the sea-level rise, sea surface temperatures, and of the El Niño -Southern Oscillation indices through an analysis of their observed variability on multiple scales.

Chapter 2: Stochastic methods and tools

2.1 Why stochastics?

Modern geophysical data assessment, both regarding the comprehension of the past evolution and the projection of the future state, uses modelling that incorporates deterministic methods, called hereby deterministic models. In the case of climate modelling especially, the complex software tools called General Circulation Models (GCMs), fall generally into the aforementioned category (Loehle, 2018). Antithetically, stochastic modelling, although incorporated as enhancement to the mainstream modelling cases is, yet, an unfavourable choice of use.

While stochastic modelling is reading the past on a similar manner with its deterministic counterpart, when referring to the future the stochastic method does not produce a projection but rather a probabilistic assessment of it, which depends on past observations. This way possibilities rather than certainties are expressed by the modelling process; or to name it better: the uncertainty factor is considered and estimated.

Another important distinction of stochastic methodology in modelling is its parsimony. Even though, the principle of parsimony in science broadly and in modelling natural phenomena specifically, has long been a foundation and a basis for application, the recent evolution in computational strength of modern machines has led to a neglection of parsimony and a substitution by complex, multi-parameter systems that seek to replicate and reproduce every detail of the natural complexity (Koutsoyiannis, 2016).

Seeking a probabilistic study of various natural variables regarding oceanic phenomena through parsimonious applications, this study utilizes tools, which, albeit light and delicate in their structure tools -demanding basic concepts of probability theory-, they may arrive into heavy-weighted results. The parsimony element of the tools utilized in this study, allows also for an easy reproduction of the result by the reader with simple computational tools. The definitions and concepts of stochastic processes and methods, as well as the description of the modelling tools used in this study are given in this section.

2.2 Definitions of key stochastic elements

2.2.1 Random Variables, Stochastic Processes and their basic properties

A random variable $\underline{x}$ is a function that maps outcomes to numbers, i.e. quantifies the sample space Ω. A particular value that a random variable may take in a random experiment, else known as a realization of the variable, is a number. We adopt here the Dutch convention, which is used to denote the random variables by an underlined letter e.g. $\underline{x}$, whereas a non-underlined letter e.g. x denotes its realization (Hemelrijk, 1966).

A stochastic process $\underline{x}(t)$, is defined as a family of random variables $\underline{X}(t)$, where $t \in T$, and T is a set of real numbers (usually represents time). If T is the real axis, then x(t) is a *continuous-*

time process. If T is the set of integers then x(t) is a *discrete-time* process (Papoulis 1991). A realization of a stochastic process namely a set of observations $\underline{x}(t)$ of X(t), arranged in a strict time sequence is named a time-series. Time-series produced through stochastic methods are called synthetic time-series. In contrast, observed time-series are labelled here as historical, observed or modelled.

For a specific t, $\underline{x}(t)$ is a random variable with distribution:

$$F(x,t) = P\big(\underline{x}(t) < x\big) \tag{2.1}$$

Where the function $F(x,t)$ is called the first-order distribution of the process $\underline{x}(t)$, while its derivative with respect to x, is called the probability density function $f(x)$, or the first order density of $\underline{x}(t)$, i.e.:

$$f(x) := \frac{dF(x)}{dx} \tag{2.2}$$

For many applications, knowing the distribution function is not needed, as only certain properties of the process are needed. These properties are named secondary-order properties of the stochastic process $\underline{x}(t)$. Following we quote the definition of three of these properties the *Mean*, the *Autocorrelation* and the *Autocovariance*, as stated in (Papoulis, 1991):

- *Mean*: The mean $\eta(t)$ of $\underline{x}(t)$ is the expected value of the random variable $\underline{x}(t)$:

$$\eta(t) = E\big\{\underline{x}(t)\big\} = \int_{-\infty}^{\infty} x f(x,t)dx \tag{2.3}$$

- *Autocorrelation*: The autocorrelation $R(t_1,t_2)$ of $\underline{x}(t)$ is the expected value of the product $\underline{x}(t_1)\underline{x}(t_2)$:

$$R(t_1,t_2) = E\big\{\underline{x}(t_1)\underline{x}(t_2)\big\} = \int_{-\infty}^{\infty}\int_{-\infty}^{\infty} x_1 x_2 f(x_1,x_2;t_1,t_2)dx_1 dx_2 \tag{2.4}$$

  The value of $R(t_1,t_2)$ on the diagonal $t_1=t_2=t$ is the *average power* of $\underline{x}(t)$:

$$E\big\{\underline{x}^2(t)\big\} = R(t,t) \tag{2.5}$$

- *Autocovariance:* The autocovariance $C(t_1,t_2)$ of $\underline{x}(t)$ is the covariance of the random variables $\underline{x}(t_1)$ and $\underline{x}(t_2)$:

$$C(t_1, t_2) = R(t_1, t_2) - \eta(t_1)\eta(t_2) \tag{2.6}$$

And its value C(t,t) on the diagonal $t_1=t_2=t$ equals the *variance* of $\underline{x}$(t):

From the value of the *Autocovariance* function on the diagonal C(t,t), we can deduct the *variance equation* of the process (Papadopoulos and Giovanis, 2017):

$$Var\left(\underline{x}(t)\right) = C(t,t) = E\left[\left(\underline{x}(t) - \mu_x(t)\right)^2\right] \tag{2.7}$$

Normalizing the *Autocorrelation function* $R(t_1,t_2)$ by subtracting the mean and dividing by the variance we obtain the *autocorrelation coefficient* (Papadopoulos and Giovanis, 2017):

$$\rho(t_1, t_2) = \frac{C(t_1, t_2)}{\sqrt{C(t_1, t_1)}\sqrt{C(t_2, t_2)}} \quad with \quad |\rho(t_1, t_2)| \leq 1 \tag{2.8}$$

2.2.2 Stationarity and Ergodicity: Two main concepts

A main concept central to that of stochastic processes is the concept of stationarity, and non-stationarity vise-versa. Stationarity of a stochastic process can be defined in a *strict-sense* and in a *wide-sense* (Papoulis,1991):

- A stochastic process $\underline{x}$(t) is called *strict-sense stationary* if its statistical properties are invariant to a shift of time origin, i.e. the processes $\underline{x}$(t) and $\underline{x}$(t+c) have the same statistics for any c. Two processes $\underline{x}$(t) and $\underline{y}$(t) are called jointly stationary if the joint statistics of $\underline{x}$(t) and $\underline{y}$(t) are the same as the joint statistics of $\underline{x}$(t+c) and $\underline{y}$(t+c) for any c. A complex process $\underline{z}$(t) = $\underline{x}$(t) + j$\underline{y}$(t) is stationary if the processes $\underline{x}$(t) and $\underline{y}$(t) are jointly stationary.

- A stochastic process x(t) is called *wide-sense stationary* if its mean is constant

$$E[x(t)] = \eta \tag{2.9}$$

and its autocorrelation depends only on $\tau = t_1-t_2$

$$E[x(t+\tau)x^*(t)] = R(t) \tag{2.10}$$

The variance Var($\underline{x}$(t)) of a stationary process remains also constant.

The concepts of stationarity and non-stationarity in geophysical processes, have been thoroughly discussed in the past (Milly et al., 2008; Montanari and Koutsoyiannis, 2014). An important

question raised in the referenced studies is whether the alteration of general climatic behaviour affects the assumption of stationarity of modelled natural time-series e.g. their constant mean value, and autocorrelation dependence, as stated before. We will assume here a stationary conception of the past observed data used in the study. We also do not consider non-stationarity to be synonym with "change" and stationarity with its opposite. On the contrary, admitting stationarity of the past data allows to model the future stochastically (thus invoking greater uncertainty), when a non-stationary assumption would imply a thesis for the ability of the deterministic prediction of the future, which is neither the goal nor the element of this study (Koutsoyiannis and Montanari, 2015)

Another important concept of stochastics is the one of *ergodicity.*

A stochastic process $\underline{x}(t)$ is considered *ergodic* if the time average of any (integrable) function $g(\underline{x}(t))$, as time tends to infinity, equals the true (ensemble) expectation $E[g(\underline{x}(t))]$ (Papoulis 1991 p. 427), which is expressed by:

$$\lim_{T\to\infty} \frac{1}{T} \int_0^T g\left(\underline{x}(t)\right) dt = E\left[g\left(\underline{x}(t)\right)\right] \tag{2.11}$$

As a result, when considering *deterministic systems*, a stationary system is also ergodic and vice versa, and a nonstationary system is also nonergodic and vice versa (Mackey, 1992). On the other hand when considering *stochastic systems* then ergodicity and stationarity do not necessarily coincide. However, recalling that a stochastic process is a model and not part of the real world, we can always conveniently device a stochastic process that is ergodic (see example in Koutsoyiannis and Montanari, 2015). *Ergodicity* can therefore be assumed if there is *stationarity*. Thus, here we consider the time-series modelled to be ergodic, as the assumption of stationarity has been accepted before.

2.3 Stochastic processes: realization and observation

Synthetic time-series can be used to depict a natural process. An important distinction when modelling natural processes comes from the divergence between their *evolution or realization* and their *observation*. While natural processes evolve in continuous time, observation and generation of synthetic time series are only made in discrete time, thus discrete-time processes need to be considered, and the effect of discretization on the processes to be accounted for.

This discretization is illustrated in Figure 2.1 were two different *discrete-time* processes are defined from the continuous time process (with discrete time denoted as *i)* (Koutsoyiannis, 2016)

By sampling at spacing Δ we obtain the sampled instantaneous process:

$$\underline{x_i} := \underline{x}(i\Delta) \tag{2.12}$$

By averaging at time scale Δ we obtain the averaged process:

$$\underline{x_i}^{(\Delta)} := \frac{\underline{X}(i\Delta) - \underline{X}\big((i-1)\Delta\big)}{\Delta} \tag{2.13}$$

where

$$\underline{X}(t) := \int_0^t \underline{x}\,(\xi)d\xi \tag{2.14}$$

X(t) is the *cumulative*, non-stationary process, shown in the first window of Figure 2.1. On the contrary both the sample *instantaneous* process $\underline{x}_i$ and the *averaged* process $\underline{x}_i^{(\Delta)}$, are stationary, and are depicted on the second and third windows of Figure 2.1 respectively.

From these two stationary processes we can construct the non-stationary, cumulative processes at discrete time *i*: namely, that of $\underline{x}_i^{(\Delta)}$is precisely X(iΔ)/Δ, while that of $\underline{x}_i$, is different, i.e. (Koutsoyiannis, 2016):

$$\underline{X_i} := \sum_{j=1}^{i} \underline{x_j} \tag{2.15}$$

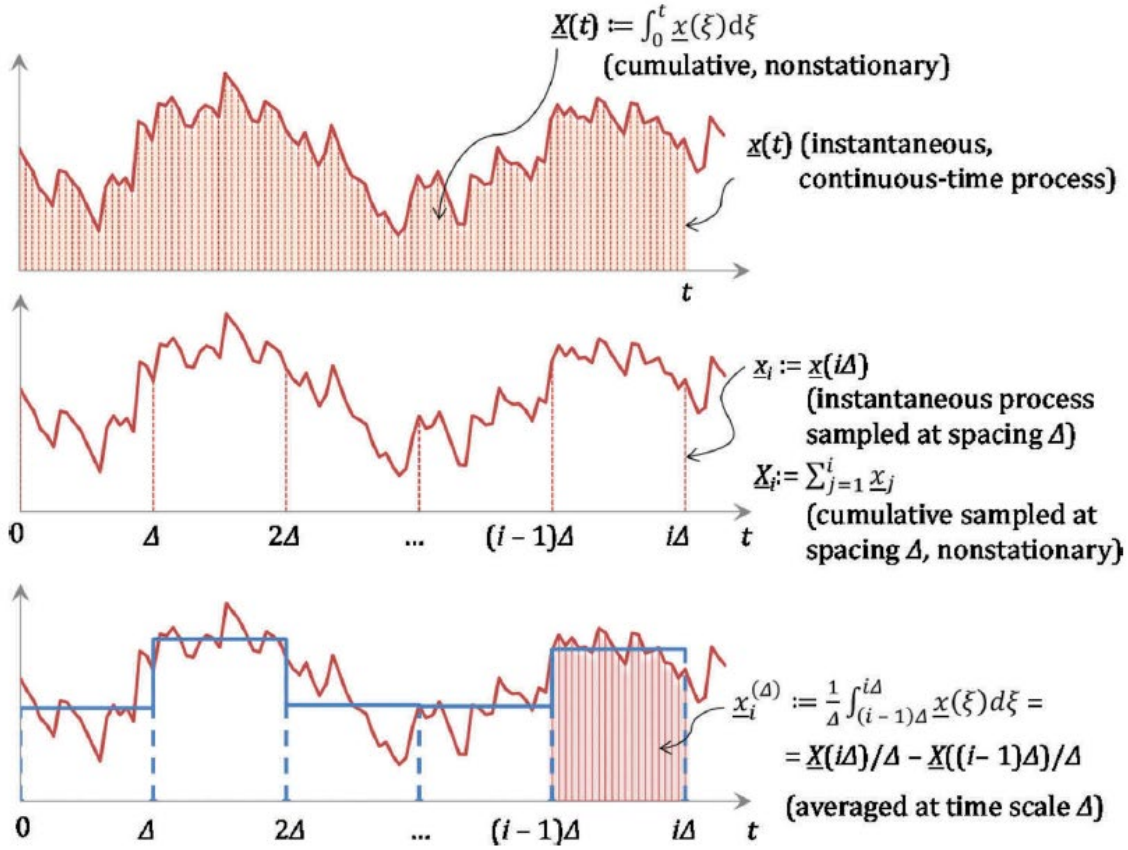

Figure 2.1: Explanation sketch of the definitions. Source: Koutsoyiannis (2016)

2.4 The climacogram: a useful tool for modelling time series

A main tool used in this study, to examine the long-term properties of the modelled time series is called the climacogram. As stated in Dimitriadis and Koutsoyiannis (2015):

> The climacogram (Koutsoyiannis 2013a) comes from the Greek word climax (meaning scale). It is defined as the (plot of) variance of the averaged process $\underline{x}(t)$ (assuming stationary) versus averaging time scale m and is symbolized by $\gamma(m)$. The climacogram is useful for detecting the long-term change (or else dependence, persistence, clustering) of a process.

The climacogram consists a simple, yet extremely useful tool, with similarities but also advantages over similar tools such as the power spectrum, the variogram and others (Koutsoyiannis and Dimitriadis, 2015). Its mathematical definition is given below, while later the depiction of persistence parameters through the climacogram is explained.

For a *continuous time process* the climacogram is defined as (Dimitriadis and Koutsoyiannis, 2015):

$$\gamma(m) := \frac{Var[\int_t^{t+m} \underline{x}(\xi)d\xi]}{m^2} = \frac{Var[\int_0^{m} \underline{x}(\xi)d\xi]}{m^2} \tag{2.16}$$

$$where \quad m \in \mathbb{R}^+ \quad and \quad \gamma(0) := Var[\underline{x}(t)]$$

For a *discrete time process* the climacogram is defined as (Dimitriadis and Koutsoyiannis , 2015):

$$\gamma_k^{(\Delta)}(k) := \frac{Var\left[\sum_{l=k(i-1)+1}^{ki} \underline{x}_l^{(\Delta)}\right]}{k^2} = \frac{Var\left[\sum_{l=1}^{k} \underline{x}_l^{(\Delta)}\right]}{k^2} = \gamma(k\Delta) \tag{2.17}$$

$$where \quad k \in \mathbb{N} \quad is\ the\ dimensionless\ scale\ for\ a\ discrete\ time\ process$$

The climacogram of the cumulative process stated below can also be derived but is not used for the purposes of this study.

2.5 Memory and Long-Term Persistence in Stochastic Processes

As described in chapter one, memory and long-term persistence is not just omni-present in natural processes but is an intrinsic characteristic of change and the concept of a “process” itself. Therefore, modelling natural processes must combine the parsimony element, described above in this chapter, with the dependence of the future on the past evolution of the modelled

variable(s) and the inclusion and quantification of the uncertainty parameter. In this section we refer to two main categories of stochastic processes and their corresponding mathematical models depicting natural processes: The Markov and the Hurst-Kolmogorov Process

2.5.1 The Markov Process

A Markov process is a process in which the future does not depend on the past when the present is known (Papoulis, 1991). The second order properties of the Markov Process are described in Table 2.1 for the instantaneous, the average process at scale Δ, and the sampled process at scale kΔ (Koutsoyiannis, 2016). The autocovariance function of the process is a pure exponential function (equation (T1.4) in Table 1), in which λ (dimension $[x]^2$) is a state-scale parameter and α (dimension [t]) is a time-scale parameter.

By inspecting Table 1 and comparing with known equations in the time-series literature, it is seen that in discrete time the process is identical to an AR(1) process if it is sampled at equidistant times, or a special case of an ARMA(1,1) process if it is averaged at time windows with constant length.

The Markov process follows the rules of simplicity in all its second order formulas, as well as parsimony, as it contains only one parameter, α, except those that describe its marginal distribution.

The Markovian assumption of the independence of the future on the past, at a certain point of present observation, is an abstract assumption, not verified in observation of natural processes. This does not imply that Markov based models, offer a poor resemblance of natural processes, rather that, they should be used on certain simplifications of reality, where the past factor is a priori neglected.

Table 2.1: Second-Order properties of the Markov Process

Process Type	Formula	Reference
	Variance	
Continuous-time and sampled process (Instantaneous)	$\gamma_0 = \gamma(0) = c(0) = \breve{\gamma}_0 = \lambda$	T1.1
Averaged process, scale Δ (Climacogram)	$\gamma(\Delta) = \frac{2\lambda}{\Delta/\alpha}\left(1 - \frac{1-e^{-\Delta/\alpha}}{\Delta/\alpha}\right)$	T1.2
Sampled process, scale kΔ (Climacogram)	$\breve{\gamma}^{(k)} = \frac{\lambda}{k(1-\rho)^2}\left(1 - \rho^2 - \frac{2\rho(1-\rho^k)}{k}\right)$ $k = 1,2,\ldots \; and \; \rho = e^{-\Delta/\alpha}$	T1.3
	Autocovariance Function	
Continuous-time process, lag τ	$c(t) = \lambda e^{-\tau/\alpha}$	T1.4
Averaged process, lag τ=jΔ	$c_j^{(\Delta)} = \frac{\lambda(1-e^{-\Delta/\alpha})^2}{(\Delta/\alpha)^2} e^{-(j-1)\Delta/\alpha}$, $j = 1,2,\ldots,$	T1.5
Sampled process, lag τ=jΔ	$\breve{c}_j = \lambda e^{-j\Delta/\alpha} = \lambda\rho^j, j = 0,1,2,\ldots,$	T1.6

2.5.1 The Hurst-Kolmogorov Process

The *Hurst-Kolmogorov* (HK) process is defined based on its climacogram, which is a power function of time scale, for an averaged process at scale Δ (Equation (T2.2) in Table 2.2) (Koutsoyiannis, 2016) . The autocovariance function is then easily determined (Equations (T2.3) and (T2.4) in Table 2.2).

The process in continuous time is also known as fractional Gaussian noise (FGN) due to Mandelbrot and van Ness (1968), although these authors used a more complicated approach to define it. In essence, though, the mathematical process had been earlier proposed by Kolmogorov (1940), while Hurst (1951) pioneered the detection in geophysical time series of the *persistence* behaviour described by this process. The name of this process refers to the names of these two pioneers (Koutsoyiannis, 2011), referenced also in Chapter 1. Because this process has infinite instantaneous variance, the sampled process in discrete time is not meaningful (many properties take infinite values). However, the averaged process is well behaved, with all of its properties (including its variance) finite, which makes it quite useful in applications.

The HK process is almost equally as simple and parsimonious as the Markov process; again, it contains only one parameter, the *Hurst coefficient*, symbolized with *H*, in addition to those describing its marginal distribution[3]. Despite that, we use the formulation shown in Table 2.2 (Koutsoyiannis, 2016) with three nominal parameters for dimensional consistency: α and λ are scale parameters with dimensions [t] and $[x]^2$, respectively, while *H*, the Hurst coefficient, is dimensionless in the interval (0,1).

Specifically, the values of the Hurst coefficient depict the persistence effect on the process:

- For $H = 0.5$ the process reduces to pure white noise.
- For $0.5 < H < 1$ the process exhibits Long-Term Persistence (or Long-Range Dependence) and is called a persistent process.
- For $0 < H < 0.5$ it is called an anti-persistent process.

A persistent process has a long-term positive autocorrelation, depicting that high and low values will cluster in time, which means that a high value will more probably be followed by another high value and the next values for a long future range will also tend to be high. An anti-persistent process has the exactly opposite effect, depicting a long-term "switch" between high and low values, meaning that a high value will probably be followed by a low value and vice-versa, with this tendency lasting for a long future range. A process with H=0.5 indicates a completely uncorrelated process. In practice a process with *H* close to the value of 0.5 can have an autocorrelation for very small lag values but will decay exponentially and quickly to zero. This

[3] Notice that the process variance is controlled by the product $\lambda*\alpha^{2-2H}$, so that λ and α are not in fact separate parameters.

is the case of the Markov Process examined before, making it essentially a sub-case of the Hurst-Kolmogorov process (Koutsoyiannis, 2002).

Most of the expressions shown in Table 2 are valid in the all cases. However, the autocovariance $c(\tau)$ has different expressions in the three cases, as shown in Table 2. Specifically, for $H < 0.5$, the autocovariance $c(\tau)$ is negative for any lag $\tau > 0$, tending to $-\infty$ as $\tau \to 0$. However, at $\tau = 0$, $c(0) = +\infty$, because this is the variance of a process that cannot be negative; thus, there is a discontinuity at $\tau = 0$. Consequently, the averaged process has positive variance and all covariances negative. Such a process is not physically realistic because real-world events at near times are always positively correlated, which means that for small τ, $c(\tau)$ should be positive. Also, the infinite variance cannot appear in nature (it would be associated with infinite energy); even the white noise, whose autocovariance is a Dirac delta function (corresponding to infinite variance, see (T2.3) for $H = 1/2$), cannot describe a natural process. Thus, the HK process can describe natural phenomena only for $0.5 < H < 1$ and for time scales not too small.

It is also noted that certain studies, utilizing different methods for the calculation of the Hurst Coefficient (such as the "DFA2" method) report values of $H > 1$. This is considered by Koutsoyiannis (2013b), as theoretically and mathematically inconsistent, and differs from the approach adopted here.

Table 2.1: Second-Order properties of the Hurst-Kolmogorov Process

Process Type	Formula	Reference
	Variance	
Continuous-time and sampled process (Instantaneous)	$\gamma_0 = \gamma(0) = c(0) = \breve{\gamma}_0 = +\infty$	T2.1
Averaged process, scale Δ (Climacogram)	$\gamma(\Delta) = \lambda(\alpha/\Delta)^{2-2H}$	T2.2
	Autocovariance Function	
Continuous-time process, lag τ	$c(t) = \lambda H(2H-1)(\alpha/\tau)^{2-2H}$ *(H>1/2)* $c(t) = \lambda\delta(\tau/\alpha)$ *(H=1/2)* $c(t) = \lambda H(2H-1)(\alpha/\tau)^{2-2H} + \delta''(\tau/\alpha)$ *(H<1/2)*	T2.3
Averaged process, lag $\tau=j\Delta$	$c_j^{(\Delta)} = \lambda(\alpha/\Delta)^{2-2H}\left(\frac{\lvert j-1\rvert^{2H} + \lvert j+1\rvert^{2H}}{2} - \lvert j\rvert^{2H}\right)$	T2.4

2.5 Generation of synthetic time-series

The random element of a synthetic time-series consists of a white noise function, in which different X_i are independent identically distributed random variables, so that $\gamma_j=0$ (and $\rho_j=0$) for $j\neq 0$. Then the aggregated process at time scale k has variance:

$$\gamma_0^{(k)} := var\left[Z_I^{(k)}\right] = k\gamma_0 \tag{2.18}$$

autocovariance $\gamma_j^{(k)}=0$ and autocorrelation $\rho_j^{(k)}=0$.

Synthetic time series can be generated by certain stochastic models which contain and a random element and preserve certain characteristics of the modelled time series. Various models exist in the bibliography, namely AR(1), AR(2), ARMA(1,1), ARFIMA(1,1), SMA, FGN and many others.

Here we compare models on their ability preserve the second-order properties described in the previous section, namely the autocovariance and autocorrelation function, not only on the original scale k of the original time-series but on (higher) aggregated scales Δk. This essentially means preserving the Long-Term Persistence ("LTP") of the original process, or elseway its behaviour as Hurst-Kolmogorov process (HK behaviour) as defined above.

We define the aggregated stochastic process at time scale k as $Z_i^{(k)}$ where (Koutsoyiannis 2002):

$$Z_i^{(k)} = \sum_{l=(i-1)k+1}^{ik} X_l \tag{2.19}$$

It follows that for k=1, $Z_i^{(1)} = X_i$; for $k=2$, $Z_1^{(2)} = X_1 + X_2$, $Z_2^{(2)} = X_3 + X_4$ *etc.*

The statistical properties of the aggregated process Zi are derived from those of the process Xi:

The mean is calculated as:

$$E\left[Z_I^{(k)}\right] = k\mu \tag{2.20}$$

while the variance and autocovariance (or autocorrelation) is calculated as:

$$\gamma_j^{(k)} := cov\left[Z_i^{(k)}, Z_{i+j}^{(k)}\right] = \sum_{l=1}^{k}\sum_{m=jk+1}^{(j+1)k} \gamma_{m-1}\,, \qquad j = 0, \pm 1, \pm 2, \ldots. \tag{2.21}$$

Here we will compare two models, whose main difference is the ability to preserve the LTP, or else the HK behaviour found in the original time series: The AR(1) model which fails to do so, and the Fractional Gaussian Noise (FGN) model, a model consisting of a sum of AR(1) models

which preserves the Hurst value along with other properties. We also seek a model to replicate the climacogram values of a harmonic process i.e. a pure deterministic one.

2.5.1 The AR(1) Model

The AR(1) model has the simplest possible introduction of a Markov-type memory, added to the white noise function. In the AR(1) model the dependence of the current value to its previous one is assumed. This dependence is expressed on the basic time scale in the equation of the AR(1) model where:

$$X_i = \rho X_{i-1} + V_i \tag{2.22}$$

where ρ is the lag one autocorrelation coefficient (-1 < ρ < 1) and V_i (i=1,2,…) are independent, identically distributed, random variables with mean (1-ρ) and variance $(1-\rho^2)\gamma_0$. The process is Markovian because the dependence of the current variable X_i on the previous variable X*i-1* suffices to express completely the dependence of the present on the past. The autocorrelation of X*i*, is:

$$\rho_j := \text{corr}[X_i, X_{i+j}] = \rho^{|j|} \tag{2.23}$$

Through the climacogram of the aggregated process shown in equation (2.21), and by combining it with equation (2.23), it can be shown that the aggregated process has variance (Koutsoyiannis 2002):

$$\gamma_0^{(k)} = \gamma_0 \frac{k(1-\rho^2) - 2\rho(1-\rho^k)}{(1-\rho)^2}, \quad \gamma_j^{(k)} = \gamma_0 \frac{\rho^{kj-k+1}(1-\rho^k)^2}{(1-\rho)^2}, \quad j \geq 1 \tag{2.24}$$

and autocorrelation:

$$\rho_1^{(k)} = \frac{\rho(1-\rho^k)^2}{k(1-\rho^2) - 2\rho(1-\rho^k)}, \quad \rho_j^{(k)} = \rho_j^{(k)} \rho^{k(j-1)}, \quad j \geq 1 \tag{2.25}$$

The autocovariance equation (2.24) is similar with the one of T1.3 for Markov processes. The last, autocorrelation equation (2.25), compared with eq. (2.23), shows that the aggregated process (2.19), is no longer a Markovian process but a more complicated one (certainly, equation (2.25) coresponds an ARMA(1,1) process (Box et al., 2015). This means that the simple AR(1) process, follows an AR(1) model only on its basic time scales, becoming more complicated on aggregated, higher time scales. Notably, for a large aggregated time scale *k*, the numerator of equation (2.24) is dominated by the first term, and the variance of the aggregated process becomes:

$$\gamma_0^{(k)} \approx k \frac{1+\rho}{1-\rho} \gamma_0 \tag{2.26}$$

i.e. it becomes proportional to the time scale *k*, similarly as in the white noise process. This depicted in the visualization of the climacogram of an AR(1) process, which rapidly reaches the theoretical climacogram of a white noise process, in aggregated time scales. This effect will be shown later on in this chapter.

2.5.2 The FGN Model

The AR(1) model is therefore unable to reproduce natural persistence, in modelling experiments, when not only the simplest scale values (close to the original scale k) are required. When the synthetic AR(1) model reaches the white noise behaviour, it essentially ignores the low-frequency signals from high aggregated time scales, «hidden» in the original time-series, and does not reproduce them, losing the element of reproducing persistence found in the original time series.

To restore consistency with reality, Mandelbrot (1965) introduced the process known as fractional Gaussian noise (FGN). Fractional Gaussian noise can be defined in discrete time in a manner similar to that used in continuous time (Peitgen and Saupe, 1988) Specifically, FGN can be defined as a process satisfying the condition:

$$\left(Z_i^{(k)} - k\mu\right) \overset{d}{=} \left(\frac{k}{l}\right)^H \left(Z_j^{(k)} - l\mu\right) \tag{2.27}$$

where the symbol $\overset{d}{=}$ stands for equality in (finite-dimensional joint) distribution and *H* is the Hurst coefficient. Equation (2.27) is valid for any integer *i* and *j* (that is, the process is stationary) and any time scales *k* and *l.* As a consequence, for *i=j=l=1* one obtains:

$$\gamma_0^{(k)} = k^{2H}\gamma_0 \tag{2.28}$$

Thus, the standard deviation is a power law of *k* with exponent *H,* which agrees with the observation on the real-world cases described above. The extremely simple equation (2.28) can serve as the basis for estimating *H* (Montanari *et al.,* 1997, Koutsoyiannis 2002) has shown that, for any aggregated time scale *k,* the autocovariance function is independent of *k,* i.e.

$$\rho_j^{(k)} = \rho_j = (1/2)[(j+1)^{2H} + (j-1)^{2H}] - j^{2H}, \qquad j > 0 \tag{2.29}$$

Apart from small *j,* the above function is very well approximated by:

$$\rho_j^{(k)} = \rho_j = H(2H-1)j^{2H-2} \tag{2.30}$$

which is the HK model introduced in equation (T2.3) for H>0.5 and without the scaling parameters.

The Hurst coefficient H is for the FGN model the parameter used to express the correlation structure of the model, as how in the AR(1) model the autocorrelation coefficient ρ serves for

the same purpose. It has been discussed in (Koutsoyiannis, 2002) that the sum of three AR(1) models with according coefficients depicting the correlation structure named ρ, φ and ξ the correlation structure of an FGN process W_i can be expressed as:

$$W_i = X_i^1 + X_i^2 + X_i^3 + \mu \tag{2.31}$$

where μ is the mean value of the original, stationary time-series and X_i^1, X_i^2, X_i^3 are three AR(1) processes with factors ρ, φ and ξ respectively:

$$X_i^1 = \rho X_{i-1}^1 + V_i\,, \quad X_i^2 = \varphi X_{i-1}^2 + V_i, \quad X_i^3 = \xi X_{i-1}^3 + V_i \tag{2.32}$$

Note that here the superscript numbers do not refer to the scale k of the process, but rather to the numbering of the combined AR(1) models. As stated in (Koutsoyiannis, 2002), the choice of three AR(1) processes suffices for modelling synthetic time-series, up to a certain length n of values while mainting a certain level of accuracy. The number of process is kept to 3 (small number) to achieve simplicity in the model, which, while close to the Fast Fractional Gaussian Noice (FFGN) algorithm (Mandelbrot, 1971), it is much simpler, in terms of components and calculation equations. Raising the number of AR(1) models allows for a more certain reproduction of the statistical properties and the Hurst Coefficient of the modelled time-series, by a longer (in length n) synthetic time-series

It is also shown in the study of (Koutsoyiannis, 2002) that the FGN process has a correlation structure of:

$$corr[W_i, W_{i+j}] = (1 - c_1 - c_2)\rho^j + c_1\varphi^j + c_2\xi^j \tag{2.33}$$

where ρ, φ and ξ are the model. parameters and c_1, c_2 positive constants with $c_1 + c_2 < 1$

The same study has proposed a simple system to calculate the parameters of the FGN model:

$$\rho = 1.52(H - 0.5)^{1.32} \tag{2.34}$$

$$\varphi = 0.953 - 7.69(1 - H)^{3.85} \tag{2.35}$$

$$\xi = \begin{cases} 0.932 + 0.087 & H \le 0.76 \\ 0.993 + 0.007H & H > 0.76 \end{cases} \tag{2.36}$$

the remaining parameters c_1 and $c_{2\,f}$ can be estimated such that the approximate autocorrelation function (equation (2.33)) matches the exact function (equation 2.29) for two lags, e.g. lags 1 and 100.

2.5.3 The harmonic model

It has been shown in (Markonis and Koutsoyiannis, 2013) that a fully deterministic, strictly periodic process composed of a single harmonic with period T has a climacogram of the form:

$$\sigma^{(k)} = \left|sinc\left(\frac{k}{T}\right)\right| = \left[\frac{T}{(\pi k)}\right]\left|\sin\left(\frac{\pi k}{T}\right)\right| \tag{2.37}$$

where sincdenotes the normalized sine-counting function.

We transcript here the proof of the above equation as shown in Markonis and Koutsoyiannis (2013).

We assume a fully deterministic, strictly periodic process composed of a single harmonic with period T, described by:

$$x(t) = \sqrt{2}\cos\left(\frac{2\pi t}{T} + b\right) \tag{2.38}$$

It can be seen that during the time interval $[t_1, t_2]$, where $2\pi t_{1,2}/T+b=\pm\arccos(x/\sqrt{2})$, the process $\underline{x}(t)$ takes on values greater than or equal to x, provided that $-\sqrt{2}\leq x\leq\sqrt{2}$ (see Figure 2.2).The length of the interval $[t_1, t_2]$, is $(T/\pi)\arccos(x/\sqrt{2})$. Consequently, if we treat the process $x(t)$ stochastically, it follows that its marginal distribution function is:

$$F(x) = 1 - \frac{\cos^{-1}\left(\frac{x}{\sqrt{2}}\right)}{\pi}, \qquad -\sqrt{2} \leq x \leq \sqrt{2} \tag{2.39}$$

Taking its derivative with respect to x, we find its marginal density function as:

$$f(x) = \frac{1}{\pi\sqrt{2 - x^2}}, \qquad -\sqrt{2} \leq x \leq \sqrt{2} \tag{2.40}$$

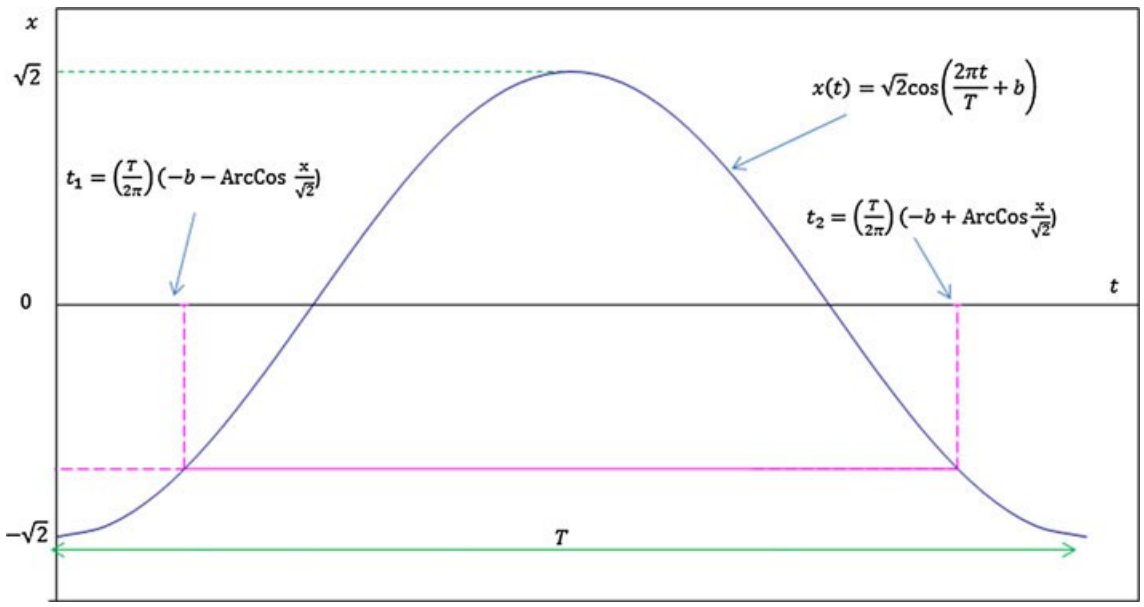

Figure 2.2 Sketch to illustrate the proof of (2.39). For the ease of the illustration, it was assumed b = p, but this does not affect the result nor the length of the time interval, which does not depend on b. Source: Markonis and Koutsoyiannis (2013)

By application of definitions of mean and variance, we readily obtain that the mean of the process is 0, and its variance is 1. Likewise, the process autocovariance is:

$$R(\tau) = cov\left[\underline{x}(t), \underline{x}(t+\tau)\right] = E\left[\underline{x}(t), \underline{x}(t+\tau)\right] \tag{2.41}$$

where τ is lag time. If x(t) = x then t=(T/2π)[−b+arccos(x/√2)] (one of the infinitely many possibilities), so that t+τ=(T/2π)[−b+arccos(x/√2)]+τ and x(t+τ)=√cos[2πτ/T+arccos(x/√2)] Consequently:

$$R(\tau) = \sqrt{2}\int_{-\sqrt{2}}^{\sqrt{2}} x \cos\left[\frac{2\pi\tau}{T} + \cos^{-1}\left(\frac{x}{\sqrt{2}}\right)\right] \tag{2.42}$$

which after algebraic manipulations becomes

$$R(\tau) = \cos\left(\frac{2\pi\tau}{T}\right) \tag{2.43}$$

Interestingly, this does not depend on t, thus behaving like a stationary process.

The climacogram value at scale k can be calculated from the variance Var [$\underline{x}_i^{(k)}$], that is,

$$Var\left[\underline{x}_i^{(k)}\right] = E\left[\left\{\underline{x}_i^{(k)}\right\}^2\right] = \frac{1}{k^2}\int_0^k\int E[x(t)x(s)]dtds \tag{2.44}$$

Or

$$Var\left[\underline{x}_i^{(k)}\right] = \frac{1}{k^2}\int_0^k\int R(t-s)dtds = \frac{1}{k^2}\int_0^k\int \cos\left[\frac{2\pi(t-s)}{T}\right]dtds \tag{2.45}$$

which after algebraic manipulations becomes:

$$Var\left[\underline{x}_i^{(k)}\right] = \left[\frac{T}{\pi k}\right]^2 \sin^2\left(\frac{\pi k}{T}\right) \tag{2.46}$$

By taking the square root of Var [$\underline{x}_i^{(k)}$], which by definition is the standard deviation σ(k), this gives equation (2.37).

From equation (2.37), we readily infer, that for increasing k, there appears a series of maxima at values $k = \alpha T/2$, with α any odd integer, so that $|sin(\pi k/T)| = 1$. This series is described by $\sigma^{(k)} = T/(\pi k)$, which is an upper envelope curve of the climacogram. Obviously, across this envelope, $\theta = d(\ln\sigma^{(k)})/d(\ln k) = -1$. However, the local slope of the climacogram is not constant but varies. We can easily determine it from:

$$\begin{aligned}\theta &:= d(ln\sigma^{(k)})/d(lnk) = (k/2)d\{\ln[(\sigma^{(k)})^2]\}/dk \\ &= (k/2)d\left(\frac{ln\left\{\left[\frac{T}{\pi k}\right]^2 sin^2\left(\frac{\pi k}{T}\right)\right\}}{dk}\right.\end{aligned} \tag{2.47}$$

which after algebraic manipulations becomes

$$\theta = \left(\frac{\pi k}{T}\right) cot\left(\frac{\pi k}{T}\right) - 1 \tag{2.48}$$

it can be seen that θ tends to $\pm\infty$ whenever k/T is integer.

2.6 Examining LTP of time series through the climacogram

2.6.1 A showcase of different processes on the climacogram

The value of the Hurst coefficient, depicting the persistence of the time series ("persistent", "white-noise" or "anti-persistent"), and/or the existence of Long-Term Persistence or HK behaviour, is shown as the slope of a simple straight line in the log-log plot of the climacogram. That is easily derived from the equation (T2.2) where the value *2-2H* is the exponent of the variance function, leading thus to a slope of 1-H in the climacogram. Altering the values of α and λ do not change the slope of the line. The climacogram can be plotted with either with the log of the variance or the standard deviation on its y axis. For the latter the equation (T2.2) is square-rooted, giving an exponent of *1-H* which is the slope of the standard-deviation climacogram.

On the climacogram we call *theoretical* the processes following a certain mathematically defined behaviour (such as HK, or AR(1) models), *synthetic* the processes which are generated through a stochastic model, by modelling an observed, historical time-series and *empirical* the processes which depict historical, observed time-series. We respectively name the climacograms of the processes as: *theoretical climacogram*, *synthetic climacogram* or *empirical climacogram.*

Here we portray the processes analysed in section 2.5, both theoretical and synthetic, in a climacogram plot. Two random windows of synthetic time series with a length of 10000 data are plotted. The first one belongs to a time series generated through an *AR*(1) model with mean value μ_v=0, standard deviation σ_v=1 and first-lag autocorrelation factor $\rho(1)$=0.75. The second one, is an *FGN* model, created through the sum of 3 (three) *AR*(1) models, with identical properties with the previous visualized one, and the methodology described above for the preservation of the HK behaviour through the Hurst Coefficient, which is chosen as H=0.8 for the modelled historical time-series. The straight lines depicting a simple theoretical model with HK behaviour, and a Hurst coefficient of H=0.8, following equation (T2.2), and a theoretical model with H=0.5 which is identical with the *White Noise* behaviour. This is visualized in the plots of Figure (2.3). On the one hand, the *AR*(1) model shows an initial slope close that of the theoretical HK, which very rapidly (in ~10 climacogram values) drops to a slope close to that of the *White Noise*, with the climacogram slope falling to -0.5 (H=0.5). This is essentially the picture of a Markov process behaviour on the climacogram, as discussed above. On the other hand, the *FGN* model manages to preserve the initially chosen Hurst coefficient, as the slope of the climacogram reaches almost the value of -0.2, which is the slope of the theoretical model (H=0.8). The slope of the theoretical model, in the case of the *FGN* model is the highest possible envelop of the generated synthetic time series (not concerning the bias of the synthetic time series). Thus, it can be said that the FGN model can represent an HK process.

The climacogram of a harmonic, deterministic function with T=100 years, is also plotted in Figure (2.3), along with its envelope which has a slope of -1, therefore refers to a theoretical HK model with H=0. This will be later used in this study to depict deterministic signals contained in a modelled historic time series, which can be combined with a stochastic one following an HK for a better understanding of the components of a process.

2.6.2. The combined climacogram

Certain studies, as are those of Markonis and Koutsoyiannis (2013) and of Pappas and Koutsoyiannis (2017) have utilized a tool named *combined climacogram* in order to jointly visualize the climacogram of time-series recorded on different scales, on the same log-log plot of aggregated variance (or standard deviation), against the averaged scale.

Each of the different time series, allows the construction of an empirical climacogram for aggregate scales k spanning from the available resolution Δ up to k = L/10 (with L being the total length of each of the time series). With the latter choice, the sample of the averaged process $\underline{x}^{(k)}$ has at least 10 data points for the estimation of $\sigma^{(k)}$, as proposed by Koutsoyiannis (2002).

Thus, to construct the empirical climacogram, an averaged time series for each scale is (k = 1, 2, 3, ⋯, L/10) and then the sample estimate of the standard deviation $\sigma^{(k)}$ are calculated.

The processes $x(t)$ undergo different linear transformations in order to be visualized into the combined climacogram. As the processes mapped on the climacogram measure the same parameter, all the different processed time series can be seen as proxies of a variable $\underline{y}(t)$ (e.g. global sea level rise on multiple scales, see Chapter 3). These processes are considered to be intrinsically related, and as an approximation, we can assume that they are linearly connected. This can be expressed through:

$$y(t) = a_x x(t) + b_x \tag{2.49}$$

where $x(t)$ represents any of the proxy variables and α_x is a correction factor of linear transformation.

It follows therefore that:

$$\sigma_y^{(k)} = \sigma_x^{(k)} \tag{2.50}$$

A factor that supports the approximation of linear connection can be the close match in variability through overlapping time scales, between the different proxy variables x(t).

The value of the correction factor α_x of the proxy on the smallest time scale is set so that the value of $\sigma_x^{(k)}$ equals 1, when k has the value of the time step of the time series, or the lowest aggregated time scale (essentially meaning that the combined climacogram begins from the value of standard deviation 1). The rest of the correction factors are calculated empirically or through the Generalized Reduced Gradient Method (Smith and Ladson, 1992), available on the EXCEL solver tool, to minimize the departures among the $\sigma_x^{(k)}$ of the different series $x(t)$ for the same scale k.

Specifically, characteristic time scales $k_l = 2^l$ years are chosen (by choosing a varying span of l) and each climacogram is interpolated at those points k_l that fall into the domain of the empirical climacogram. For each k_l, a sample of empirical climacogram values is formed, obtained by each of the different series that overlap at a range containing the point k_l. The standard deviation is the estimated at all points k_l and the sum of the standard deviations at each point k_l is minimized. Through this process a unique set of weights (or correction factors) α_x is obtained, through which the processes now appear on the climacogram as a unified process y(t), with a common standard deviation $\sigma_y^{(k)}$, for the different time scales k.

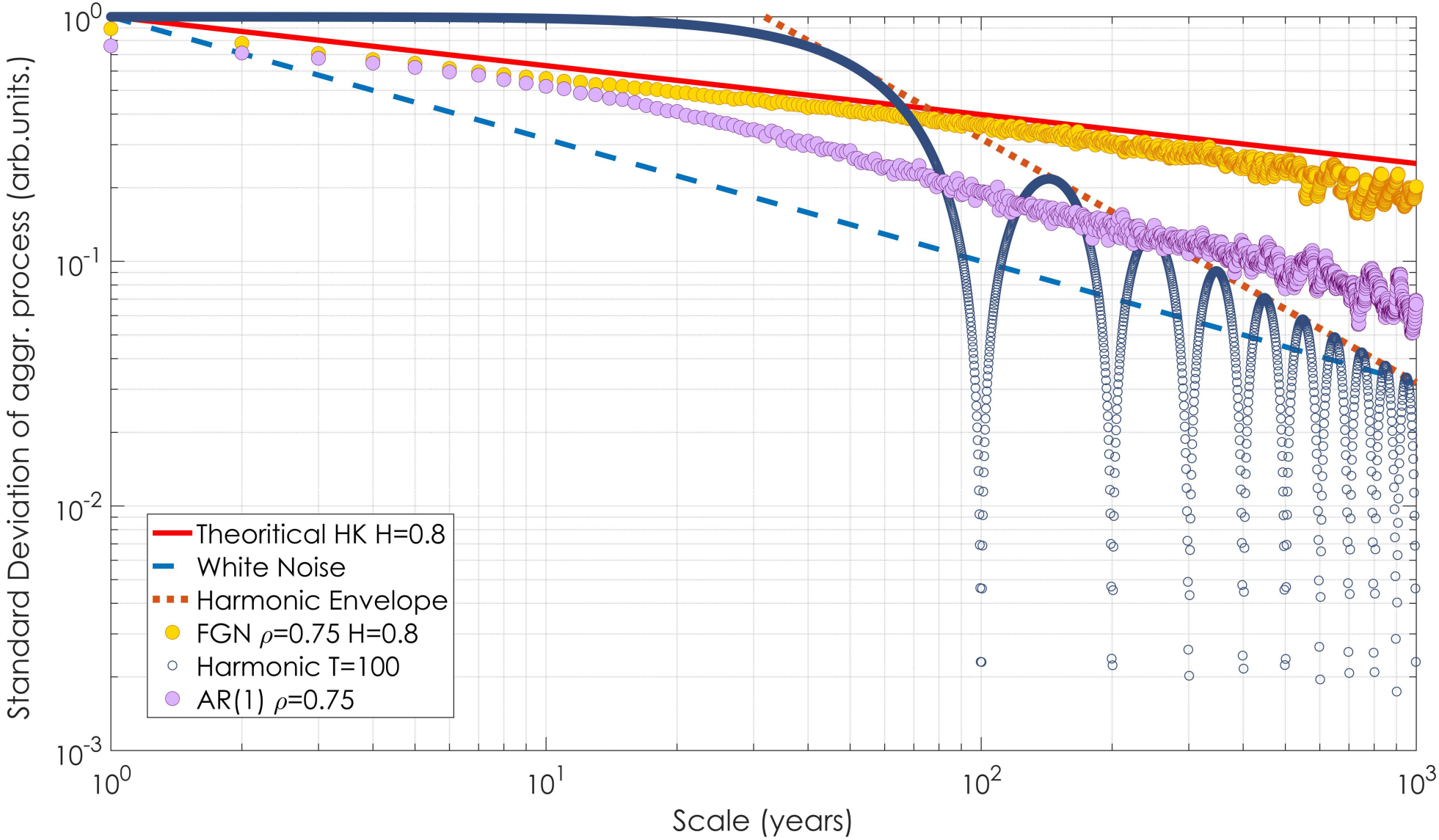

Figure 2.3: Portray of the basic processes, on the climacogram. The thick red line depicts a Theoretical HK process with H=0.8. The dashed blue line, depicts a theoretical White Noise process (corresponding to an HK model with H=0.5). The blue dots represent a theoretical Harmonic process with time period T=100 years, and the brown dotted line it's envelope. The purple filled circles represent a synthetic AR(1) process with length n=10000 years and autocorrelation factor of lag-1, ρ=0.75. The yellow filled circles represent a synthetic FGN process with length n=10000 years and autocorrelation factor of lag-1, ρ=0.75 and Hurst coefficient of H=0.8.

Chapter 3: Variability and Persistence in Sea-Level

3.1 Variability of the sea-level variable

In this study numerous sea-level rise records spanning from monthly to millennium scales are examined, in order to evaluate the variability of the sea-level variable across different time-scales. Many proxy time-series of sea-level measurements and reconstructions are utilized to create a record of variability spanning on a large number of scales. This is presented in the following section.

Sea-level has been a parameter of great interest for past and future climate evolution as it is both affected by other climatic variables such as ocean heat content and general temperature variations (Barth 1984, IPCC, 2013) but it also affects the general circulation of the planet as well as human environment, notably with the process of coastal erosion (Brunn et al., 1962, Leatherman et al. 2000).

On a short scale where carbon emission forcing on climatic and oceanic processes has been shown to contribute to the observed sea level rise, observations and projections are provided by the IPCC Fifth Assessment Report (IPCC, 2013). Additionally, many authors have analysed sea-level data of the last century to examine the relation between long-term natural variability and variability which could be attributed to anthropogenic origin.

On a large scale, reconstruction methods through proxy data have been utilized to estimate the sea-level record, on multiple past time-scales. The orbital theory and the theory of stochastic variability have been both used to examine climate variations as well as glaciation cycles and their effect on the sea-level record. Here we follow a recently adopted view of a combination of the two, namely the examination of deterministic oscillations and their alteration through time as well as the stochastic description of climatic variable fluctuations. The rules applied for climate can be applied for the sea-level parameter, following the method to model stochastic natural variables described in Chapter 2.

In this section we give a brief bibliographical review of the aforementioned cases.

3.1.1 Short scale: Natural and anthropogenic variability

According to IPCC Fifth Assessment Report, Chapter 3 (Rhein et al., 2013) *"it is virtually certain that globally averaged sea level has risen over the 20th century, with a very likely mean rate between 1900 and 2010 of 1.7 [1.5 to 1.9] mm yr^{-1} and 3.2 [2.8 and 3.6] mm yr^{-1} between 1993"*. Also, as stated in the same report, *"it is virtually certain that interannual and decadal changes in the large-scale winds and ocean circulation can cause significantly higher or lower rates over shorter periods at individual locations, as this has been observed in tide gauge records around the world."*

Regarding the anthropogenic forcing, the consideration of it as a deterministic forcing by the IPCC Fifth Assessment Report (Church et al. 2013), on the global sea-level values, allows for

the production of complex numerical models that resemble the geophysical processes affecting the natural variable and also incorporate anthropogenic forcing which are described through different Representative Concentration Pathway (RCP) scenarios. According to the Fifth Assessment Report, Chapter 13 (Church et al.2013), *"it is very likely that the rate of global mean sea level rise during the 21st century will exceed the rate observed during 1971– 2010 for all Representative Concentration Pathway (RCP) scenarios due to increases in ocean warming and loss of mass from glaciers and ice sheets. Projections of sea level rise are larger than in the AR4, primarily because of improved modelling of land-ice contributions. For the period 2081–2100 compared to 1986–2005, global mean sea level rise is likely (medium confidence) to be in the 5 to 95% range of projections from process- based models, which give 0.26 to 0.55 m for RCP2.6, 0.32 to 0.63 m for RCP4.5, 0.33 to 0.63 m for RCP6.0, and 0.45 to 0.82 m for RCP8.5. For RCP8.5, the rise by 2100 is 0.52 to 0.98 m with a rate during 2081–2100 of 8 to 16 mm yr^{-1}"*. Also, *"it is virtually certain that global mean sea level rise will continue beyond 2100, with sea level rise due to thermal expansion to continue for many centuries. The amount of longer term sea level rise depends on future emissions."*

Various studies have used methods which compare to, but have quite different axioms, from the ones used here, e.g. the examination of the Hurst parameter in time-series or the general estimation of the variability across different time scales:

Dangendorf et al. (2015) analysed both global and local sea level time-series data for the last century, to examine persistence (long-term correlations) in natural variability signals. This is done through a second-order detrended fluctuation analysis (DFA2) analysis method, which also incorporates the variance plot, but with a different definition of the Hurst parameter which allows it to reach values higher than 1, which in this study is considered naturally and mathematically inconsistent with basic stochastic definitions (for more see Koutsoyiannis (2013b)). This study separates the volumetric and atmospheric components of the local sea level time-series, which are measured through gauges around the world. It results that the fast-varying atmospheric component masks an important amount of natural persistence found in the slower varying, volumetric one. Additionally, such persistence is examined for the volumetric component for the global sea-level on most parts around the world. The study concludes the importance of persistence natural variation not taken before into account, but also considers the residue variation of sea-level (45% of the Global Sea-Level rise) as of anthropogenic origin.

In the same motive Dangendorf et al. (2014), Becker et al. (2014) and Marcos et al. (2017) both used a DFA2 analysis to seek persistence into local-sea level time-series obtained by different gauges around the globe, through a DFA2 method, to seek long-term correlations. Both of these studies also agree on a significant part of the examined local-sea level rise that cannot be adhered to a long-term correlation and is thus explained through forcings of anthropogenic origin.

Finally, Ercan et al (2013) used stochastic models, which model the "long-rage dependence" – the term the authors use for what we call long-term persistence here- in sea level time series, such as ARFIMA models. They apply this model to two case studies one of the Caspian Sea and another one of the Peninsular Malaysia and Sabah-Sarawak, to forecast possible future evolution of the sea level values. While our study does not move to the extent of setting up a stochastic model for the estimation of possible future scenarios based on the modeled data, it has a similar motive to that of Ercan et al., allowing for this logic to be used for future applications.

3.1.2 Large Scale: Orbital Theory and Stochastic Variability

The following section is excerpted and taken from Markonis and Koutsoyiannis (2013) explaining thoroughly orbital theory and stochastic variability in climate process, as well as their relation. As stated later, sea-level records which are presented here follow a common response to the glaciation cycles and their orbital causes described in orbital theory and can be thus described in terms of general climate. The aforementioned study is common in terms of methods and tools used to this one, while modelling different natural variables.

We use the term 'orbital theory', originally proposed by Bolshakov (2008), to describe the hypothesis that global climate is affected by changes in Earth's orbital characteristics, such as the eccentricity, the precession of the equinoxes and the axial tilt or obliquity, at scales ranging from 20 to 100 thousand years or even more (Berger 1978). This hypothesis was set forth by Milankovitch (1941), following the theoretical ideas of Adhemar and Croll (Imbrie 1982). According to it, the intensity of incoming solar radiation during the summer solstice at high latitudes (65°) of the Northern Hemisphere causes the glaciation and deglaciation periods. Direct insolation changes by eccentricity or insolation at the Southern Hemisphere are not regarded to have a clear effect on climate as underlined by several researchers (Imbrie et al. 1993; Liu and Chao 1998; Balshakov 2008; Huybers 2009), despite the fact that it has been shown that the glaciations were almost synchronous in both hemispheres (Kawamura et al. 2007). Rather, glaciation cycles are mainly affected by precession forcing (19 and 24 thousand years) and obliquity forcing (41 thousand years). Thorough reviews of the historical development of the theory, as well as a full description of the celestial mechanics, are presented by Imbrie (1982), Bolshakov (2008) and Paillard (2010).

Recently, the orbital climate theory has been challenged by several studies arguing that it cannot sufficiently describe the links between climate and insolation variations (Winograd et al. 1992; Muller and MacDonald 2000; Elkibbi and Rial 2001; Wunsch 2004; Bolshakov 2008). A well-known example of the weaknesses of the orbital theory is the mid-Pleistocene transition (MPT), which refers to the switch, around 900 thousand years BP, from predominant 41 thousand years glaciation cycles to 100 thousand years glaciation cycles This transition occurred without a corresponding change in orbital forcing (Pisias and Moore 1981), and the duration of each of the last four glacial cycles increased from 80 to 130 thousand years, which suggests that major climate shifts were aperiodic (Winograd et al. 1992). Till today, there is no confirmed explanation for MPT, although some efforts have been made and some hypotheses have been formulated, including those of a glacial-modulated threshold (Paillard 1998), frequency modulation (Rial 1999), possible CO2 correlation (Berger et al. 1999) and obliquity-modulated threshold (Huybers 2006).

An alternative path to the understanding of the global climate cycles was based on stochastic dynamics (Petersen and Larsen 1978; Kominz and Pisias 1979; Benzi et al. 1981; Saltzman 1982; Pelletier 2003; Ditlevsen 2009). In this concept, insolation forcing could have a minor role in the glaciation cycles, or even could have no role at all, whereas the self-sustained internal variability of the climate system could be the actual driver of the glaciations (Ashkenazy and Tziperman 2004). Small periodic perturbations could be amplified by the variability of the climate system through the mechanism of stochastic resonance (Benzi et al. 1981), which was based on the works of Hasselmann (1976) and Sutera (1981). The former demonstrated that short-time-scale phenomena, modelled as stochastic perturbations, could affect long-term climate variations. The latter showed that,

if such stochastic perturbations are imported into an energy balance model with no other forcing, they could lead to random transitions between the equilibrium states of the model.

In the last few years, there has been an effort to bridge the gap between the classical orbital theory and stochastic dynamics. Huybers and Wunsch (2005) proposed that obliquity may be a more important mechanism of glacial dynamics, in a nonlinear way though, and showed that the integrated summer insolation at high latitudes is relevant to the obliquity cycle. Their suggestion was supported recently by high-resolution empirical data (Liu et al. 2007; Suwa and Bender 2008; Drysdale et al. 2009; Naish et al. 2009; Lourens et al. 2010) and as Paillard (2010) highlights: 'the relative weight of 23,000 and 41,000 years periodicities is quite different with such a definition of the astronomical forcing, pleading for a more prominent role of obliquity on climate than usually assumed'. An important addition to the development of modern orbital theory is the mechanism of nonlinear phase locking, describing a mechanism in which obliquity can act as a pace maker for the glacial periods, amplified by the internal system dynamics (Gildor and Tziperman 2000; Ashkenazy 2006; Tziperman et al. 2006). On the other hand, Roe (2006) showed that insolation is in good agreement with the change in ice volume (dV/dt) for the last million years, which led to further investigation of possible combination of obliquity and precession forcing (Huybers and Tziperman 2008; Huybers 2011).

3.2 Sea level measurements and reconstructions spanning different time scales

On this section the sea-level data drawn either from measurements or from reconstruction through proxy data are presented, together with the methods and conclusions of the studies they are drawn from. Additionally, the time series used later for the purposes of creating a combined climacogram, are illustrated here on different plots, for the different time-scale values. In each time-series graph a blue rectangle represents the time length of the previous, smaller time-scale time-series (i.e. process which happens in smaller time period). In plots where two or more time series are plotted together some transformations have been applied to match the data values, which are explained onwards.

Time-series whose resolution followed different values (i.e. did not have a constant time-step) were regularized through linear or nearest-neighbour interpolation, in order to be consistent with the climacogram equations, shown in Chapter 2. The criteria for the chosen step of regularization are the following: (1) the lowest enough percentage of time-steps above the regularized time-step Δ (2) the climacogram (e.g. variance plot) of the time-series keeping the same form and slope values (3) the time-series covering all time scale areas of the combined climacogram plot (see later on)

Finally, two tables present important data values for the used time-series. Table 3.1, contains the information, data and time length, original and regularized resolution, the α climacogram factor (see later), as well as the reference and the source of the data for each of the time-series. Table 3.2, contains the cross-correlation values between the time-series, on different aggregated scales, to test consistency between some of the proxies used, which stem from different studies. The values of Table 3.2 show good consistency between the proxies used, on their overlapping time-scales.

The measurements of global sea-level rise with the highest resolution available are those of the high-quality satellite altimeters (TOPEX/Poseidon (Benada 1997), Jason-1 (Aviso 2003), and OSTM/Jason-2 (CNES 2009)). The three satellite altimeter missions measure sea surface height (SSH) relative to the centre of mass of the Earth along the satellite ground track. While achieving important resolution in its time steps the data is available for a very limited time period. Here we have used the satellite altimetry data of the Global Mean Sea Level (GMSL) variation for the time period of 1993-2017. The Global Isostatic Adjustment is not accounted for, as these alterations are not relevant for the purposes that the time-series is used in this study (i.e. variability and persistence examination).

Church and White (2006 and 2011) reconstructed the global average sea level for the period 1880-2009 and estimated its rise from altimeter data for 1993–2009 and from coastal and island sea-level measurements from 1880 to 2009. According to their reconstruction, for 1993–2009, the estimated rate of rise is 3.2 ± 0.4 mm year^{-1} from the satellite data and 2.8 ± 0.8 mm year^{-1} from the in-situ data. The global average sea-level rise from 1880 to 2009 is about 210 mm. The linear trend from 1900 to 2009 is 1.7 ± 0.2 mm year^{-1} and since 1961 is 1.9 ± 0.4 mm year^{-1}. They also state variability on the rate of rise during the whole twentieth century, but also a statistically significant acceleration since 1880.

Jevrejeva et al. (2006 and 2014), in a similar manner, used 1277 tide gauge records since 1807 to reconstruct the global average sea level rise for the period 1807-2009. According to this reconstruction there is a rate of sea level rise of 3.2 ± 0.4 mm·yr^{-1} for the period 1993-2009, which agrees with the satellite data. This reconstruction, suggests a linear trend of 1.9 ± 0.3 mm·yr^{-1} during the 20th century, with 1.8 ± 0.5 mm·yr^{-1}, since 1970, deviating slightly from that of Church and White (2011). The total acceleration for the reconstructed period (1807-2009) is calculated as 0.02 ± 0.01 mm·yr^{-2}.

Both of these three aforementioned time series are illustrated together in Figure 3.1, where there have been some adjustments to match the plot values for better visualization. Specifically, the reconstructions of Church and White (2011) and Jevrejeva et al. (2014) have been both set to zero on 1990, by superimposing the rest of the values on the Jevrejeva et al time series, while they have also been set to the same average values over 1960-1990 by altering again those of Jevrejeva et al. In a similar manner, the Satellite Altimetry Data has been set to match the value of the Church and White time series on 1993, while the averages of both time series have been set to be the same for the period 1993-2009, by altering the Satellite Altimetry Data values.

Kemp et al. (2011) reconstructed the sea level in North Carolina for the past 2100 years based on salt-mash sedimentary sequences from the US Atlantic coast. Based on the reconstruction, the data on North Carolina, reveal four phases of persistent sea-level change on this time scale. Sea level was stable from at least BC 100 until AD 950. Sea level then increased for 400 y at a rate of 0.6 mm/y, followed by a further period of stable, or slightly falling, sea level that persisted until the late 19th century. Since then, sea level has risen at an average rate of 2.1 mm/y, representing the steepest century-scale increase of the past two millennia. This rate was initiated between AD 1865 and 1892. The authors of the reconstruction have also shown that the North Carolina proxy sea level changes are consistent with global temperature values for at least the past millennium. The time series of Kemp et al. (2011) is illustrated in Figure 3.2.

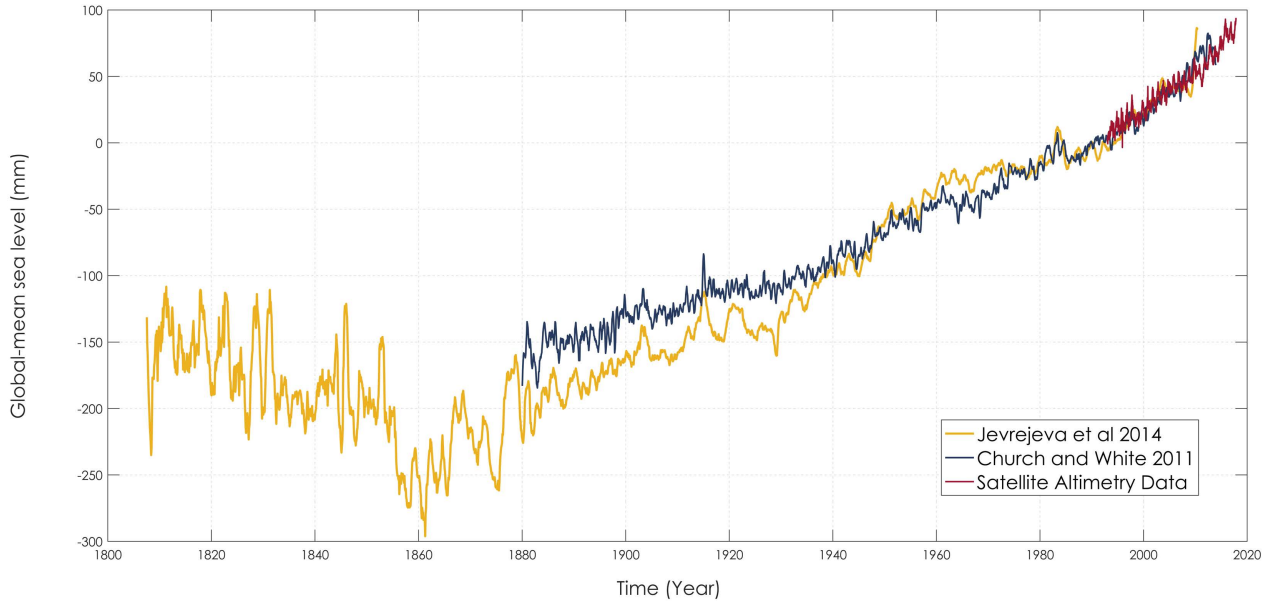

Figure 3.1: Satellite Altimetry Data (Topex/Poseidon, Jason 1 and 2), Church and White (2011) and Jevrejeva et al. (2014) sea level time-series. The values of the y axis represent the global-mean sea-level in millimetres. The x axis counts years until present time.

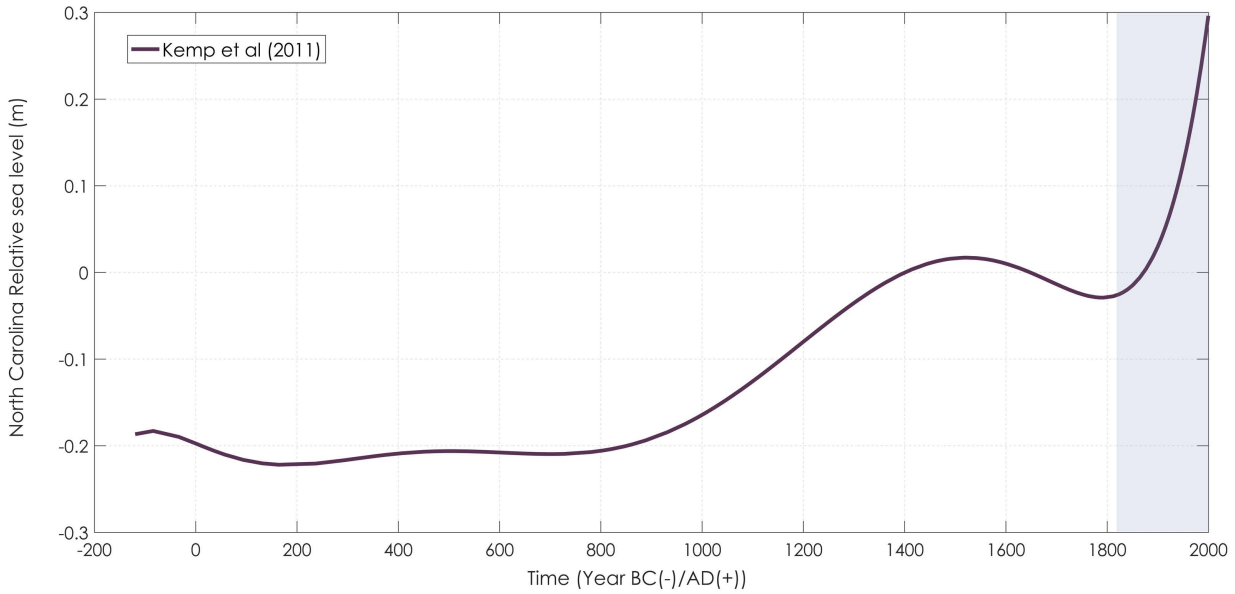

Figure 3.2: Kemp et al. (2011) sea-level time series. The values of the y axis represent the North Carolina Relative sea level in meters. The x axis counts years from the age of -200 B.C. until the age of 2000 A.D. The blue window represents the length of the time series in Figure 3.1.

Grant et al. (2012), reconstructed a continuous and millennial-scale detail record of Red Sea relative sea-level (RSL) for the past 150,000, through ice volumetric changes in core data. The ice volumetric changes were correlated with proxy data of changes in $\delta^{18}O$ values in nearby eastern Mediterranean marine sediments and cave speleothem data from the Soreq Cave. Based on the reconstruction, the rates of sea-level rise reached at least 1.2m per century during all major phases of ice-volume reduction and were typically up to 0.7m per century when sea-level exceeded 0 during the Last Interglacial. Rates of sea-level lowering rarely exceeded 0.8m per century. The time series of Grant et al. (2012) is illustrated in Figure 3.3. It can be seen that the scale difference between this time series and that of Kemp et al. (2011) is high. This is due to low data availability, as the proxies available for timescales between the two aforementioned time series had either very coarse or low-quality data.

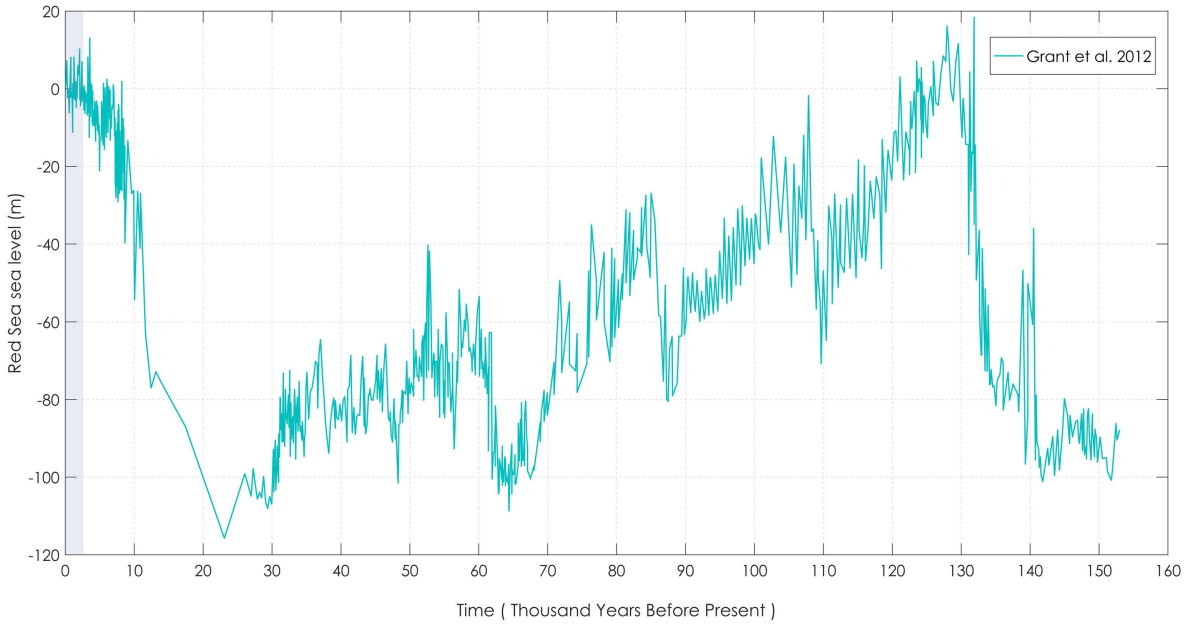

Figure 3.3: Grant et al. (2012) sea-level time series. The values of the y axis represent the Red Sea Relative sea level in meters. The x axis counts thousand years before present. The blue window represents the length of the time series in Figure 3.2.

Siddall et al. (2003) also reconstructed the Red Sea relative sea-level, through oxygen isotope records of the sea's sediment, forming a record of the past 470 thousand years, which approximates to the last glacial cycle. In our study only the record of approximately 380 thousand years was used, as it had the appropriate resolution. The same study reconstructed a higher quality record with a centennial scale resolution from 70kyr to 25kyr before present. It is evident from this record that sea-level changes of up to 35m, at rates of up to 2cm yr^{-1}, coincident with abrupt changes in climate. The maximum rate of change of 0.02 m yr^{-1} Is similar to the mean rate of change during the last deglaciation.

Waelbroeck et al. (2002) reconstructed a global sea-level record of almost 450 thousand years long, through long benthic isotopic records retrieved at one North Atlantic and one Equatorial Pacific site, which were compared with sparse available relative sea-level data. In Figure 3.4 both the time series of Waelbroeck et al. that of Siddall et al are illustrated. It is shown the global sea-level record of the first study agrees with the Red Sea level record of the latter.

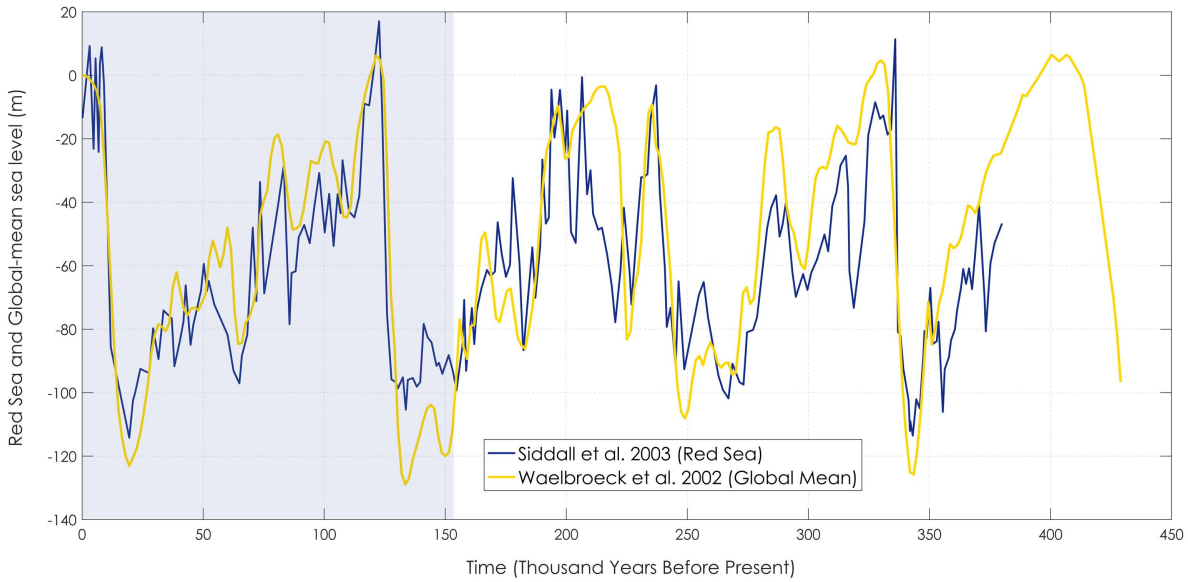

Figure 3.4: Siddall et al. (2003) and Waelbroeck et al. (2002) sea-level time series. The values of the y axis represent the Red Sea and the Global-mean sea-level respectively, in meters. The x axis counts thousand years before present. The blue window represents the length of the time series in Figure 3.3.

Spratt et al. (2016) reconstructed a late Pleistocene global sea-level record spanning 800 thousand years before present, from ocean sediment core data using a wide variety of proxies and models. The orbital forcing signal is evident through a spectral analysis of this record but also through the spectral analysis of the proxy data that was used for its creation. Sea-level estimates for each interglacial vary greatly between them, producing standard deviations of 11–26 m. The time series is illustrated in Figure 3.5.

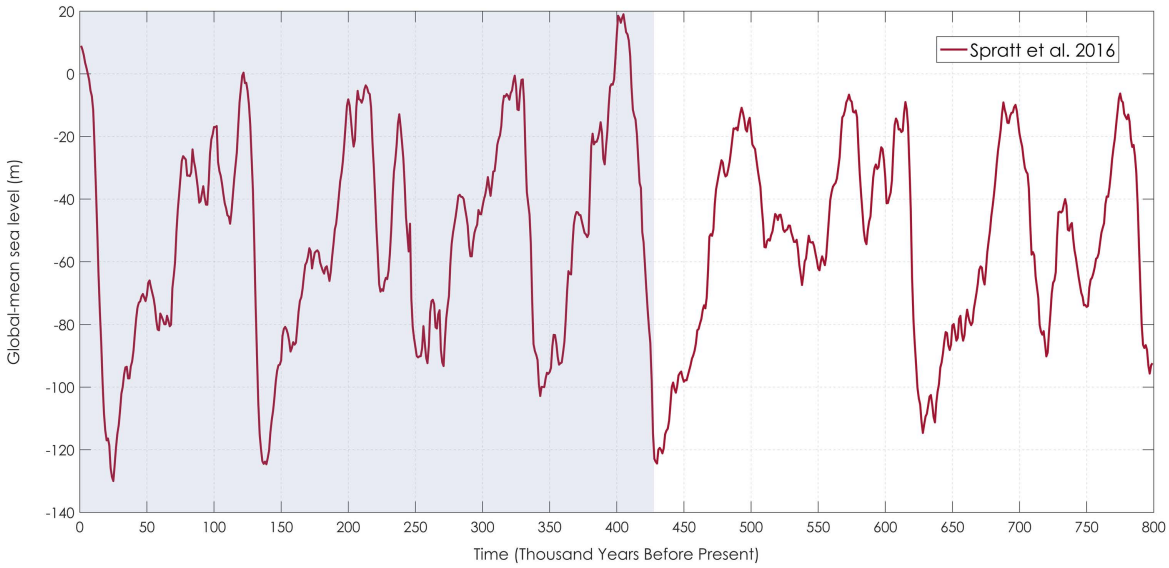

Figure 3.5: Spratt et al. (2016) sea-level time-series. The values of the y axis represent the Global-mean sea-level in meters. The x axis counts thousand years before present. The blue window represents the length of the time series in Figure 3.4.

De Boer et al. (2013) constructed an almost 5.5 million year-long global sea-level reconstruction using a fully coupled system of four 3-D ice-sheet models is used, simulating glaciations on Eurasia, North America, Greenland and Antarctica. The ice-sheet models use a combination of the shallow ice and shelf approximations to determine sheet, shelf and sliding velocities. The framework used consists of an inverse forward modelling approach to derive a self-consistent record of temperature and ice volume from deep-sea benthic $\delta^{18}O$ data over the past 1 million years, a proxy for ice volume and temperature. It is shown, that for both eustatic sea level and sea water $\delta^{18}O$ changes, the Eurasian and North American ice sheets are responsible for the largest part of the variability. De Boer et al. (2014) through the simulation of these proxies showed persistent 400,000-year eccentricity cycles of Antarctica dominating through the past 35 million years, which was eventually supressed by the smaller 100,000-year cycle found also in the higher resolution proxies we refer to in this study.

Miller et al. (2005 and 2011) reconstructed a coarse 180-million-year global sea-level record with a resolution of 0.1 million years and a higher-resolution record of a step of thousand years and a length of 9 million years, by studying coral reef records, the $\delta_{18}O$ proxy of ice volume, and continental margin sequences. Many of proxies used for the reconstruction were acquired through an Ocean Drilling Program (ODP). The effect of the 41,000-year tilt-cycle is evident through the spectral analysis of the record and played a special role especially during the Pliocene to Brunhes (i.e., from 5.2–0.8 million years before present) when it dominated between the Milankovitch-scale sea level cycles. The evidence of the small precessional cycle is also apparent, but not yet explained. The larger ~100,000-year eccentricity cycle is dominating during the last Brunhes (780 thousand years before present). A large million year-

scale cycle is apparent during the Oligocene to middle Miocene, where large (50-60 m) sea level falls occurred. This cycle is approximated by the authors at a periodicity of 1.2 million years and may be paced by the long planetary tilt cycle.

Kominz et al (2008) reconstructed a sea-level record for the past 108 million years through backstripping of corehole data from the New Jersey and Delaware Coastal Plains. This study points out the importance of million-year scale sea-level cycles and suggests that may be eustatic in origin. The reconstructed time-series suggests that sea level ranged from about 75-110 m in the Late Cretaceous, reached a maximum of about150 m in the Early Eocene and fell to zero in the Miocene.

The 10 million-year scale time-series of De Boer et al. (2013) and Miller et al. (2011) are illustrated in Figure 3.6, while the 100 million-year scale time-series of Miller et al. (2005) and Kominz et al. (2008) are illustrated in Figure 3.7. The time series where plotted together with their values unchanged, while they follow different mean values or fluctuations on certain time periods.

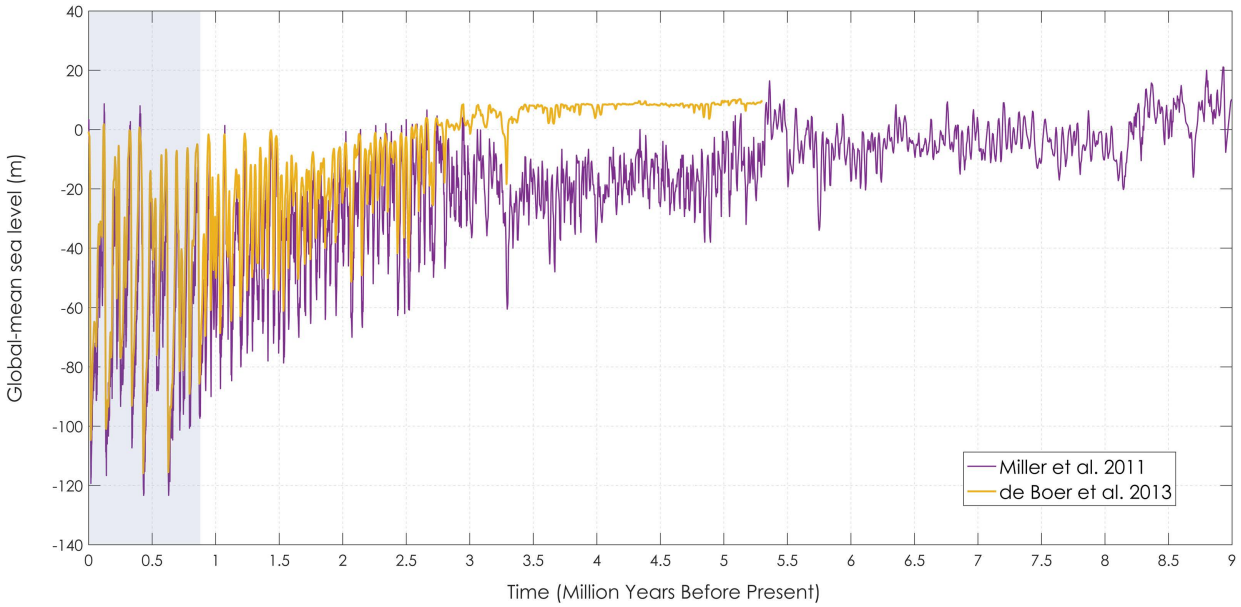

Figure 3.6: De Boer et al. (2013) and Miller et al. (2011) sea-level time series. The values of the y axis represent the Global-mean sea-level in meters. The x axis counts million years before present. The blue window represents the length of the time series in Figure 3.5.

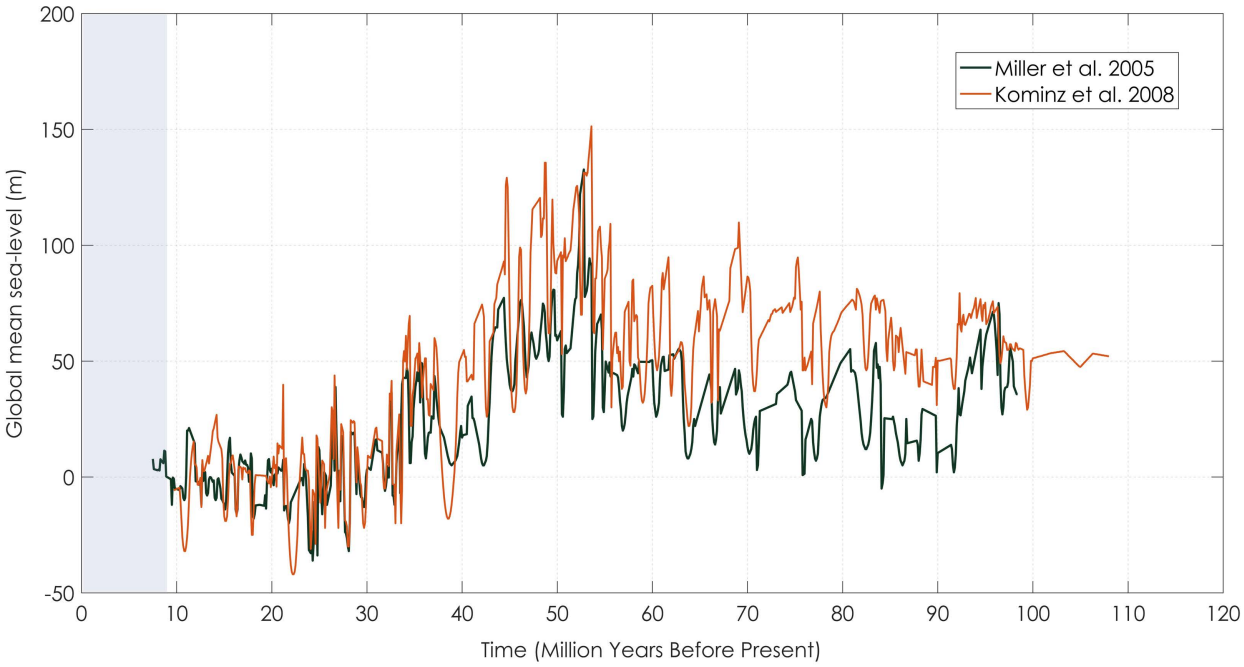

Figure 3.7: Kominz et al. (2008) and Miller et al. (2005) sea-level time series. The values of the y axis represent the Global-mean sea-level in meters. The x axis counts million years before present. The blue window represents the length of the time series in Figure 3.6.

Table 3.1: Characteristic Values of the Sea-Level Time Series

Abbreviation	Number of data *n*	Original resolution range (years)	Regularized resolution Δ (years) *	Total length L (years)	Climacogram Factor α	Reference	Data availability from
Satellite Data	915	21/773	21/773	24.86	0.046	TOPEX/Poseidon (Benada 1997), Jason-1 (Aviso 2003), OSTM/Jason-2 (CNES 2009)	https://www.nodc.noaa.gov/SatelliteData/jason/
Church and White	1608	1/12	1/12	134	0.0157	Church and White (2011)	http://www.cmar.csiro.au/sealevel/sl_data_cmar.html
Jevrejeva	2436	1/12	112	203	0.0118	Jevrejeva et al. (2014)	http://www.psmsl.org/products/reconstructions/jevrejevaetal2014.php
Kemp	211	0.1-73.1	10 (49%)	2,110	9.5	Kemp et al. (2011)	https://www1.ncdc.noaa.gov/pub/data/paleo/paleocean/relative_sea_level/kemp2011rsl.txt
Grant	503	100-5,635	250 (28%)	125,750	0.0345	Grant et al. (2012)	https://www1.ncdc.noaa.gov/pub/data/paleo/contributions_by_author/grant2012/grant2012rsl.txt
Siddall	125	147-7,660	300 (6.57%)	375,000	0.033	Siddall et al. (2003)	https://www1.ncdc.noaa.gov/pub/data/paleo/contributions_by_author/siddall2003/siddall2003.txt
Waelbroeck	287	1500	1500	430,500	0.0268	Waelbroeck et al. (2002)	https://www1.ncdc.noaa.gov/pub/data/paleo/contributions_by_author/waelbroeck2002/waelbroeck2002.txt
Spratt	799	1000	1000	799,000	0.03	Spratt et al. (2016)	https://www1.ncdc.noaa.gov/pub/data/paleo/contributions_by_author/spratt2016/spratt2016.txt
Deboer	53001	100	100	5,300,100	0.0382	De Boer et al. (2013)	https://www1.ncdc.noaa.gov/pub/data/paleo/reconstructions/deboer2014/deboer2014.txt
Miller (short)	1801	1,000-5,000	5,000 (0%)	9,005,000	0.041	Miller et al. (2011)	https://www1.ncdc.noaa.gov/pub/data/paleo/contributions_by_author/miller2005/miller2011.txt
Miller (long)	910	100,000	100,000	91,000,000	0.0315	Miller et al. (2005)	https://www1.ncdc.noaa.gov/pub/data/paleo/contributions_by_author/miller2005/miller2005-backstrip.txt
Kominz	984	100,000	100,000	98,400,000	0.023	Kominz et al. (2008)	https://www1.ncdc.noaa.gov/pub/data/paleo/contributions_by_author/miller2005/miller2005-kominz08.txt

** the values in parenthesis represent the percentage of the data with a time step higher than the chosen regularized time steps.*

Table 3.2: Cross-Correlation factor (lag 0) between different time-series

Cross - Correlations							
Scale	Jevrejeva – Kemp	Scale	Grant - Spratt	Scale	Siddall - Spratt	Scale	Waelbroeck - Spratt
5	0.93	1000	0.82	2000	0.76	3000	0.91
10	0.94	2000	0.83	4000	0.79	6000	0.93
15	0.95	3000	0.83	6000	0.84	9000	0.94
		4000	0.84	8000	0.87	12000	0.95
		5000	0.85	10000	0.85	15000	0.96
		6000	0.85	12000	0.90	18000	0.97
				14000	0.92		
				16000	0.95		
				18000	0.93		

3.3 The combined climacogram: seeking persistence and deterministic cycles in the sea-level record

3.3.1 The empirical climacogram

To construct the empirical part combined climacogram, i.e. the log-log plot of the standard deviation of the historical time series versus the time scale values, we follow the methodology proposed in Chapter 2, section 2.6.2. The aggregated standard deviation values $\sigma_x^{(k)}$ for different scales of each time series is calculated from the available resolution Δ up to the scale values of k=L/10 (Koutsoyiannis 2002). The standard deviation values $\sigma_x^{(k)}$, for each time-series x(t) are multiplied by a climacogram scaling factor, a_x so that the values of $\sigma_y^{(k)} = a_x \sigma_x^{(k)}$ are visualized combinedly beginning from the value 1 (see more in section 2.6.2). The values of the factors a_x for each of the time series are presented in Table 3.1. The log/log plots of the empirical climacogram each time series are shown in the combined climacogram plot of Figure 3.8, with circle dot-plots of different colours.

The combined empirical climacogram of Figure 3.8 gives us an impressive view of overall sea level variability spanning eight orders of magnitude – from 1 month to 10 million years. We derive from the empirical climacogram some basic conclusions:

1. It is observed that, for this huge variation of the scale k, the (combined) standard deviation $\sigma_y^{(k)}$ of all series, which depicts the standard deviation of the sea-level variable, ranges in a very small interval, varying less than an order of magnitude (between 0.1 and 1). The red horizontal dashed line in Figure 3.8, which is drawn from the rightmost bottom point of the empirical climacogram, shows that the variability at the scale of 10 million years is about 65% percent of the variability at the monthly scale. The essence of this value can be shown by comparing this process with a process without any persistence e.g. a pure random white noise process with Hurst coefficient, H = 0.5. The theoretical climacogram of a white noise process

is visualized in Figure 3.8 through a blue dashed line. It seems that if the fluctuation of the sea level rise was consistent with classical statistics and followed no persistence pattern the reduction in variability to 65% percent (from 100% in the monthly scale) would appear at the scale of only 3 months (!), calculated from the point of intersection of the blue dashed line of the white noise process with the red horizontal dashed line. This huge difference of 3 months against 10 million years (!) suggests enhanced change particularly at the large time scales. The fact that the variability at large time scales remains at such a high percentage of the variability at low time scales, also suggests that there is enhanced unpredictability – or else uncertainty, aside from the predictable deterministic cycles affecting the sea-level process. This concludes to the description of the existence of a long-term persistent behaviour (or Hurst-Kolmogorov behaviour) of the sea-level process, on a scale span from months to ten million years.

2. Between the scale magnitudes of 10^3 to 10^5 years, a sudden drop of slope, and a steeper general slope is observed for the time-series which depict process on this magnitude, namely the Grant, Siddall, Waelbroeck and Spratt time-series. The magnitude of scale values where the drop of slope of the climacogram occurs, coincides with the scale magnitude of the Milankovitch cycles, as described in section 3.1.2. To show that this drop of model is due to the deterministic harmonic oscillation caused by the Milankovitch cycles – as is also evident from the spectral analysis of the aforementioned time series, described above – we construct and describe later on, a stochastic FGN model, incorporating harmonic deterministic oscillations (see section 3.3.3).

This drop of slope values is also followed by the de Boer and Miller (short) time-series on the scale magnitudes of 10^3 to 10^5 years. The higher length of these time series allows us to better understand the effect of the Milankovitch forcing, as after the scale values of 10^5 the climacogram of the time-series becomes again flat, thus showing the continuation of the long-term persistent behaviour after those scales.

Another, -milder- drop is observed for the time-series occurring on time scales of magnitude 10^6 to 10^7 years. This is also attributed to a deterministic forcing of cycles with eustatic origin as described in Miller et al. (2011), which occur on million-year time-scale values. The effect of these cycles can be studied more coherently if sea-level reconstruction data of higher time-scale values are available.

3. Certain time-series, especially that of Jevrejeva, but also those of Topex/Poseidon satellite altimetry observations, Church and White and Miller (short) reconstructions, show a flat part and/or a rise of slope on the tail of the climacogram. Positive slope values of the climacogram are inconsistent with the stochastic theory presented in Chapter 2, as they imply a negative Hurst coefficient. The reason this inconsistency appears is because of data uncertainties (both in sampling and ageing) combined with the bias in sample estimation (Koutsoyiannis 2003a, 2011b)[4]. The aforementioned studies show a method of bias estimation and extraction from the climacogram values, which was not applied hereby.

[4] Koutsoyiannis D (2003a) Climate change, the Hurst phenomenon, and hydrological statistics. Hydrol Sci J 48(1):3–24
Koutsoyiannis D (2011b) Hurst-Kolmogorov dynamics and uncertainty. J Am Water Resour Assoc 47(3):481–495

The reason for the flat or rising tail is related to the fact that the entire length of the aforementioned time series is located on a branch of the process with a monotonic trend (see the plotted windows of the respective time series e.g. Jevrejeva or Church and White). When a longer time series is viewed, which shows that the monotonic trend is in fact part of a longer fluctuation, the problem of the climacogram tail is indeed remedied. For this reason, we choose to ignore the bias in the climacogram estimation.

4. For the scale magnitudes of 10 to 100 years, there was an important unavailability of data, as the only study available was that of Kemp et al. (2011). The climacogram on this scale values is fluctuating, as the resolution of the provided time-series is not adequate enough. The consistency of the climacogram on these values with the rest of the combined climacogram arises from consistency between slope of the time series for the scales before (Church and White and Jevrejeva time-series) and after (Grant time-series) these values.

3.3.2 The theoretical climacogram

A theoretical climacogram is adapted to the empirical climacogram values by combining a simple Hurst-Kolmogorov (HK) model with a harmonic model integrating different oscillation periods, and modelling it to adapt to the form of the empirical climacogram:

1. For the Hurst-Kolmogorov (HK) model we use a simple and parsimonious edition of the model as described in Chapter 2, section 2.5.1, Table 2.1:

$$\gamma(\Delta) = \lambda(\alpha/\Delta)^{2-2H} \tag{3.1}$$

where $\gamma(\Delta)$ is the variance at scale Δ, H is the theoretical value of the Hurst coefficient for the HK model and α and λ are scaling factors.

Thus, the values of the standard deviation $\sigma_{HK}^{(k)}$ of the HK model are given by the simple power-law relationship:

$$\sigma_{HK}^{(k)} = k^{H-1}\sigma \tag{3.2}$$

where σ is the combined scaling factor (which incorporates previously used factors α and λ) that is equal to the first value of the theoretical climacogram:

$$\sigma \equiv \sigma_{HK}^{(1)} = 1/12 \tag{3.3}$$

The value of the Hurst coefficient is chosen through consecutive trials to follow the slope of the log/log empirical climacogram plot, mainly on its beginning (scales 1/12 - 10^3) and its tail (scales 10^6 - 10^7). A value of $H = 0.995$ is chosen to reflect a maximization of uncertainty on small and high scales, thus allowing to create an HK model with maximum long-term persistence.

2. For the harmonic model we incorporate three Milankovitch cycles, namely the precession cycle with an approximate period of T_1 = 21,000 years, the obliquity/axial tilt cycle with an approximate period of T_2 = 41,000 years and the eccentricity cycle with an approximate period of T_3 = 100,000 years (Milankovitch 1941, Bolshakov 2008, Paillard 2010). A million-year scale cycle, of eustatic origin is also incorporated in the model to account for the drop in the empirical climacogram at time-scales of 10^6 to 10^7 years, with an approximate period of T_4 = 1,200,000 years (Miller et al. 2011).

In section 2.5.3 the climacogram of a harmonic process is presented. Accounting to the presented methodology, the four harmonic processes are incorporated into the theoretical climacogram following equation (2.37), which formulates the climacogram of a harmonic process:

$$\sigma_{T_i}^{(k)} = \left[\frac{T_i}{(\pi k)}\right]\left|\sin\left(\frac{\pi k}{T_i}\right)\right| \tag{3.4}$$

where $\sigma_{T_i}^{(k)}$ is the aggregated standard deviation of the harmonic process, with time period T_i, for i=1,2,3,4.

3. The complete theoretical model consists of the sum of the climacogram values of the HK model and the four harmonic models, each multiplied by a model weight coefficient ω_i, as follows:

$$\sigma_{th}^{(k)} = \omega_1\sigma_{T_1}^{(k)} + \omega_2\sigma_{T_2}^{(k)} + \omega_3\,\sigma_{T_3}^{(k)} + \omega_4\,\sigma_{T_4}^{(k)} + \omega_5\sigma_{th}^{(k)} \tag{3.5}$$

The values of the ω_i coefficients are chosen so that the plot of the climacogram of the theoretical model agrees with the one of the combined empirical climacogram. The theoretical model values, as well as the values of the ω_i coefficients are presented in Table 3.3. The theoretical model spanning from scales of 1 month to 10^7 years is plotted with a thick continuous red line in Figure 3.8. The red line plot fits perfectly the fluctuations of the empirical climacogram, except for those sections analysed before, which will be furtherly examined in the following section.

Table 3.3: Values of parameters and coefficients for the HK and the four Harmonic models

Model	Value	Coefficient	Value
Harmonic T_1	T_1 = 21,000	ω_1	0.02
Harmonic T_2	T_2 = 41,000	ω_2	0.05
Harmonic T_3	T_3 = 100,000	ω_3	0.10
Harmonic T_4	T_4 = 1,200,000	ω_4	0.05
Hurst-Kolmogorov	**H = 0.995**	ω_5	0.78

Figure 3.8: The combined empirical climacogram and the theoretical climacogram all in one plot. The dotted plots represent the empirical climacogram plots of the various time-series shown with different colours on the legend. The thick continuous red line represents the theoretical climacogram which consists of a combination of an HK model with H=0.995 and four harmonic models with T= 21,000, 41,000, 100,000 and 1,200,000 years respectively. The blue dashed line represents a white noise model with H=0.5. The purple dashed line shows the lowest standard deviation value of the combined empirical climacogram, which is approximately $\sigma_y^{(10\text{^}7)}=0.65$.

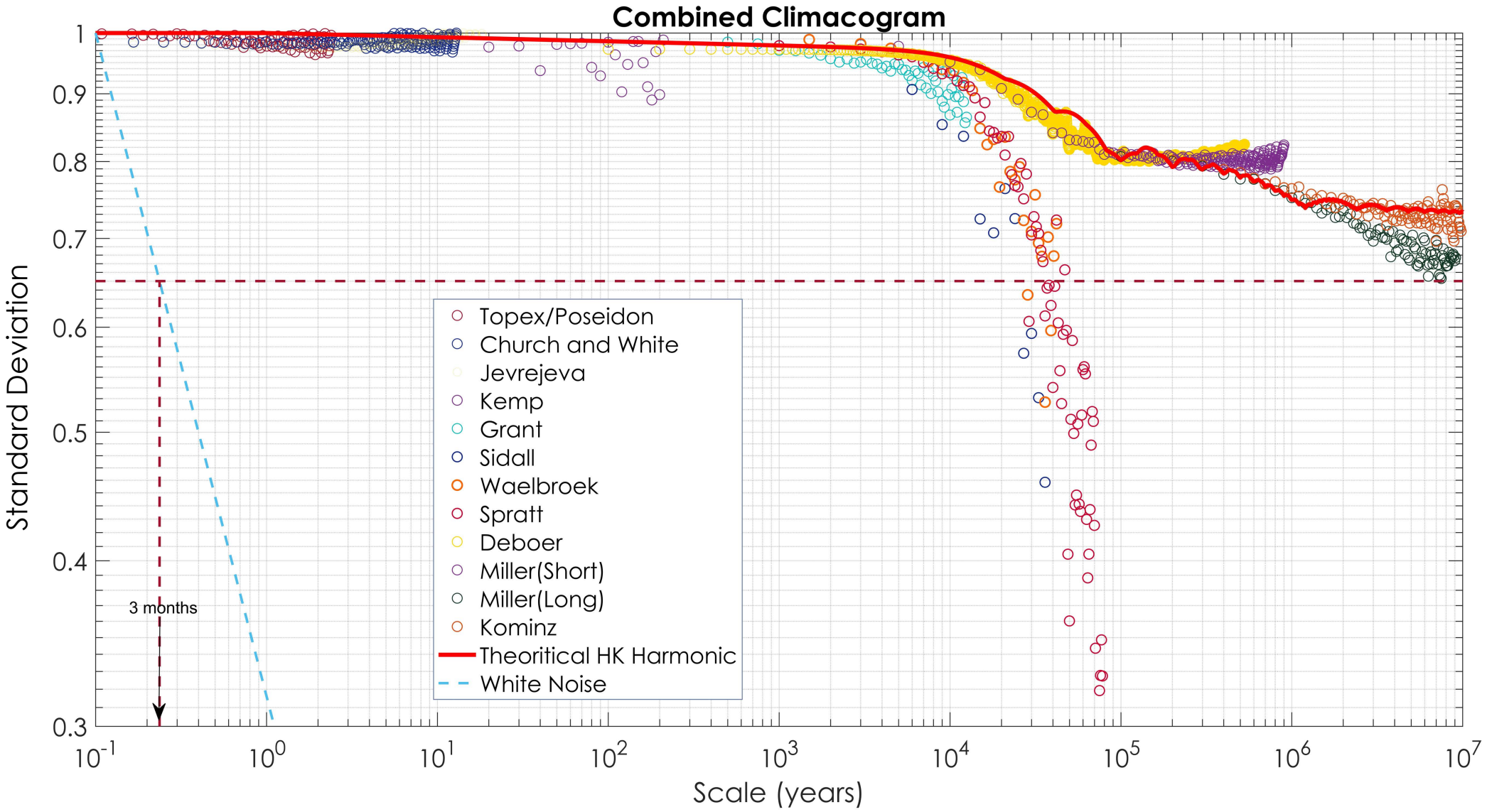

3.3.3 Effect of the deterministic forcing on the climacogram – construction of an FGN model

As discussed in section 3.3.1 the drop of slope and the overall steeper slopes observed on the combined climacogram of Figure 3.8 between the scale magnitudes of 10^3 to 10^5 years. It is also discussed that this drop is attributed to deterministic forcing, especially the one arriving from the effect of Milankovitch cycles, as they occur on time periods of approximately 21,000, 41,000 and 100,000 years. The effect of the Milankovitch cycles is not only seen on the time series that show a steep and important drop of slope (those of Grant, Siddall, Waelbroeck and Spratt), but also on those of Deboer and Miller (Short), which while having a head and a tail of constant slope, they follow a drop between 10^4 and 10^5 years. The theoretical climacogram discussed on section 3.3.2, incorporating harmonic deterministic functions together with and HK model, accounts for this forcing and follows the slope of the empirical climacogram of Deboer and Miller (Short).

To evaluate completely the adaptability of the theoretical climacogram to the empirical data, but also to evaluate the effect of deterministic forcing of Milankovitch cycles, on the sea-level variable, the construction of a stochastic reproduction of the sea-level time process, on the scale magnitudes of concern is followed here. To account for and to preserve the main elements of concern on variability and the climacogram which are the short-term correlation (represented through the autocorrelation factor) as well as the long-term correlation (represented through the Hurst coefficient) an FGN model is constructed. The FGN model, as discussed on section 2.5.2 has the ability not only to preserve the autocorrelation of small lags, but also to preserve the long-term correlation of the time series, e.g. the long-term persistence through the Hurst coefficient. The combination of an FGN model which adapts to the Hurst values of the theoretical HK model constructed on section 3.2.3, with a harmonic model as the one used in the theoretical model, creates a combined FGN/Harmonic model, the characteristic values of which are based on the theoretical model. This allows for a random generation of synthetic time-series on the modeled scale values and plotting of their climacograms. To show adaptability with the empirical climacograms, the climacogram of a synthetic time series generated through the combined FGN/Harmonic model, with length equal to a time series occurring on scale magnitudes of 10^4 to 10^5 years, should follow the drop of slope of the empirical climacogram on scale magnitudes of 10^4 to 10^5 years.

For the construction of the FGN model we follow the methodology presented on section 2.5.2. The general equations of the model follow equations (2.31) and (2.32), combining three AR(1) autoregressive models. The FGN model preserves the mean value and the standard deviation of the modeled time-series, as well as the first-lag autocorrelation factor (ρ_1), and the Hurst coefficient of the theoretical model. The factors which are needed to construct the autocorrelation structure of the FGN model are calculated through equations (2.33) – (2.36). The constructed FGN model is then combined with the harmonic model through the same methodology that was followed to create the theoretical model in section (3.3.2) but also through preserving the same values of the model coefficient factors ω_i.

The climacogram of the combined FGN/Harmonic model is calculated as follows.

$$\sigma^{(k)}_{FGN/Harmonic} = \omega_1 \sigma^{(k)}_{T_1} + \omega_2 \sigma^{(k)}_{T_2} + \omega_3 \, \sigma^{(k)}_{T_3} + \omega_4 \, \sigma^{(k)}_{T_4} + \omega_5 \sigma^{(k)}_{FGN} \qquad (3.5)$$

where the factors ω_i and the rest of the model values (periods T_i, Hurst Coefficient H), are equal to the ones referenced in Table 3.3.

After the set-up we utilize the FGN/Harmonic model, by considering as model time-series one following the statistical characteristics, the resolution (time-step) and length of data of the reconstruction of Spratt et al. (2016), which falls on the time-scales of interest. Thus, by generating a synthetic-time series through the FGN/Harmonic model with time-step of 1000 years, and length n = 1000, and plotting its climacogram, its values would fall on the same scale level as the Spratt time series on the climacogram e.g. on scale magnitudes of 10^4 to 10^5 years.

This is visualized in Figure 3.9, where the climacogram of a synthetic time-series generated by the FGN/Harmonic model, plotted with red dots, not only falls on the scale magnitudes discussed above but also preserves the exact slope that the empirical climacogram data follow, not only that of the Spratt time series, but from all the rest of the time series occurring on these scales starting from the Grant time series (10^3 scale) up to Spratt (10^5 scale).

This agreement between the FGN/Harmonic model, which is based on the characteristics of the theoretical model in section 3.3.2, and the empirical data, shows the agreement between the general theoretical model (red line on the climacogram plot) and the empirical data, as on the theoretical model agrees with the drop of slope, when considering a time series of equal length as to those occurring on the time scale range where the slope is dropping. Also, the agreement shows the drastic deterministic forcing of the Milankovitch cycles on the time-scale range where they occur, as the climacogram drops to a slope close to 0.5 which would signify close-to-zero uncertainty. At the same time, the differentiation of the slope before and after this time-scale values, shows that uncertainty works vice-versa for the time scales where the deterministic forcing does not occur, preserving great persistent behaviour (thus uncertainty). Altogether, the good adaptation of the theoretical model to the empirical data, describes a general long-term persistent behaviour of the sea-level variable on a multiple time scales, as also discussed above.

Figure 3.9: The combined climacogram is ploted both for the empirical part (coloured dots) and the theoretical model (red line), for scale values between 103 and 106 years. Additionally, the climacogram of a random realization of the FGN/Harmonic model is plotted with red filed dots

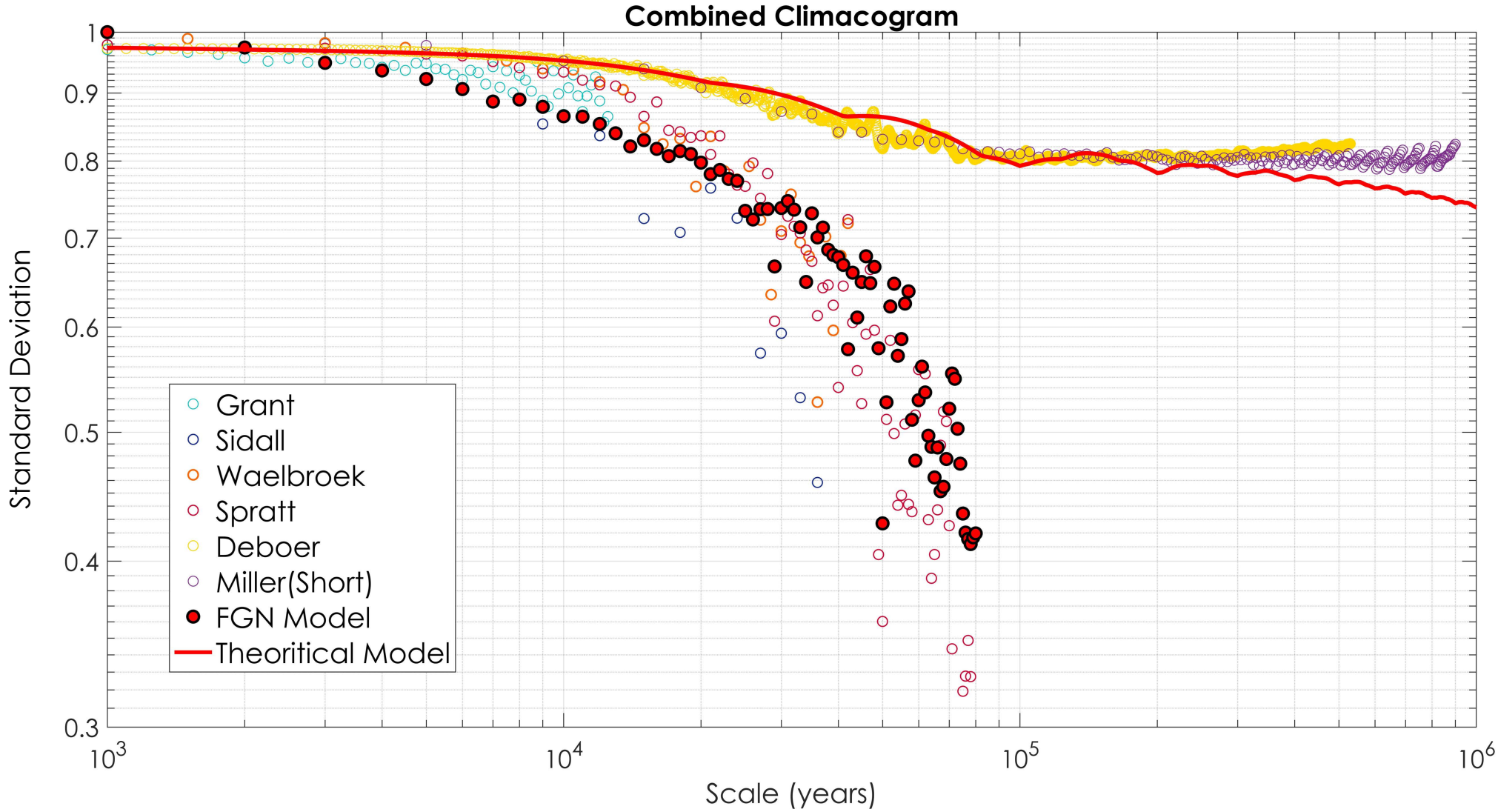

Chapter 4: Variability and Persistence in Sea Surface Temperature and the El Niño Southern Oscillation

In this part of the study, various measurements and reconstructions of the recent evolution of the Sea Surface Temperature (SST) variable, are analyzed through stochastic tools. The El Niño Southern Oscillation (ENSO) in the equatorial Pacific, which affects the SST and the whole climatic stability of the planet is also analyzed here.

4.1 The ENSO phenomenon and SST variability

We describe the basic definition and physical explanation of the ENSO phenomenon with a description taken from the National Oceanic and Atmospheric Administration (NOAA) of the United States Department of commerce[5]:

> *The El Niño-Southern Oscillation (ENSO) is a periodic fluctuation in sea surface temperature (El Niño) and the air pressure of the overlying atmosphere (Southern Oscillation) across the equatorial Pacific Ocean. The term El "Niño" (the boy in Spanish) stems from early Christian inhabitants of western equatorial South America, who equated the warm water current at the finish of the year, when the ENSO oscillation caused a peak of water warming and the resulting impacts in local fishing and other activities, with their holiday celebrating the birth of Jesus.*
>
> *The Southern Oscillation describes a bimodal variation in sea level barometric pressure between observation stations at Darwin, Australia and Tahiti. It is quantified in the Southern Oscillation Index (SOI), which is a standardized difference between the two barometric pressures. Normally, lower pressure over Darwin and higher pressure over Tahiti encourages a circulation of air from east to west, drawing warm surface water westward and bringing precipitation to Australia and the western Pacific. When the pressure difference weakens, which is strongly coincidental with El Niño conditions, parts of the western Pacific, such as Australia experience severe drought, while across the ocean, heavy precipitation can bring flooding to the west coast of equatorial South America.*
>
> *The SOI is one measure of the large-scale fluctuations in air pressure occurring between the western and eastern tropical Pacific (i.e., the state of the Southern Oscillation) during El Niño and La Niña episodes. In general, smoothed time series of the SOI correspond very well with changes in ocean temperatures across the eastern tropical Pacific. The negative phase of the SOI represents below-normal air*

[5] https://www.ncdc.noaa.gov/teleconnections/enso/enso-tech.php

pressure at Tahiti and above-normal air pressure at Darwin. Prolonged periods of negative (positive) SOI values coincide with abnormally warm (cold) ocean waters across the eastern tropical Pacific typical of El Niño (La Niña) episodes. The evolution of the SOI index values through the years 1951-2018 is depicted in Figure 4.2.

Although the exact initiating causes of an ENSO warm or cool event are not fully understood, the two components of ENSO – sea surface temperature and atmospheric pressure are strongly related. During an El Niño event, the easterly trade winds converging across the equatorial Pacific weaken. This in turn slows the ocean current that draws surface water away from the western coast of South America and reduces the upwelling of cold, nutrient–rich water from the deeper ocean, flattening out the thermocline and allowing warm surface water to build in the eastern part of the basin.

The strengthening and weakening of the trade winds is a function of changes in the pressure gradient of the atmosphere over the tropical Pacific. Ironically, the warming of the sea surface works to decrease the atmospheric pressure above it by transferring more heat to the atmosphere and making it more buoyant. So, in summary, the pressure gradient affects the sea surface temperatures, and the sea surface temperatures affect the pressure gradient. These mechanics are illustrated in Figure 4.1 (a).

The connection between the Southern Oscillation and precipitation is also manifest in the quantity of long–wave (e.g., infrared) radiation leaving the atmosphere. Under clear skies, a great deal of the long–wave radiation released into the atmosphere from the surface can escape into space. Under cloudy skies, some of this radiation is prevented from escaping. Satellites are able to measure the amount of long–wave radiation reaching space, and from these observations, the relative amount of convection in different parts of the basin can be estimated.

Monitoring of ENSO conditions primarily focuses on sea surface temperature (SST) anomalies in 4 geographic regions of the equatorial Pacific (see image to the right). SST anomalies equal to or greater than 0.5°C (0.9°F) in the Niño 3.4 region (comprising portions of Niño regions 3 and 4, from 170°W to 120°W longitude) are indicative of ENSO warm phase (El Niño) conditions, while anomalies less than or equal to –0.5°C (–0.9°F) are associated with cool phase (La Niña) conditions. Niño 3.4 SST anomalies are averaged over the three months ending with the current month, and that value is called the Oceanic Niño Index (ONI). If the ONI exhibits warm or cool phase conditions for at least five consecutive values, it officially becomes an El Niño or La Niña event. The geographic regions of ENSO are shown in Figure 4.1 (c). Figure 4.3 depicts the SST variability in the Nino 4.3 area through the years 2000-2018.

In addition, the thermal expansion of the warming water in the eastern part of the basin measurably raises sea level in these regions, and this change in sea level can be measured by satellite sensors. Therefore, variations in sea level are good indicators of the presence of an El Niño. During an El Niño, sea level in the eastern Pacific is well above average, while during a La Niña, the increased flow of cold

deep water to the surface acts to lower the sea level. Sea level fluctuations in the El Niño and La Niña phases are pictured in Figure 4.1 (b).

a.

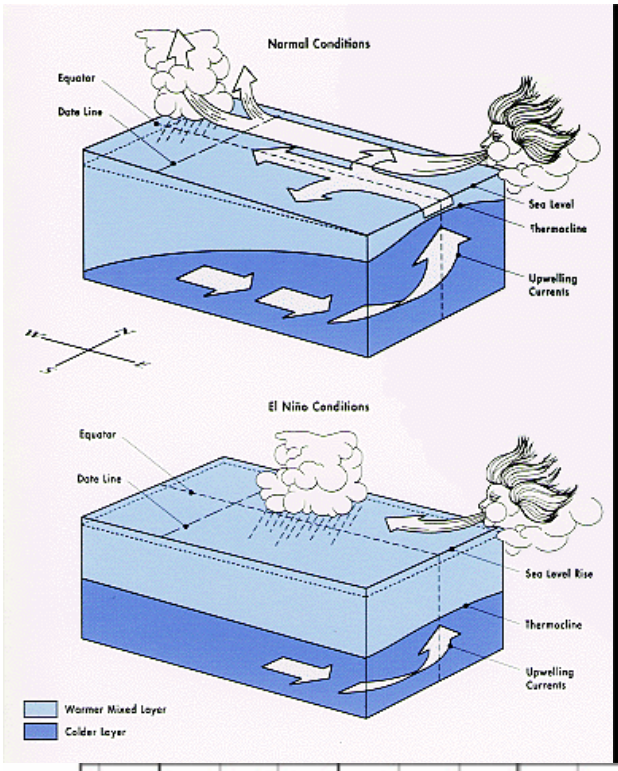

b.

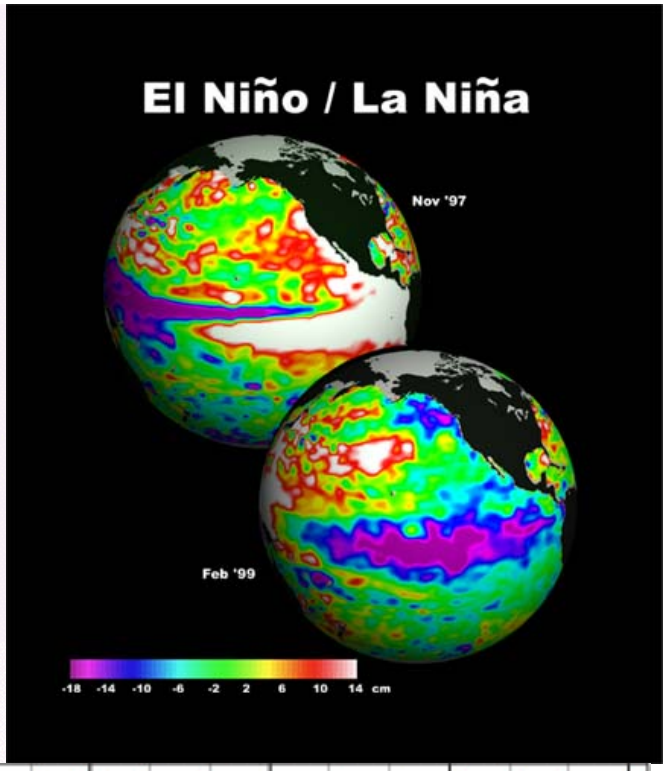

c.

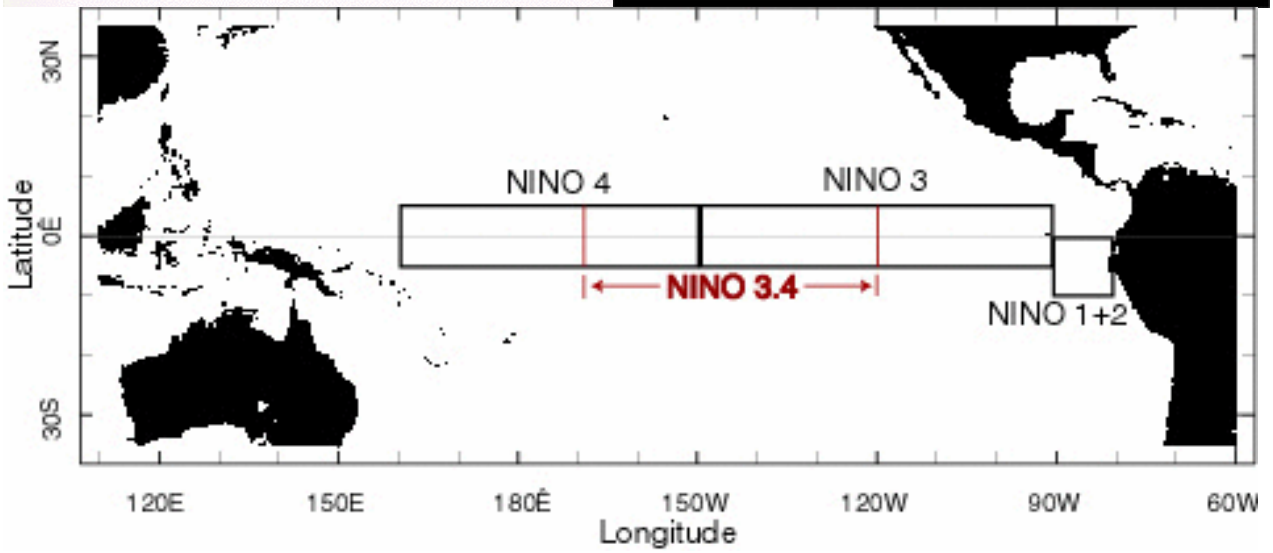

Figure 4.1: a. Driving physical mechanisms in Neutral and El Niño conditions b. Sea level anomalies in El Niño and La Niña events c. Geographic regions of ENSO. Source: NOAA

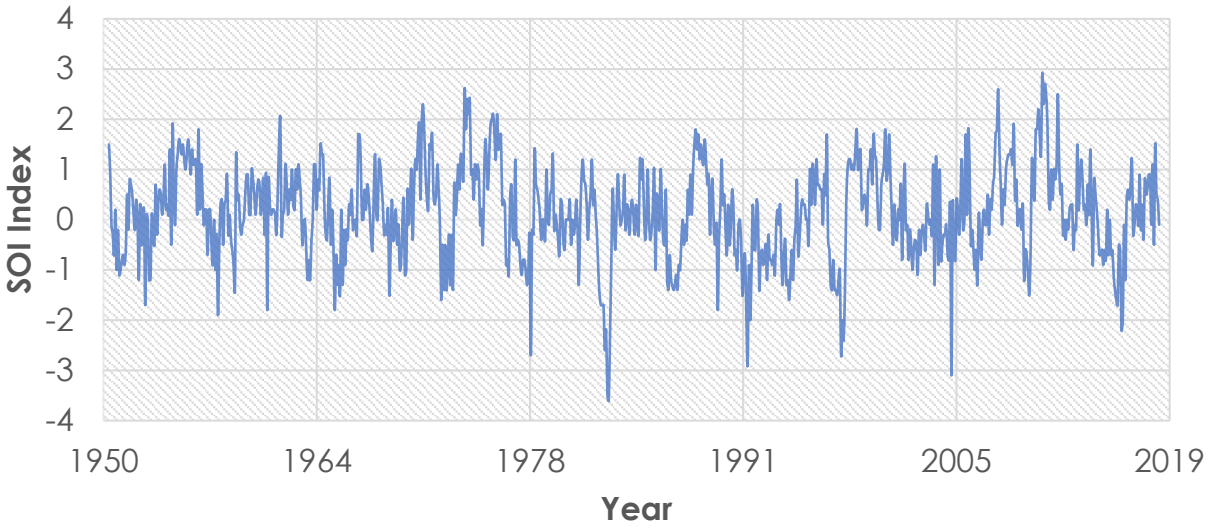

Figure 4.2: Evolution of the SOI index through the years 1951-2018. Source: NOAA

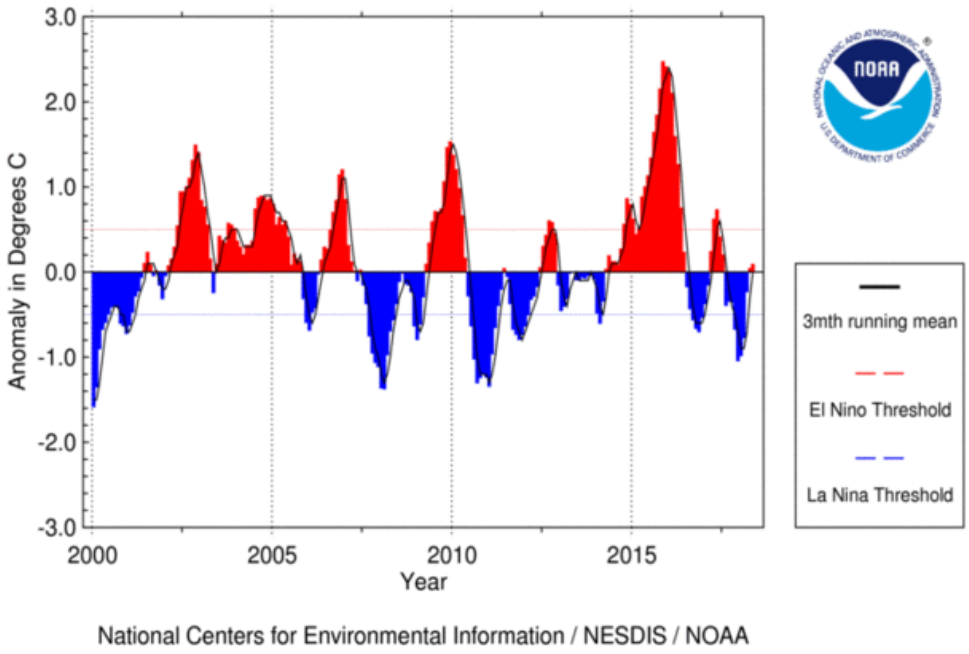

Figure 4.3: SST anomaly in Nino 3.4 region (5N-5S, 120-170W) through the years 2000-2018. Source: NOAA

4.2 Variability, persistence and climacogram of ENSO measured and reconstructed indexes, on multiple time scales

The ENSO variability, can be studied through the record of its indexes. The basic indices, through which the evolution of the ENSO phenomenon is observed, namely the Southern Oscillation Index (SOI), and the Oceanic Niño Index (ONI) have been presented in Section 4.1. In this chapter we will analyse the variability of the ENSO phenomenon on different time-scales through observed and reconstructed time-series of ENSO indices. In addition to the observed data, reconstructed value of indices through various proxies are utilized. The tool used to study the variability is the climacogram, presented on Chapter 2 and used to study the behaviour of the variability and the persistence of the time-series.

The ONI index for the years 1950-2018 is derived from the ERSSTv5 data (Huang et al., 2017) through an application of a high frequency filter. The data is provided by the National Oceanic and Atmospheric Administration (NOAA)[6], in a 3-month running mean of ERSSTv5 SST anomalies in the Niño 3.4 region (5^{o}N-5^{o}S, 120^o-170^{o}W). Periods which surpass the threshold of +/- 0.5^{o}C for five consecutive values, are considered to exhibit an El Niño or a La Niña phenomenon, for a positive or negative temperature values accordingly.

The SOI index is provided from two sources: The National Climate Centre of the Bureau of Meteorology of the Australian Government[7] provides a SOI index monthly time-series for the time period of 1876-2017 based on the monthly Mean Sea Level Pressure (MSLP) time-series of the Darwin and Tahiti stations. Additionally, the Climatic Research Unit of the University of East Anglia[8] also calculated through the normalized difference of the MSLP of the Darwin and Tahiti stations (Ropelewski and Jones, 1987), creating a time series of the SOI index for the years 1866-2017.

The three indices are represented in Figure 4.4, where their values have been normalised by subtracting the mean and diving by the standard deviation of each time series, in order for them to follow a common distribution. The high adaptation between the two SOI index time-series, and the variability of the ENSO phenomenon through the last century is evident from this figure.

[6] Available online:
http://origin.cpc.ncep.noaa.gov/products/analysis_monitoring/ensostuff/ONI_v5.php

[7] Available online: http://www.bom.gov.au/climate/current/soihtm1.shtml
[8] Available online: https://crudata.uea.ac.uk/cru/data/soi/

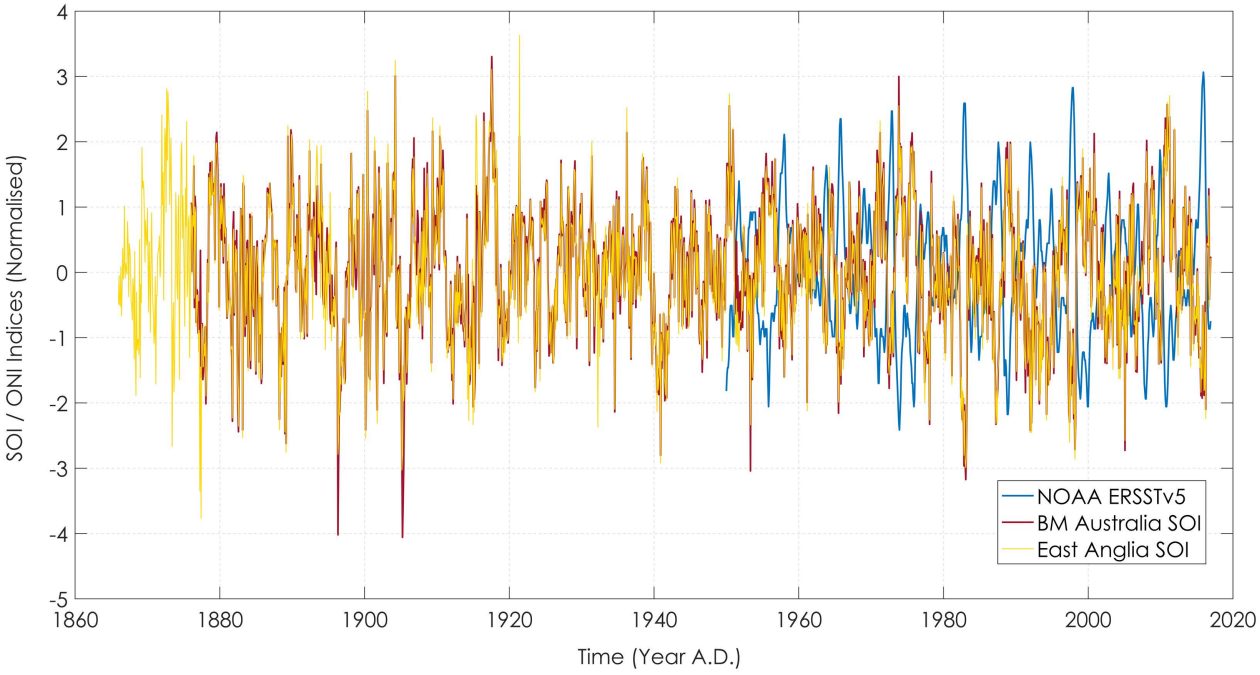

Figure 4.4: ONI Index for the years 1950-2018 (Source: NOAA), SOI Index for the years 1876-2017 (Source: BMC Australia), SOI Index for the years 1866-2017 (Source: University of East Anglia). All indices have been normalised

Li et al. (2013) reconstructed a seven-century-long ENSO index based on 2,222 tree-ring chronologies from both the tropics and mid-latitudes in both hemispheres. The authors derive certain conclusions from the reconstructed data:

"Our results show marked interdecadal–centennial variations in ENSO amplitude that modulate its effects on extratropical climate, suggesting that ENSO variance, rather than alternative mechanisms such as mid-latitude waveguide modulation, is a primary control of the modulations. On longer timescales, ENSO variance is low in the early LIA period and high in the twentieth century. The elevated ENSO variability in recent decades is unprecedented over the past seven centuries, suggesting a response to increased anthropogenic radiative forcing […] Although ENSO is an internal mode of the coupled system, our analysis with a large sample size reveals a robust response to large tropical volcanic eruptions. [...] The response to the 11-year solar cycle is inconsistent in phase over the record, possibly because of weak forcing"

The reconstructed time series of the ENSO Index based on Tree Ring data is visualized in Figure 4.5 for the years 900-2000 A.D.

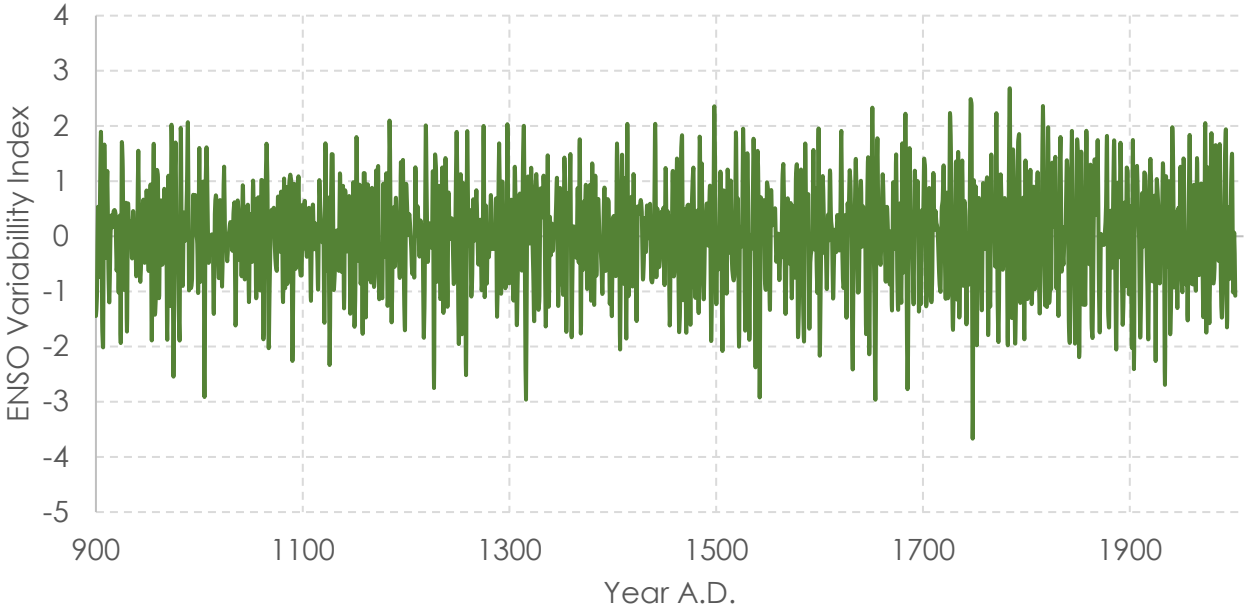

Figure 4.5: Reconstructed SOI Index through tree-ring data for the years 900-2000 from Li et al. (2013)

McGregor et al. (2010) combined different proxy reconstructions of ENSO indices to consolidate their common signal into one individual proxy titled the Unified ENSO Proxy (UEP). The study presents a high correlation between the UEP and the proxies used for its construction, and according to the authors it "p*rovides better representation of observed indices of ENSO, discrete ENSO events and documented historical chronologies of ENSO than any of the input ENSO reconstructions".* Additionally, this study shows shows that "*multi-year El Nino events similar to the 1990–1995 event have occurred several times over the last 3 1/2 centuries"* and is consistent with the previously presented study of Li et al. (2013) in showing the effect of volcanic eruptions on ENSO variability. The UEP reconstruction over the period 1650-1977 is illustrated in Figure 4.6

Lastly, Moy et al. measured and constructed a record of sedimentation in Laguna Pallcacocha, southern Ecuador, which is strongly influenced by ENSO variability, and covers the past 12,000 years continuously. The authors *"find that changes on a timescale of 2–8 years, which we attribute to warm ENSO events, become more frequent over the Holocene until about 1,200 years ago, and then decline towards the present. Periods of relatively high and low ENSO activity, alternating at a timescale of about 2,000 years, are superimposed on this long-term trend. We attribute the long-term trend to orbitally induced changes in insolation and suggest internal ENSO dynamics as a possible cause of the millennial variability."*. The reconstructed 11,000-year Laguna Pallcacocha Sediment Red Colour Intensity data, that is used as a proxy of the ENSO phenomenon, and depicted in Figure 4.7, shows a low concentration of ENSO events in the early Holocene, followed by an increasing occurrence after 7,000 years before present (B.P.), with a peak event frequency around 1,200 years B.P and a decline then onwards. Additionally, around 5,000 years B.P. the periodical oscillation shifts from a

1,500-year period in the middle/early Holocene to a 2,000-year period in the late Holocene. It is shown that internal mechanisms of ENSO variability, in addition with deterministic orbital and carbon cycle forcings, account for this oscillation periods and their shifts through the Holocene era. This will also be shown in the climacogram of the time-series.

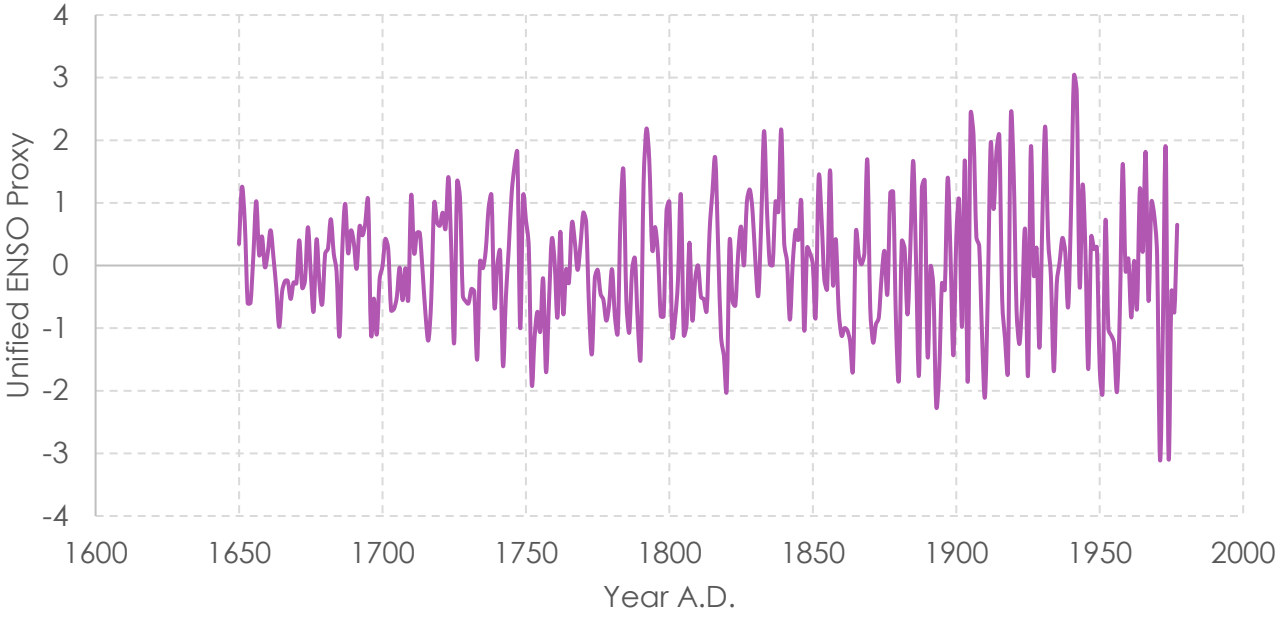

Figure 4.6: Unified ENSO Proxy reconstruction for the years 1650-1977 from McGregor et al. (2010)

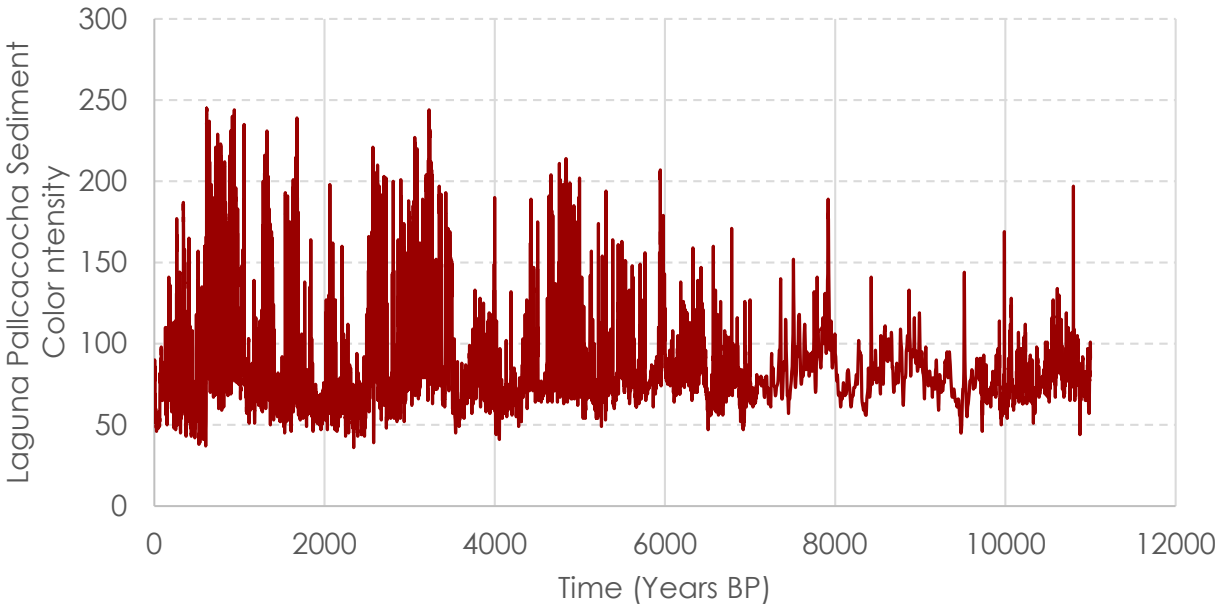

Figure 4.7: Red Intensity of the Laguna Pallcacocha Sediment through a period of 11,000 years before present from Moy et al. (2002)

The climacograms are constructed through the methodology presented in Chapter 2. The aggregated standard deviation $\sigma^{(k)}$ of each of the time-series present before, is calculated for multiple scales *k*, and their values are plotted on a log-log plot.

As stated in Chapter 2, the slope α of the log-log plot signifies the value of the Hurst Coefficient via the equation:

$$a = 1 - H \tag{4.1}$$

Although many values of scales *k* are plotted in the climacograms presented here, the value of the Hurst Coefficient is only for the part of the climacogram that combines the following criteria:

- Shows a constant linear slope, usually occurring after several small time-scales on which a more horizontal slope is found, due to bias on small-time scale values.
- Does not exceed the scale value of $k = L / 10$, where L is the time Length of the time-series, calculated as the product of the data length of the time series n with its time step (or resolution).

The climacograms of the ENSO indices time-series are shown through Figures 4.8-4.13. The slope which is used to calculate the value of the Hurst Coefficient is shown with a red line in Figures 4.8-4.12 and with dashed lines in Figure 4.13. The values of the Length, the time step and the Hurst Coefficient of each time-series are presented in Table 4.1.

Here we present basic conclusions on the ENSO variability and persistent behaviour:

1. The climacogram of the ONI index (Figure 4.8), shows a strong anti-persistent behaviour, with a Hurst Coefficient of $H = 0.166$ for scales of 2 months to almost a yearly scale. An anti-persistent behaviour also applies for the two SOI index time-series, on the same scales, but with much higher Hurst Coefficient values (less strong anti-persistence), of $H = 0.398$ for the BMC Australia time-series (Figure 4.9) and $H = 0.462$ for the East Anglia time-series (Figure 4.10). This is easily understood and explained from the variability of the ENSO indices that portray a fluctuation between opposite "El Nino" and "La Nina" phases, shown by positive and negative values on their indices. The anti-persistent behaviour signifies exactly this "switch" between high and low values. The existence of a long-term anti-persistence behaviour can be examined by observing the climacogram of time-series occurring on higher scale values.
2. The climacograms of the Li et al. (2013), (Figure 4.11) and the McGregor et al. (2010) (Figure 4.12) ENSO index reconstructions, show the occurrence of an anti-persistent behaviour on higher time scales of 10 to 100 years, which can signify a long-term anti-persistent behaviour of the ENSO phenomenon on these time-scales. Specifically, the values of $H = 0.384$ for the first and $H = 0.225$ for the second time-series are low enough to support the previous argument.

3. The climacogram of Moy et al. (2002) Red Intensity data (Figure 4.13), which illustrates the behaviour of the ENSO variability on time scales spanning 10 to ~1.1 thousand years, shows a different behaviour. A long-term persistent behaviour is observed through scales of 10 to ~300 years, with a constant slope depicting a Hurst Coefficient of $H = 0.84$. This result coincides with that of Wang and Tsonis (2008), which noted a Hurst Coefficient of $H = 0.85$ for the Red Intensity time-series, through a method of calculation different than the climacogram. After the scale of ~300 years a fluctuation occurs at the climacogram until the scale of ~500 years which turns into a constant drop of slope until the scale of ~1.1 years, depicting a very low Hurst Coefficient value of $H = 0.08$. This signifies two cases: (a) An anti-persistent behaviour occurring on higher time-scales for the ENSO phenomenon, and/or (b) A deterministic forcing, and a periodical cycle occurring through the time-series on these scales which creates a sudden drop on the climacogram (see Chapters 2 and 3). As discussed in Moy et al. (2002) the latter case is evident by orbital and carbon cycle forcings which occur on the time scale periods from ~1.500-2000, but also internal ENSO variability that creates a fluctuation on these periods. The shape of the climacogram reaffirms this statement. The strong persistent behaviour found on low time scales shows a strong internal variability of the ENSO phenomenon while the sudden drop can be accounted to periodical external forces. The combination of these two processes on a theoretical model, creating the theoretical climacogram of the ENSO process, in the same means that it is carried on in Chapter 3, could easily coincide with the values of the empeirical climacogram.

Overall it is observed through the climacogram analysis that the ENSO process, exhibits a strong anti-persistent behaviour on time scale values of 2 months to 1 year, but also on higher time scale values of 10-100 years. A strong persistent behaviour on medium scales appearing on the climacogram of the Red Intensity data possibly shows strong internal variability of the ENSO phenomenon, and high uncertainty in its evolution on this time-scales. Finally, the drop of the climacogram on time scales of ~1,000 years, shows the effect of periodical deterministic forcings such as orbital cycles on the ENSO variability.

Table 4.1 Properties of the ENSO indices time-series

Time-series Source	**Length (L) (years)**	**Original (O) or Regularized (R) Resolution (Δ) (years)**	**Hurst Coefficient (H)**
NOAA (ONI)	68	1/12 (O)	**0.166**
BMC Australia	141	1/12 (O)	**0.398**
Uni. East Anglia	151	1/12 (O)	**0.462**
Li et al. (2013)	1100	1 (O)	**0.384**
McGregor et al. (2010)	327	1 (O)	**0.225**
Moy et al. (2002)	11,000	1 (R)	**0.84** (k=10-300) **0.08** (k=500-1100)

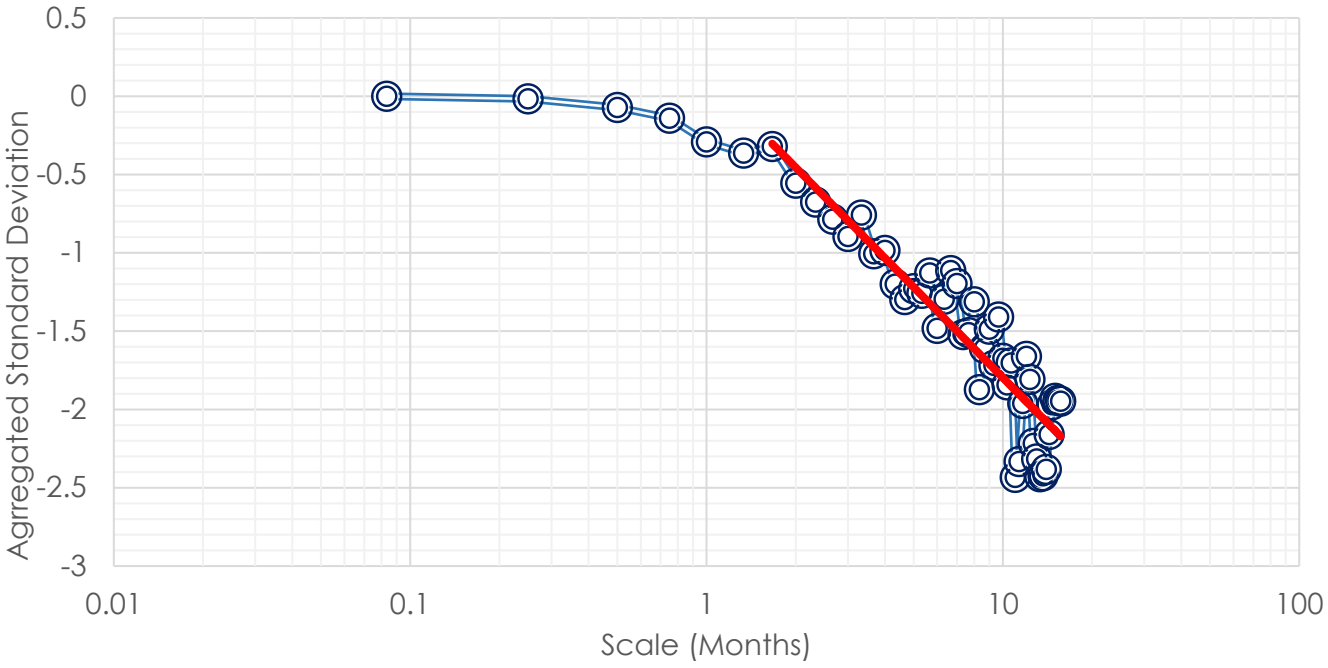

Figure 4.8: Climacogram of the ONI index, scale values in months. Source: NOAA

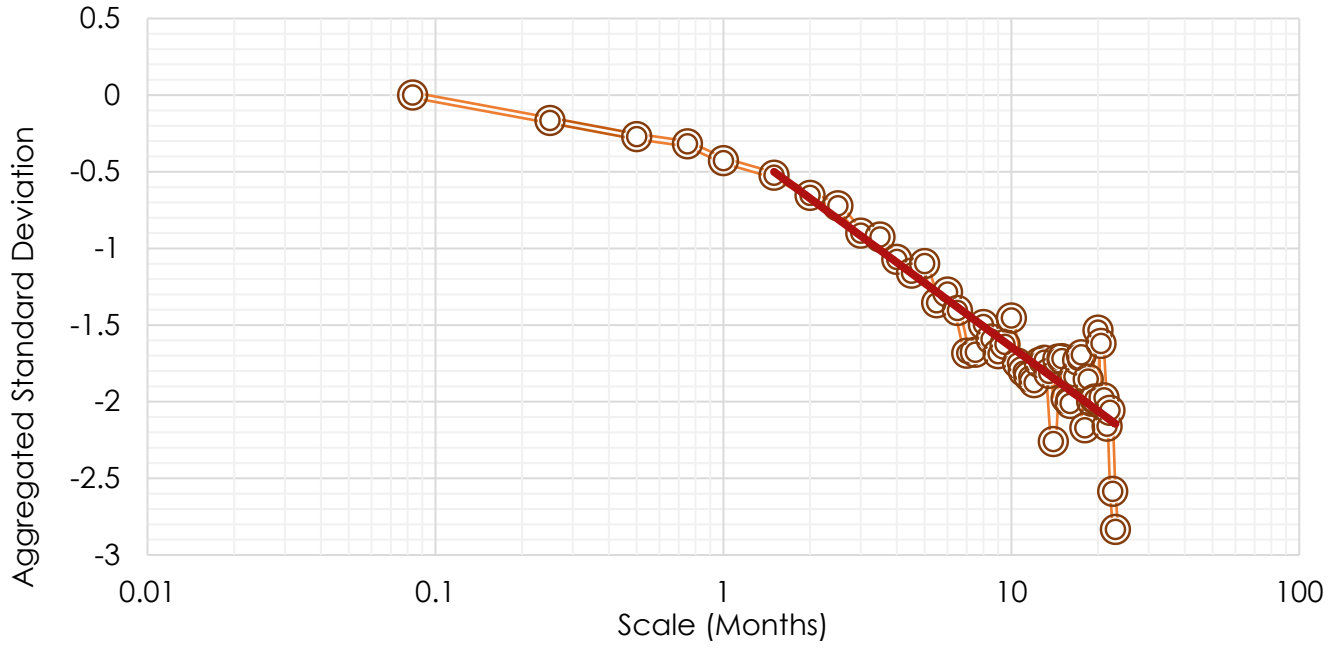

Figure 4.9: Climacogram of the SOI index, scale values in months. Source: BMC Australia

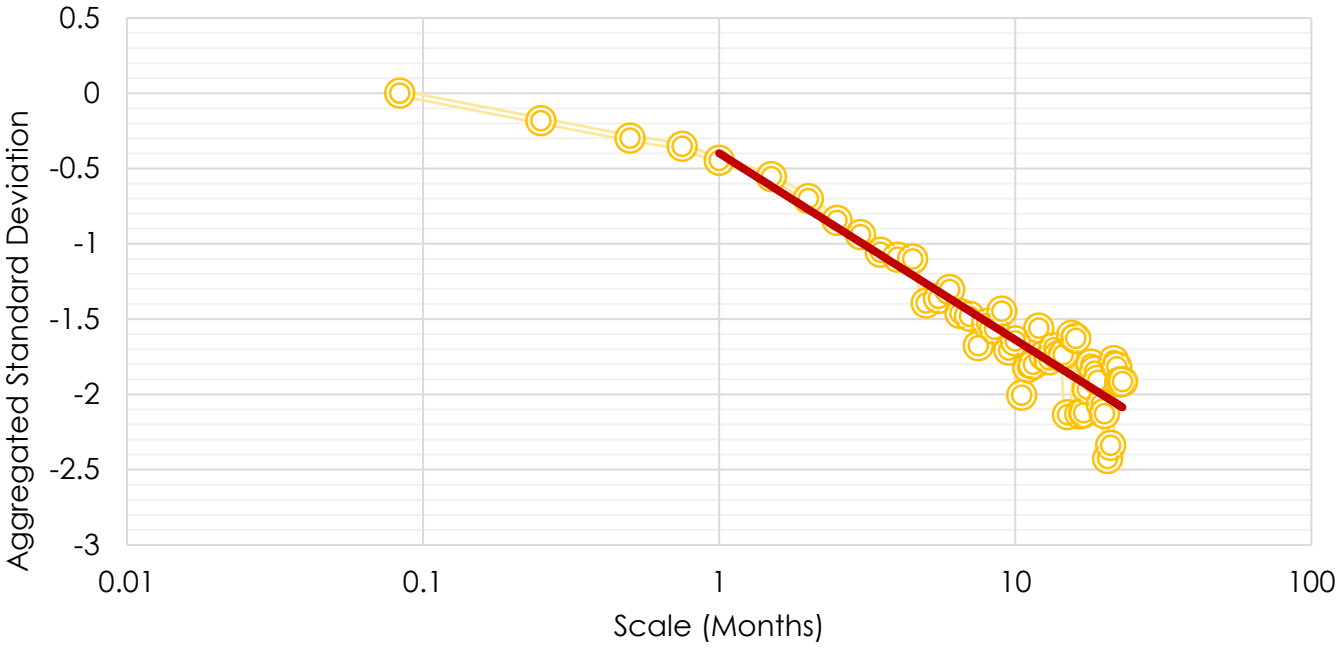

Figure 4.10: Climacogram of the SOI index, scale values in months. Source: University of East Anglia

Figure 4.11: Climacogram of the tree-ring reconstructed ENSO index by Li et al. (2013), scale values in years.

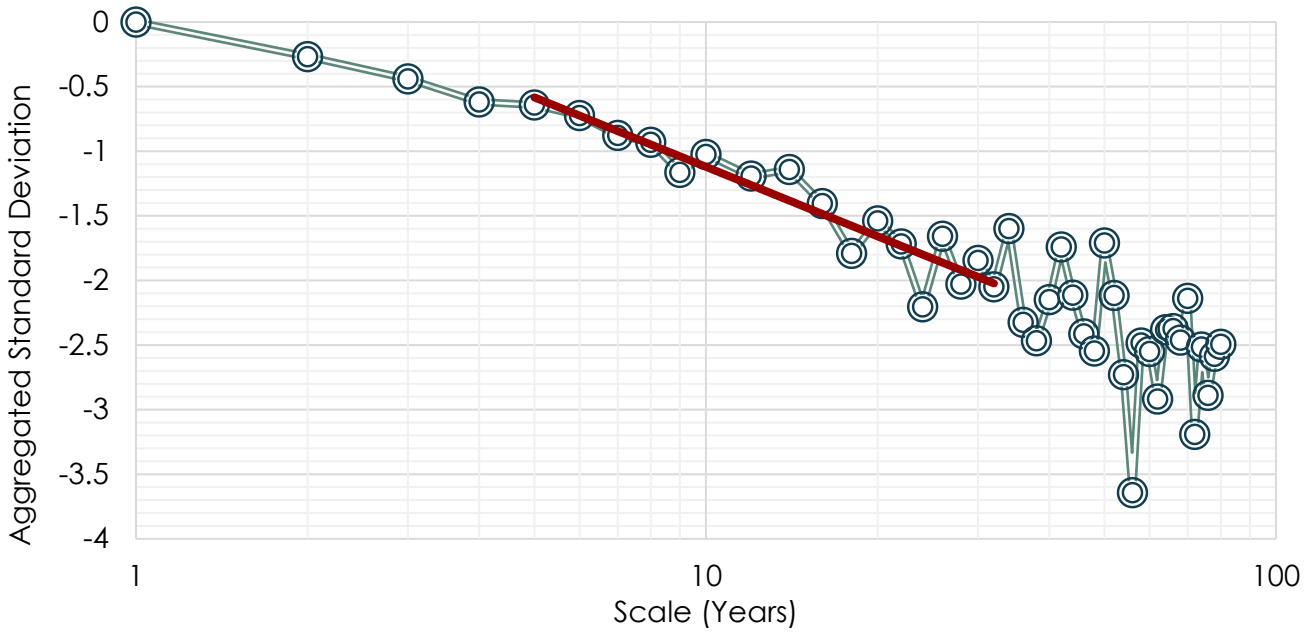

Figure 4.12: Climacogram of the Unified ENSO Proxy index by McGregor et al. (2010), scale values in years.

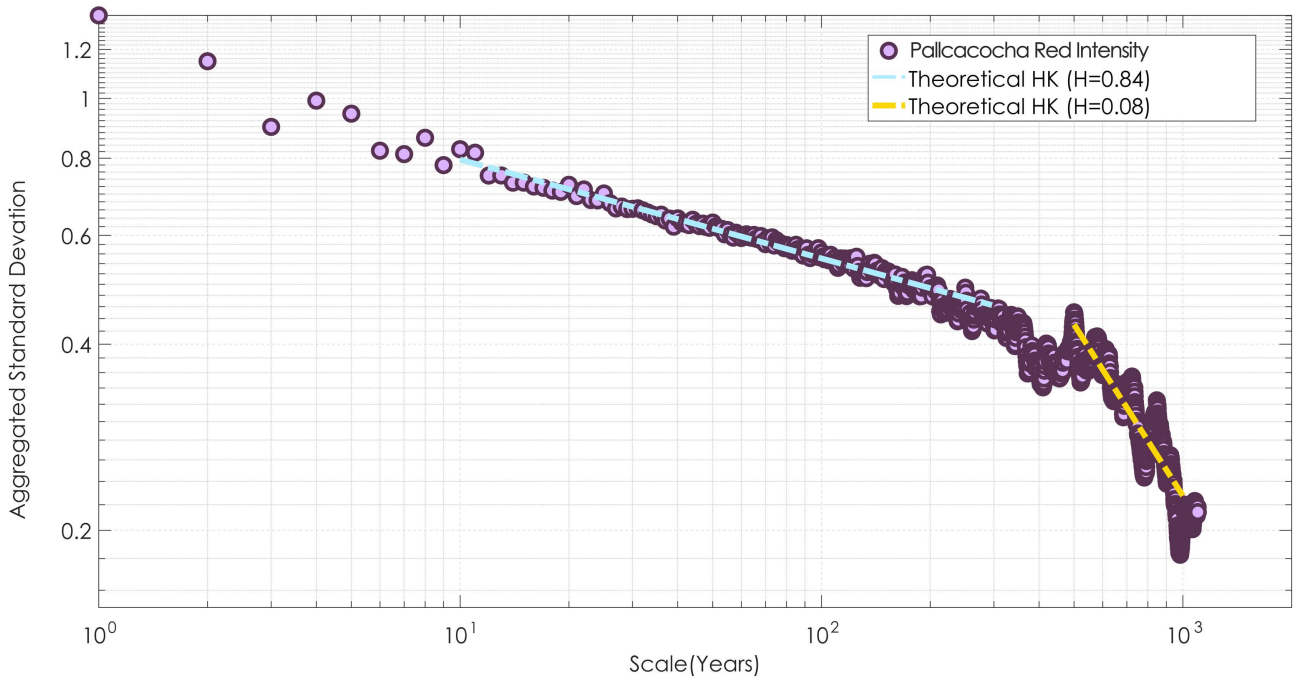

Figure 4.13: Climacogram of the Pallcacocha Red Intensity proxy by Moy et al. (2002), scale values in years.

4.3 Spatial and temporal persistence in the global SST reconstruction

The Extended Reconstructed Sea Surface Temperature (ERSST) dataset (Huang et al. 2015a, Liu et al. 2015) is a global monthly sea surface temperature analysis on a 2x2 degree grid derived from the International Comprehensive Ocean-Atmosphere Dataset (ICOADS). The latest ERSST Version 5 (Huang et al. 2017) is used for this study, which provides a global gridded SST reconstruction from the year 1854 until the year 2018[9].

The Extended Reconstructed Sea Surface Temperature (ERSST) dataset is a global monthly sea surface temperature dataset derived from the International Comprehensive Ocean–Atmosphere Dataset (ICOADS). Production of the ERSST is on a 2° × 2° grid with spatial completeness enhanced using statistical methods. This monthly analysis begins in January 1854 continuing to the present and includes anomalies computed with respect to a 1971–2000 monthly climatology.

The original gridded time-series has a monthly time resolution. In order to analyze its properties, the time series is presented into three forms, of which the first is the original one, and the other two are created through averaging:

(a) The original monthly time-series
(b) An aggregated annual time-series
(c) The twelve annual time series for each of the twelve months of the year.

Through the two transformations of the original time-series the cyclostationarity, evident in the evolution of the autocorrelation structure as shown later, is removed, and thus the persistence can be observed.

The autocorrelation structure of these three gridded time series is analyzed by examining the evolution of the autocorrelation factor (ACF) through time lag, and the value of the Hurst coefficient which portrays the long-term correlation or persistence statue in the time-series. The ACF is calculated through a simple algorithm for the autocorrelation function as shown in equation (2.8) of Chapter 2. The Hurst coefficient is calculated through a simple algorithm for an averaged process at scale Δ, as shown in equation T2.4 of Table 2 in Chapter 2. It is reminded here that:

- For $H = 0.5$ the process reduces to pure white noise.
- For $0.5 < H < 1$ the process exhibits Long Term Persistence (or Long-Range Dependence) and is called a persistent process.
- For $0 < H < 0.5$ it is called an anti-persistent process.

[9] Data can be accessed through the site of NOOA: https://data.nodc.noaa.gov/cgi-bin/iso?id=gov.noaa.ncdc:C00884

We present here the results of the algorithms on gridded figures with the same spatial analysis as the original ERSST data:

1. The values of the Hurst Coefficient for the monthly time-series (a) are illustrated in Figure 4.14
2. The values of the Hurst Coefficient for the annual time-series (b) are illustrated in Figure 4.15
3. The values of the Hurst Coefficient for the twelve annual time-series for the twelve months of the year (c) are illustrated in the twelve windows of Figure 4.16
4. The values of the ACF for the monthly time-series (a) for monthly time lags of 2 consecutive years (24 total values) are illustrated in the twenty-four windows of Figure 4.17 (a and b).
5. The values of the ACF for the annual time series (b) for annual lags for 24 consecutive years are illustrated in the twenty-four windows of Figure 4.18 (a and b).
6. The values of the ACF for the twelve annual time-series for the twelve months of the year (c), for a time lag of one year are illustrated in the twelve windows of Figure 4.19.

By examining the values of the Hurst Coefficient of the monthly ERSST time-series (a), in Figure 4.14, strong *H* values are observed through various oceanic regions around the equator. Specifically values of Hurst coefficient greater than *0.75* are concentrated in the area of the equatorial pacific especially in the Nino 3.4 and Nino 4 areas, but also in the Indonesian seas, the northern Indian ocean and the equatorial Atlantic. Additional areas of high Hurst values are spotted southwards but are outside of the purposes analyzed here.

By examining the ACF evolution for the monthly ERSST time-series (a), through monthly lags, in Figure 4.17 we can observe evidence of an annual cyclostationarity in the modeled time-series. Characteristically, the twelve windows for the monthly lags of 1-12 show identical shape with those for lags of 13-24 months. In the second case, the monthly evolution of the ACF values in preserved, due to internal cyclostationarity of the time-series, while the high ACF values observed during the first-year lags (lags 1-12 months), are decreasing. The picture of windows 13-24, depicted in Figure 4.7b is repeating for longer modeled time lags up to 10 years, as the high autocorrelation values have already dropped from year 2 (after ~24 lags). For this reason, no more time windows were illustrated here. Consequently, the internal cyclostationarity needs to be firstly removed to unmask long-term persistence through the Hurst Coefficient, as the high *H* values depicted in Figure 4.14, which spatially coincide with those of Figure 4.17 in the equatorial Pacific, are affected by the cyclostationarity. This is done by creating the aggregated time series (b) and (c) as explained earlier and analyzing the ACF and the Hurst Coefficient in these time series.

By examining the Hurst Coefficient of the annual ERSST time-series (b), in Figure 4.15, the picture is reversed. Strong Hurst coefficient values, larger than *0.75*, even reaching higher than *0.9* in many cases, are observed throughout the globe, showing an intense persistent behavior of the SST variable. At the same time, in Nino 3 (including

3.4) and 1,2 areas the values of Hurst coefficient are around 0.5, moving to less than 0.5 in Nino 1,2 areas. This implies a white-noise behavior of the SST in the area of the Nino 3.4 area, while at the same time a mild anti-persistent behavior in Nino 1,2 and part of the Nino 3 area. The first is attributed to the cyclical pattern of the El Nino phenomenon, which while not strictly periodical follows a biennial to septennial cycle, at the modeled time-scale. The latter agrees with the climacogram studies of the measured and reconstructed Nino Indexes time-series, analyzed in Chapter 4.2, which show anti-persistent behavior on small time scales.

By examining the ACF evolution for the annual ERSST time-series (b), through Figure 4.18, we observe the exact pattern depicted through the Hurst coefficient, on the first window, which shows the ACF for a lag of 1 year. Following the increase of yearly lags, we can note a strong auto-correlation structure on certain areas of the Pacific Ocean, which imply long-term persistent behavior that explains a part of the persistence shown in Figures 4.14 and 4.17 which is not masked by the monthly time-series cyclostationarity. Still, some of the values of the annual time-series are masked by internal cyclostationarity, which is only fully removed through the separation of the time-series for each month, done in formation (c), analyzed here onwards.

By examining the Hurst coefficient for the annual ERSST time-series for each of the twelve months of the year (c), in Figure 4.16, we observe a pattern common to that of Figure 4.15. This shows that cyclostationarity has been removed, when the annual time-series is plotted. Even more, in Figure 4.16 the anti-persistent behavior in Nino 3.4, 3, 2 and 1 regions is more evident, as the Hurst coefficient reaches values of 0.3 for specific months in the area of the El Nino Oscillation. Additionally, the length of the anti-persistent (blue-coloured) area, which changes depending on the modeled month might be connected to the months of strong ENSO presence in the equatorial. The ACF for lag values of 1 year for the same time-series, depicted in Figure 4.19, shows the same pattern as that of Figure 4.6, with low ACF values in Nino areas and an important autocorrelation structure in some areas of the Pacific Ocean.

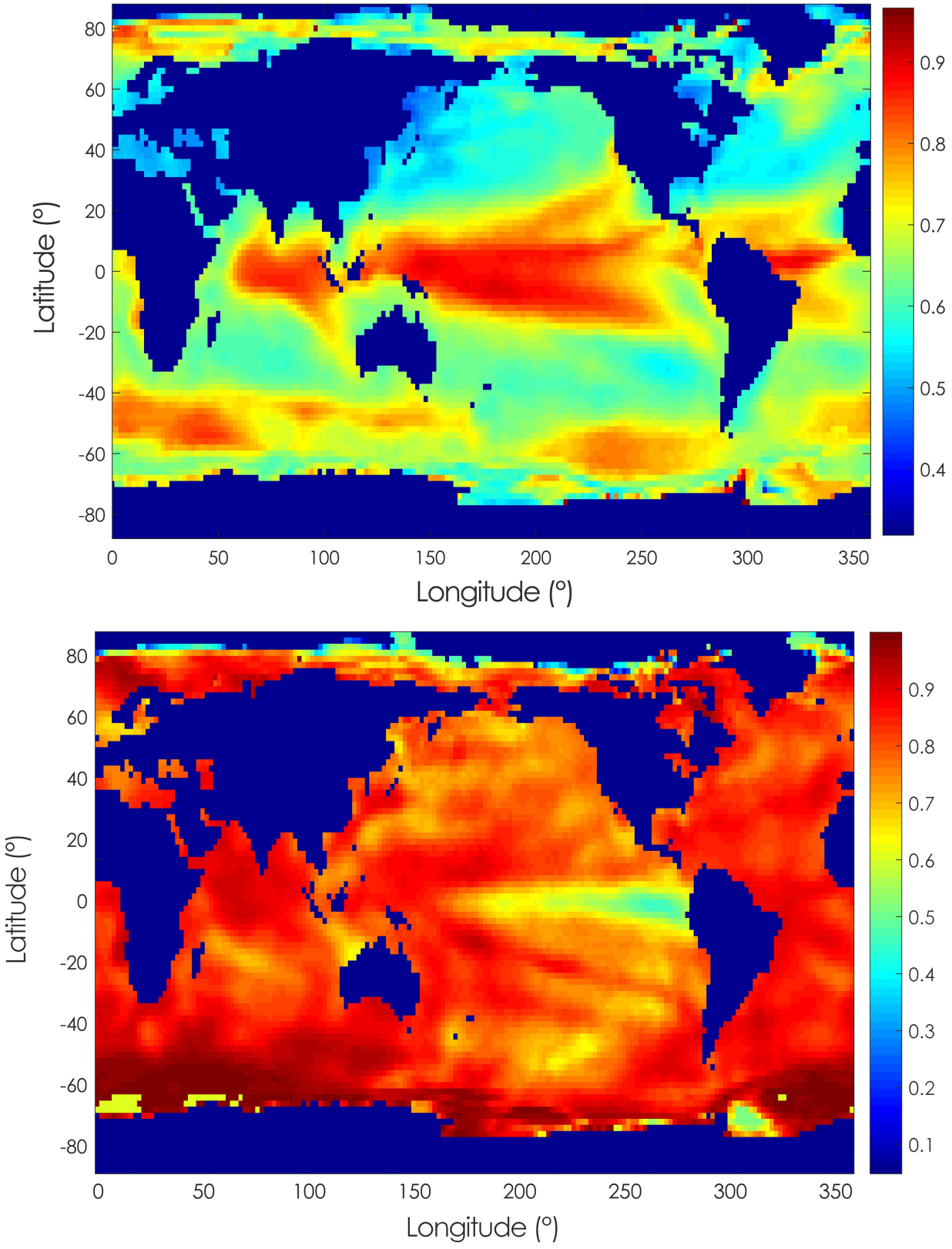

Figure *4.14 (top) and Figure 4.15 (bottom): Hurst Coefficient (H) values of the Monthly (top) and the Annual (bottom) ERSSTv5 time-series*

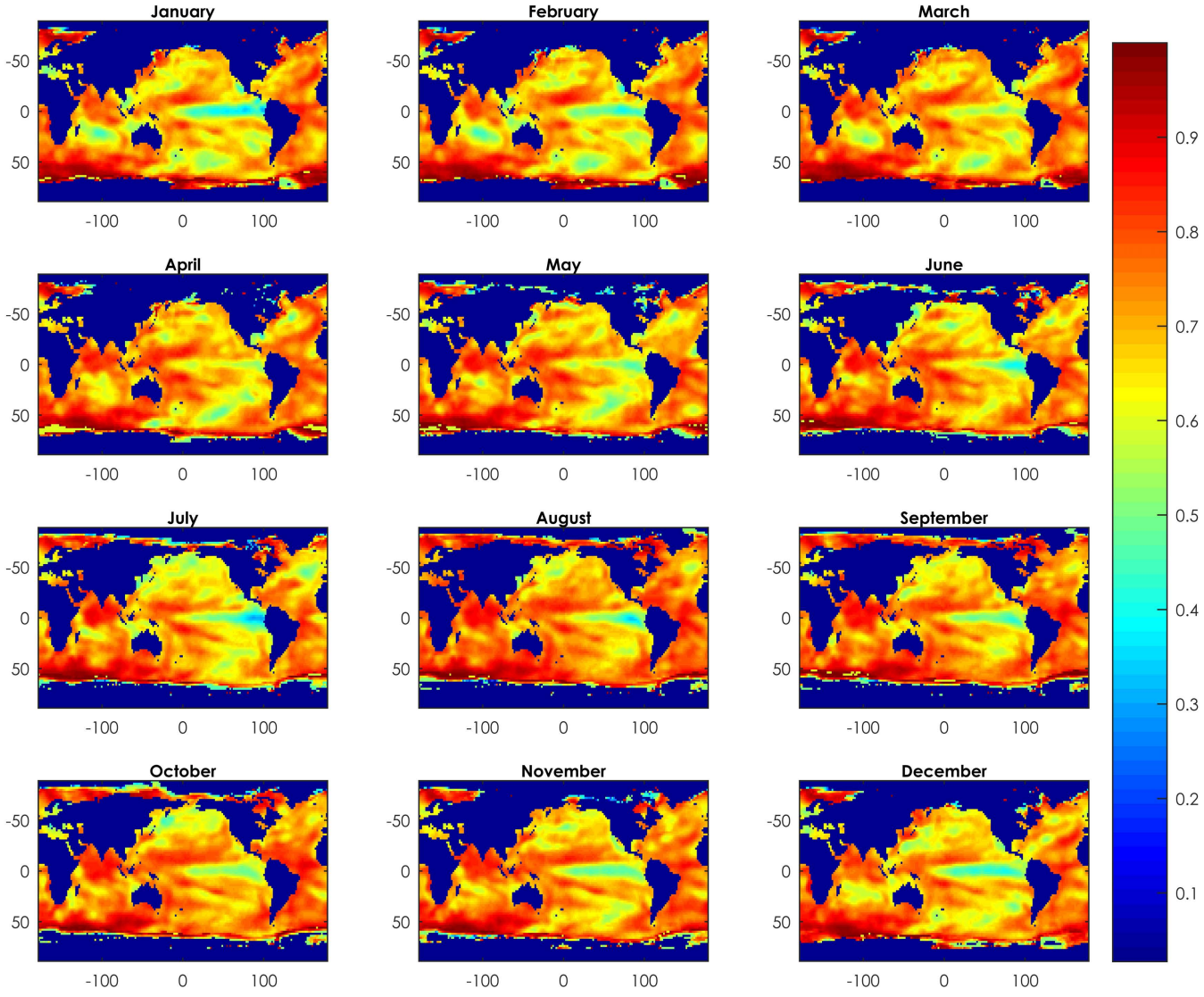

Figure *4.16: Hurst Coefficient (H) values of the twelve Annual ERSSTv5 time-series for each of the twelve months of the year.*

a.

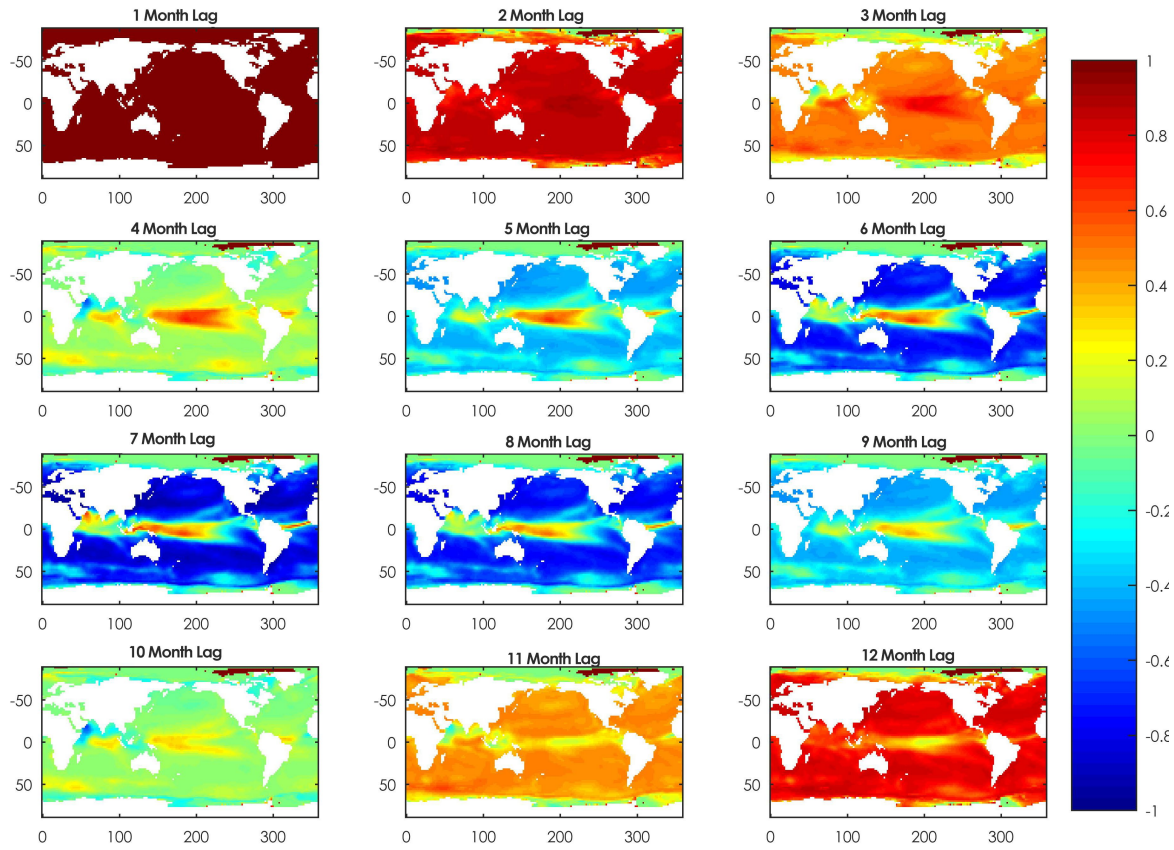

b.

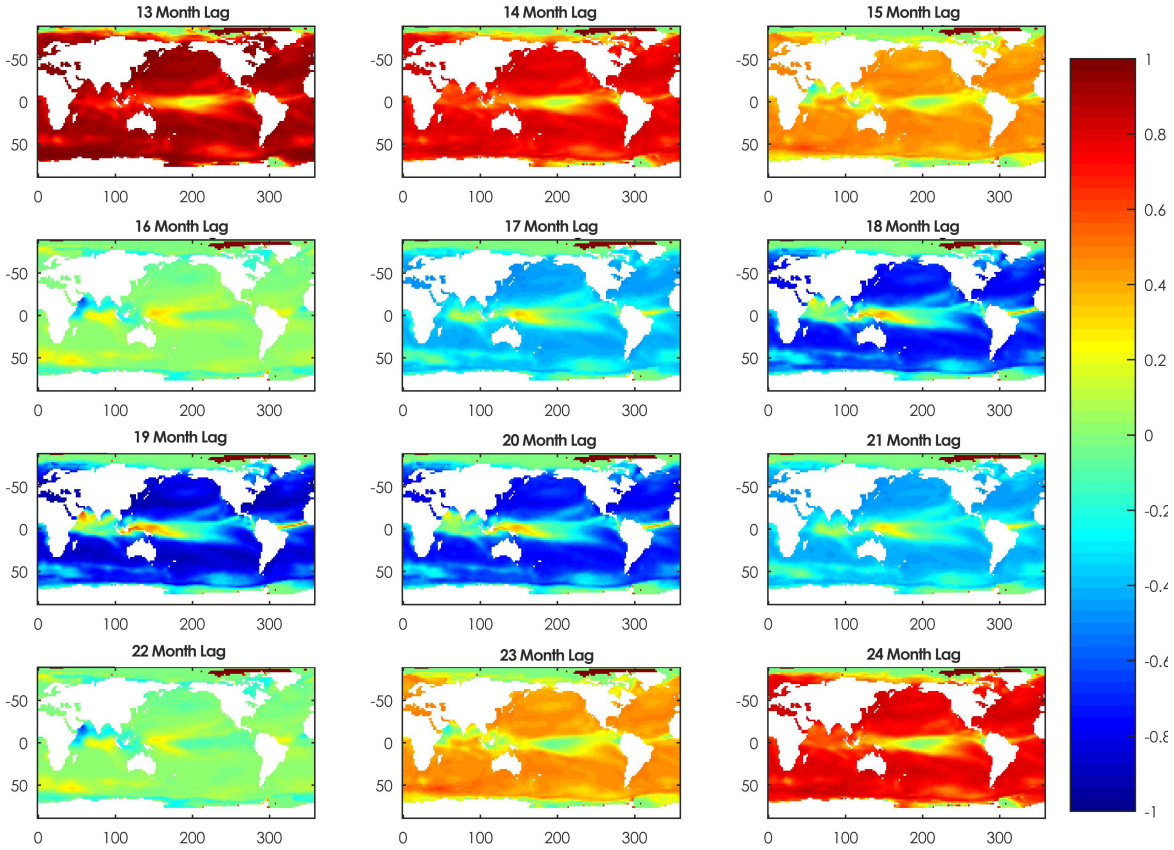

Figure 4.17 (a and b): Autocorrelation Factor (ACF) values of the Monthly ERSSTv5 time-series for 24 yearly lags.

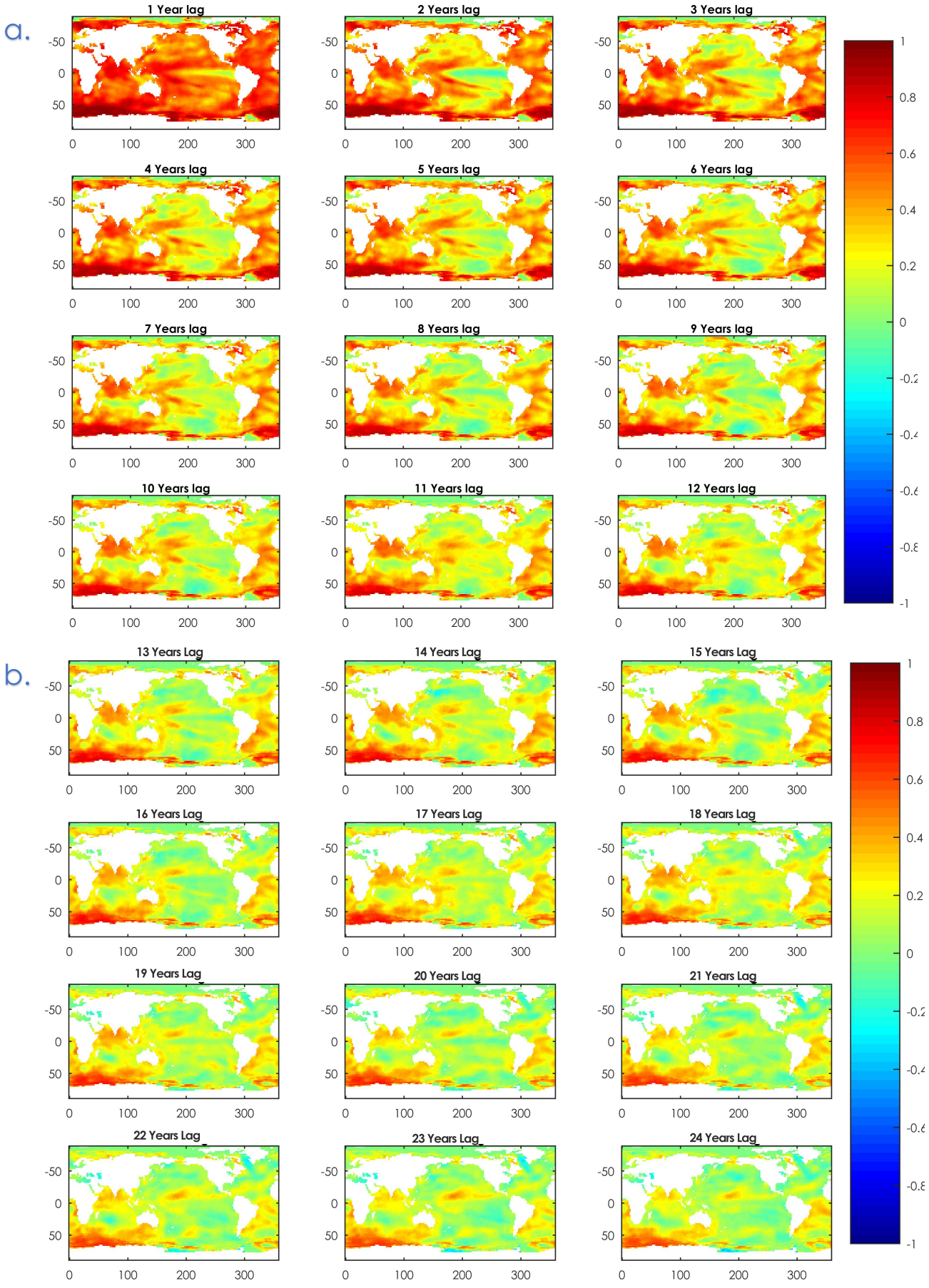

Figure 4.18 (a and b): Autocorrelation Factor (ACF) values of the Annual ERSSTv5 time-series for 24 yearly lags.

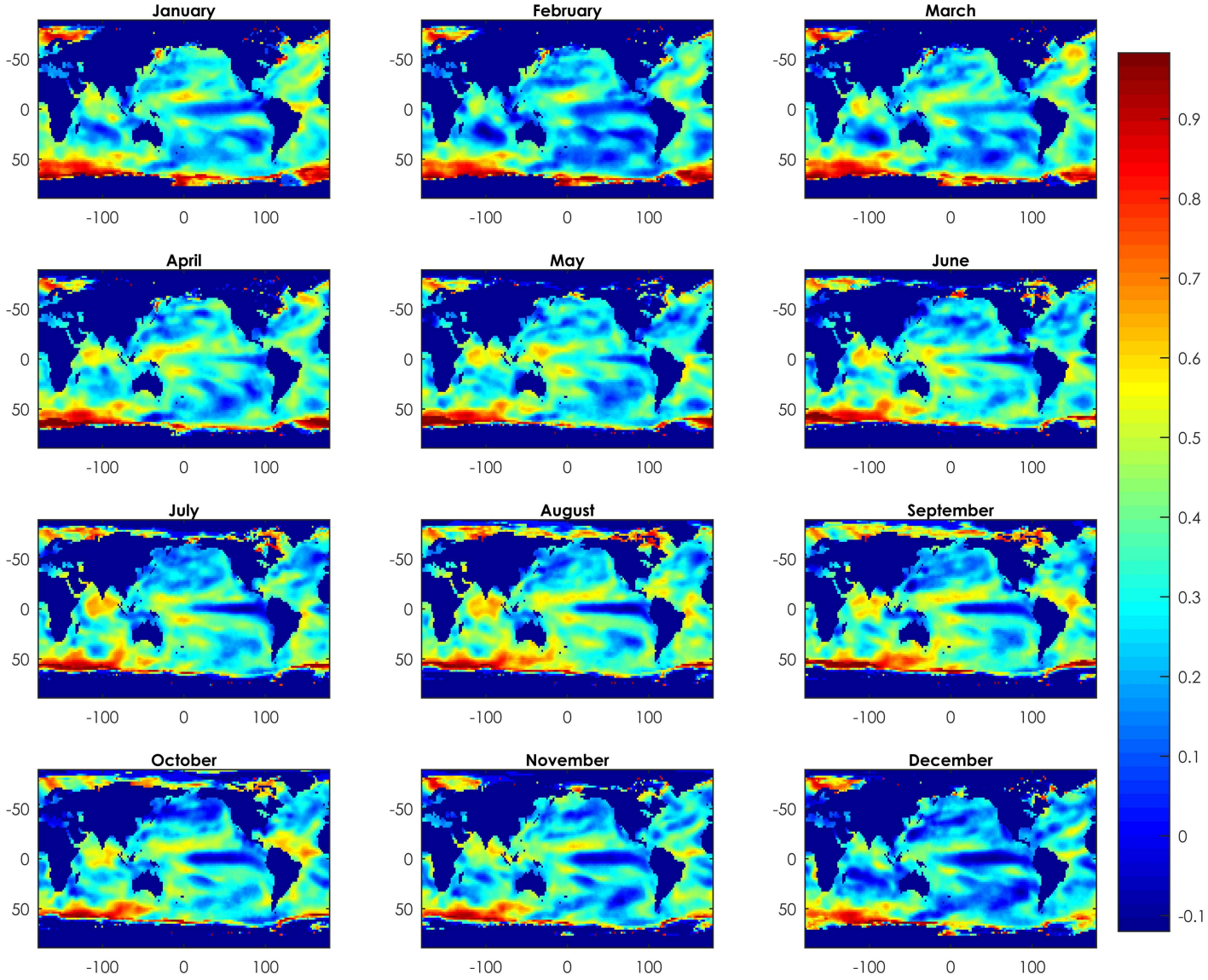

Figure *4.19: Autocorrelation Factor (ACF) values of the twelve Annual ERSSTv5 time-series for each of the twelve months of the year, for a yearly lag.*

References

Alvarez-Ramirez J, Alvarez J, Dagdug L, Rodriguez E, Carlos Echeverria J (2008) Long-term memory dynamics of continental and oceanic monthly temperatures in the recent 125 years. Phys A 387(14):3629–3640

Aristotle: Meteorologica. (1952) Harvard University Press

Ashkenazy Y, Baker DR, Gildor H, Havlin S (2003) Nonlinearity and multifractality of climate change in the past 4,20,000 years. Geophys Res Lett. doi: 10.1029/2003GL018099

Ashkenazy Y, Tziperman E (2004) Are the 41 kyr glacial oscillations a linear response to Milankovitch forcing? Quat Sci Rev 23(18–19):1879–1890

Aviso (2003) AVISO and PODAAC user handbook—IGDR and GDR jason products. Edition 2.0. SMM-MU-M5-OP-13184-CN

Awadallah, A. G. (2014). Evolution of the Nile River drought risk based on the streamflow record at Aswan station, Egypt. *Civil Engineering and Environmental Systems*, *31*(3), 260-269.

Barth, Michael C., and James G. Titus. "Greenhouse effect and sea level rise: A challenge for this generation." (1984).

Becker, M., Mikhail Karpytchev, and S. Lennartz-Sassinek. "Long-term sea level trends: Natural or anthropogenic?." *Geophysical Research Letters* 41.15 (2014): 5571-5580.

Benada JR (1997) PO.DAAC Merged GDR (TOPEX/POSEIDON) Generation B user's handbook, version 2.0, JPL D-11007

Ben-Naim, A. (2008). A Farewell to Entropy: Statistical Thermodynamics Based on Information: S. World Scientific.

Benzi R, Parisi G, Sutera A, Vulpiani A (1981) Stochastic resonance in climatic change. Tellus 34(1):10–16

Beran, J. (1994) Statistics for Long-Memory Processes, vol. 61 of Monographs on Statistics and Applied Probability, Chapman and Hall, New York, USA.

Berger A, Li XS, Loutre MF (1999) Modelling northern hemisphere ice volume over the last 3 Ma. Quat Sci Rev 18:1–11

Berger AL (1978) Long- term variations of daily insolation and quaternary climatic changes. J Atmos Sci 35:23622367

Bolshakov VA (2008) How long will the ‘precession epoch’ last in terms of Pleistocene glacial cycles? Rus J Earth Sci 10:ES3004

Box, G. E., Jenkins, G. M., Reinsel, G. C., & Ljung, G. M. (2015). *Time series analysis: forecasting and control*. John Wiley & Sons.

Boyin Huang, Viva F. Banzon, Eric Freeman, Jay Lawrimore, Wei Liu, Thomas C. Peterson, Thomas M. Smith, Peter W. Thorne, Scott D. Woodruff, and Huai-Min Zhang (2015b) Extended Reconstructed Sea Surface Temperature (ERSST), Version 4. [NetCDF] NOAA National Centers for Environmental Information. doi:10.7289/V5KD1VVF [05/2018].

Bruun, Per. "Sea-level rise as a cause of shore erosion." *Journal of the Waterways and Harbors division* 88.1 (1962): 117-132.

Chaitin, G. J. (1975). Randomness and mathematical proof. *Scientific American*, *232*(5), 47-53.

Church, J. A., & White, N. J. (2006). A 20th century acceleration in global sea-level rise. *Geophysical research letters*, *33*(1).

Church, J. A., & White, N. J. (2011). Sea-level rise from the late 19th to the early 21st century. *Surveys in geophysics*, *32*(4-5), 585-602.

Church, J. A., Clark, P. U., Cazenave, A., Gregory, J. M., Jevrejeva, S., Levermann, A., ... & Payne, A. J. (2013). *Sea level change*. PM Cambridge University Press.

CNES (2009) OSTM/Jason-2 Products Handbook. SALP-MU-M-OP-15815-CN

Dangendorf, S., Marcos, M., Müller, A., Zorita, E., Riva, R., Berk, K., & Jensen, J. (2015). Detecting anthropogenic footprints in sea level rise. *Nature communications*, *6*, 7849.

Dangendorf, S., Rybski, D., Mudersbach, C., Müller, A., Kaufmann, E., Zorita, E., & Jensen, J. (2014). Evidence for long-term memory in sea level. Geophysical Research Letters, 41(15), 5530-5537.Ditlevsen P (2009) Climate transitions on long timescales. Contem Phys 50(4):511–532

De Boer, B., Lourens, L. J., & Van De Wal, R. S. (2014). Persistent 400,000-year variability of Antarctic ice volume and the carbon cycle is revealed throughout the Plio-Pleistocene. *Nature communications*, *5*, 2999.

De Boer, B., Van de Wal, R. S. W., Lourens, L. J., Bintanja, R., & Reerink, T. J. (2013). A continuous simulation of global ice volume over the past 1 million years with 3-D ice-sheet models. *Climate dynamics*, *41*(5-6), 1365-1384.

Dimitriadis, P. (2017). Hurst-Kolmogorov dynamics in Hydrometeorological processes and in the microscale of turbulence.

Dimitriadis, P., & Koutsoyiannis, D. (2015). Climacogram versus autocovariance and power spectrum in stochastic modelling for Markovian and Hurst–Kolmogorov processes. Stochastic environmental research and risk assessment, 29(6), 1649-1669.

Drysdale RN, Hellstrom JC, Zanchetta G, Fallick AE, Sanchez Goni MF, Couchoud I, McDonald J et al (2009) Evidence for obliquity forcing of glacial termination II. Science 325(5947):1527–1531

Eichner JF, Koscielny-Bunde E, Bunde A, Havlin S, Schellnhuber H-J (2003) Power-law persistence and trends in the atmosphere: a detailed study of long temperature records. Phys Rev E 68:046133

Ercan, A., Kavvas, M. L., & Abbasov, R. K. (2013). *Long-range dependence and sea level forecasting*. Springer.

Fraedrich K, Blender R (2003) Scaling of atmosphere and Ocean temperature correlations in observations and climate models. Phys Rev Lett 90(1–4):108501

Gildor H, Tziperman E (2000) Sea ice as the glacial cycles climate switch: role of seasonal and orbital forcing. Paleoceanogrphy 15:605–615

Grant, K. M., Rohling, E. J., Bar-Matthews, M., Ayalon, A., Medina-Elizalde, M., Ramsey, C. B., ... & Roberts, A. P. (2012). Rapid coupling between ice volume and polar temperature over the past 150,000 years. *Nature*, *491*(7426), 744.

Haslett J, Raftery AE (1989) Space-time modelling with long-memory dependence: assessing Ireland's wind power resource. J R Stat Soc 38(1):1–50

Hasselmann K (1976) Stochastic climate models. 1. theory. Tellus 28(6):473–485

Heinz-Otto, P., & Saupe, D. (1988). The science of fractal images.

Hemelrijk, J. (1966). Underlining random variables. Statistica Neerlandica, 20(1), 1-7.

Huang, B., Banzon, V. F., Freeman, E., Lawrimore, J., Liu, W., Peterson, T. C., ... & Zhang, H. M. (2015). Extended reconstructed sea surface temperature version 4 (ERSST. v4). Part I: upgrades and intercomparisons. *Journal of climate*, *28*(3), 911-930.

Huang, B., Thorne, P. W., Banzon, V. F., Boyer, T., Chepurin, G., Lawrimore, J. H., ... & Zhang, H. M. (2017). Extended reconstructed sea surface temperature, version 5 (ERSSTv5): upgrades, validations, and intercomparisons. Journal of Climate, 30(20), 8179-8205.

Hurst, H. E. (1951). Long-term storage capacity of reservoirs. *Trans. Amer. Soc. Civil Eng.*, *116*, 770-799.

Huybers P (2006) Early pleistocene glacial cycles and the integrated summer insolation forcing. Science 313(5786):508–511

Huybers P (2007) Glacial variability over the last two million years: an extended depth derived age model, continuous obliquity pacing, and the Pleistocene progression. Quat Sci Rev 26(1–2):37–55

Huybers P (2011) Combined obliquity and precession pacing of late Pleistocene deglaciations. Nature 480:229–232

Huybers P, Tziperman E (2008) Integrated summer insolation forcing and 40,000 year glacial cycles: the perspective from an icesheet/energy-balance model. Paleoceanography. doi: 10.1029/2007PA001463

Imbrie J (1982) Astronomical theory of the Pleistocene ice ages: a brief historical review. Icarus 50(2–3):408–422

Imbrie J, Berger A, Kutzbach J, Pisias NG, Raymo ME, Shackleton NJ et al (1993) On the structure and origin of major glaciation cycles 2. The 100,000 year cycle. Paleoceangraphy 8:699–735

IPCC, 2013: Climate Change 2013: The Physical Science Basis. Contribution of Working Group I to the Fifth Assessment Report of the Intergovernmental Panel on Climate Change [Stocker, T.F., D. Qin, G.-K. Plattner, M. Tignor, S.K. Allen, J. Boschung, A. Nauels, Y. Xia, V. Bex and P.M. Midgley (eds.)]. Cambridge University Press, Cambridge, United Kingdom and New York, NY, USA, 1535 pp

Jevrejeva, S., Grinsted, A., Moore, J. C., & Holgate, S. (2006). Nonlinear trends and multiyear cycles in sea level records. *Journal of Geophysical Research: Oceans*, *111*(C9).

Jevrejeva, S., Moore, J. C., Grinsted, A., Matthews, A. P., & Spada, G. (2014). Trends and acceleration in global and regional sea levels since 1807. *Global and Planetary Change*, *113*, 11-22.

Kawamura K, Parrenin F, Lisiecki L, Uemura R, Vimeux F, Severinghaus JP, Hutterli MA et al (2007) Northern Hemisphere forcing of climatic cycles in Antarctica over the past 360,000 years. Nature 448(7156):912–916

Kemp, A. C., Horton, B. P., Donnelly, J. P., Mann, M. E., Vermeer, M., & Rahmstorf, S. (2011). Climate related sea-level variations over the past two millennia. *Proceedings of the National Academy of Sciences*, *108*(27), 11017-11022.

Khaliq MN, Gachon P (2010) Pacific Decadal oscillation climate variability and temporal pattern of winter flows in Northwestern North America. J Hydrometeor 11(4):917–933

Kirk, G. S. (1951). Natural change in Heraclitus. *Mind*, *60*(237), 35-42.

Klemeš, V. (1974). The Hurst phenomenon: A puzzle?. Water Resources Research, 10(4), 675-688.

Kolmogorov, A. N. (1963). On tables of random numbers. Sankhyā: The Indian Journal of Statistics, Series A, 369-376.

Kolmogorov, A. N. (1965). Three approaches to the definition of the concept “quantity of information”. *Problemy peredachi informatsii*, *1*(1), 3-11.

Kominz MA, Pisias NG (1979) Pleistocene climate: deterministic or stochastic? Science 204:171–173

Kominz, M. A., Browning, J. V., Miller, K. G., Sugarman, P. J., Mizintseva, S., & Scotese, C. R. (2008). Late Cretaceous to Miocene sea-level estimates from the New Jersey and Delaware coastal plain coreholes: an error analysis. *Basin Research*, *20*(2), 211-226.

Koutsoyiannis D. (2013b) Encolpion of stochastics: fundamentals of stochastic processes, p 12, Department of Water Resources and Environmental Engineering—National Technical University of Athens, Athens

Koutsoyiannis, D. (2002). The Hurst phenomenon and fractional Gaussian noise made easy. Hydrological Sciences Journal, 47(4), 573-595.

Koutsoyiannis, D. (2010). HESS Opinions" A random walk on water". Hydrology and Earth System Sciences, 14(3), 585-601.

Koutsoyiannis, D. (2011). Hurst-Kolmogorov Dynamics and Uncertainty 1. *JAWRA Journal of the American Water Resources Association*, *47*(3), 481-495.

Koutsoyiannis, D. (2013a). Hydrology and change. *Hydrological Sciences Journal*, *58*(6), 1177-1197.

Koutsoyiannis, D. (2016). Generic and parsimonious stochastic modelling for hydrology and beyond. Hydrological Sciences Journal, 61(2), 225-244.

Koutsoyiannis, D. (2017). Entropy production in stochastics. *Entropy*, *19*(11), 581.

Koutsoyiannis, D., & Montanari, A. (2015). Negligent killing of scientific concepts: the stationarity case. *Hydrological Sciences Journal*, *60*(7-8), 1174-1183.

Koutsoyiannis, D., Dimitriadis, P., Lombardo, F., & Stevens, S. (2018). From fractals to stochastics: Seeking theoretical consistency in analysis of geophysical data. In *Advances in Nonlinear Geosciences* (pp. 237-278). Springer, Cham.

Laplace, P. S. (2012). *Pierre-Simon Laplace Philosophical Essay on Probabilities: Translated from the fifth French edition of 1825 With Notes by the Translator* (Vol. 13). Springer Science & Business Media.

Leatherman, S. P., Zhang, K., & Douglas, B. C. (2000). Sea level rise shown to drive coastal erosion. *Eos, Transactions American Geophysical Union*, *81*(6), 55-57.

Li, J., Xie, S. P., Cook, E. R., Morales, M. S., Christie, D. A., Johnson, N. C., ... & Fang, K. (2013). El Niño modulations over the past seven centuries. *Nature Climate Change*, *3*(9), 822.

Lieb, I. C. (1991). *Past, present, and future: a philosophical essay about time*. University of Illinois Press.

Liu H-S, Chao BF (1998) Wavelet spectral analysis of the Earth's orbital variations and Paleoclimatic cycles. J Atmos Sci 55(2):227–236

Liu Z, Cleveland L, Herbert T (2007) Early onset and origin of 100-kyr cycles in Pleistocene tropical SST records. Earth Planet Sci Lett 265:703–715

Liu, W., Huang, B., Thorne, P. W., Banzon, V. F., Zhang, H. M., Freeman, E., ... & Woodruff, S. D. (2015). Extended reconstructed sea surface temperature version 4 (ERSST. v4): Part II. Parametric and structural uncertainty estimations. *Journal of Climate*, *28*(3), 931-951.

Loehle, C. (2018). The epistemological status of general circulation models. *Climate Dynamics*, *50*(5-6), 1719-1731.

Lourens LJ, Becker J, Bintanja R, Hilgen FJ, Tuenter E, van de Wal RS, Ziegler M (2010) Linear and non-linear response of late Neogene glacial cycles to obliquity forcing and implications for the Milankovitch theory. Quat Sci Rev 29(1–2):352–365

Mackey, M. C. (1992). Time's arrow. *The origins of thermodynamic behavior*.

Mandelbrot, B. (1965). Une classe de processus stochastiques homothétiques a soi: application à la loi climatologique de H. E. Hurst. *Comptes rendus hebdomadaires des seances de l academie des sciences*, *260*(12), 3274-+.

Marcos, M., Marzeion, B., Dangendorf, S., Slangen, A. B., Palanisamy, H., & Fenoglio-Marc, L. (2017). Internal variability versus anthropogenic forcing on sea level and its components. *Surveys in Geophysics*, *38*(1), 329-348.

Markonis, Y., & Koutsoyiannis, D. (2013). Climatic variability over time scales spanning nine orders of magnitude: Connecting Milankovitch cycles with Hurst–Kolmogorov dynamics. *Surveys in Geophysics*, *34*(2), 181-207.

McGregor, S., Timmermann, A., & Timm, O. (2010). A unified proxy for ENSO and PDO variability since 1650. *Climate of the Past*, *6*(1), 1-17.

Milankovitch M (1941) Kanon der Erdbestrahlung und seine Andwendung auf das Eiszeitenproblem. Royal Serbian Academy Special Publication,133, Belgrade [English version published by the Israel Program for Scientific Translations, Jerusalem, 1969.]

Miller, K. G., Kominz, M. A., Browning, J. V., Wright, J. D., Mountain, G. S., Katz, M. E., ... & Pekar, S. F. (2005). The Phanerozoic record of global sea-level change. *science*, *310*(5752), 1293-1298.

Miller, K. G., MouNtaiN, G. S., WriGht, J. D., & BroWNiNG, J. V. (2011). A 180-million-year record of sea level and ice volume variations from continental margin and deep-sea isotopic records. *Oceanography*, *24*(2), 40-53.

Milly, P. C. D., Betancourt, J., Falkenmark, M., Hirsch, R. M., Kundzewicz, Z. W., Lettenmaier, D. P., & Stouffer, R. J. (2008). Stationarity is dead: Whither water management?. *Science*, *319*(5863), 573-574.

Monetti, R. A., Havlin, S., & Bunde, A. (2003). Long-term persistence in the sea surface temperature fluctuations. Physica A: Statistical Mechanics and its Applications, 320, 581-589.

Montanari, A., & Koutsoyiannis, D. (2014). Modeling and mitigating natural hazards: Stationarity is immortal!. *Water Resources Research*, *50*(12), 9748-9756.

Montanari, A., Rosso, R., & Taqqu, M. S. (1997). Fractionally differenced ARIMA models applied to hydrologic time series: Identification, estimation, and simulation. *Water resources research*, *33*(5), 1035-1044.

Moschos, E., Manou, G., Dimitriadis, P., Afentoulis, V., Koutsoyiannis, D., & Tsoukala, V. K. (2017a). Harnessing wind and wave resources for a Hybrid Renewable Energy System in remote islands: a combined stochastic and deterministic approach. *Energy Procedia*, *125*, 415-424.

Moschos, E., Manou, G., Georganta, X., Dimitriadis, P., Iliopoulou, T., Tyralis, H., ... & Tsoukala, V. (2017b). Investigation of the stochastic nature of wave processes for renewable resources management: a pilot application in a remote island in the Aegean sea. *European Geosciences Union General Assembly 2017, Geophysical Research Abstracts*, *19*.

Moy, C. M., Seltzer, G. O., Rodbell, D. T., & Anderson, D. M. (2002). Variability of El Niño/Southern Oscillation activity at millennial timescales during the Holocene epoch. *Nature*, *420*(6912), 162.

Mpitsakis E (2003), Pathways of Dialectics, Agra

Muller RA, MacDonald GJ (2000) Ice ages and astronomical causes. Springer Praxis, Chichester

Naish T, Powell R, Levy R, Wilson G et al (2009) Obliquity-paced Pliocene West Antarctic ice sheet oscillations. Nature 458(7236):322–328

Paillard D (1998) The timing of Pleistocene glaciations from a simple multiple-state climate model. Nature 391(6665):378–381

Paillard D (2010) Climate and the orbital parameters of the Earth. Comptes Rendus Geosci 342(4–5):273–285

Papadopoulos, V., & Giovanis, D. G. (2017). *Stochastic Finite Element Methods: An Introduction*. Springer.

Papoulis, A., & Pillai, S. U. (1991). Random Variables and Stochastic Processes. McGraw Hill.

Pappas, C., Mahecha, M. D., Frank, D. C., Babst, F., & Koutsoyiannis, D. (2017). Ecosystem functioning is enveloped by hydrometeorological variability. Nature ecology & evolution, 1(9), 1263.

Pelletier J (2003) Coherence resonance and ice ages. J Geophys Res. doi: 10.1029/2002JD003120

Pettersen EL, Larsen SE (1978) Statistical study of a composite isotopic, paleotemperature series from the last 700,000 years. Tellus 30:193–200

Pisias NG, Moore TC (1981) The evolution of Pleistocene climate: a time series approach. Earth Planet Sci Lett 52:450–458

Prigogine, I., & Stengers, I. (1985). Order out of Chaos.

Prigogine, I., & Stengers, I. (1997). The end of certainty. Simon and Schuster.

Rhein, M. A., Rintoul, S. R., Aoki, S., Campos, E., Chambers, D., Feely, R. A., ... & Mauritzen, C. (2013). Observations: ocean. *Climate change*, 255-315.

Rial JA (1999) Pacemaking the Ice Ages by frequency Modulation of Earth's orbital eccentricity. Science 285(5427):564–568

Roe G (2006) In defense of Milankovitch. Geophys Res Lett. doi: 10.1029/2006GL027817

Ropelewski, C. F., & Jones, P. D. (1987). An extension of the Tahiti–Darwin southern oscillation index. *Monthly Weather Review*, *115*(9), 2161-2165.

Saltzman B (1982) Stochastically-driven climatic fluctuations in the sea-ice, ocean temperature, CO2, feedback system. Tellus 34:97–112

Siddall, M., Rohling, E. J., Almogi-Labin, A., Hemleben, C., Meischner, D., Schmelzer, I., & Smeed, D. A. (2003). Sea-level fluctuations during the last glacial cycle. *Nature*, *423*(6942), 853.

Smith, S., & Lasdon, L. (1992). Solving large sparse nonlinear programs using GRG. *ORSA Journal on Computing*, *4*(1), 2-15.

Spratt, R. M., & Lisiecki, L. E. (2016). A Late Pleistocene sea level stack. *Climate of the Past*, *12*(4), 1079.

Stephenson DB, Pavan V, Bojariu R (2000) Is the North Atlantic Oscillation a random walk? Int J Climatol 20:1–18

Sutcliffe, J., Hurst, S., Awadallah, A. G., Brown, E., & Hamed, K. (2016). Harold Edwin Hurst: the Nile and Egypt, past and future. *Hydrological sciences journal*, *61*(9), 1557-1570.

Suwa M, Bender ML (2008) Chronology of the Vostok ice core constrained by O2/N2 ratios of occluded air, and its implication for the Vostok climate records. Quat Sci Rev 27:11–12

Theodoratos, N. (2012). Entropy: Uncertainty in Hydrology and Nature (Master's thesis).

Tziperman E, Raymo M, Huybers P, Wunsch C (2006) Consequences of pacing the Pleistocene 100 kyr ice ages by nonlinear phase locking to Milankovitch forcing. Paleoceanogrphy. doi: 10.1029/2005PA001241

Waelbroeck, C., Labeyrie, L., Michel, E., Duplessy, J. C., McManus, J. F., Lambeck, K., ... & Labracherie, M. (2002). Sea-level and deep water temperature changes derived from benthic foraminifera isotopic records. *Quaternary Science Reviews*, *21*(1-3), 295-305.

Wang, G., & Tsonis, A. A. (2008). On the variability of ENSO at millennial timescales. *Geophysical Research Letters*, *35*(17).

Winograd IJ, Coplen TB, Landwehr JM, Riggs AC, Ludwig KR, Szabo BJ, Kolesar PT et al (1992) Continuous 500,000-Year climate record from Vein Calcite in Devils Hole Nevada. Science 258(5080):255–260

Wunsch C (2004) Quantitative estimate of the Milankovitch-forced contribution to observed quaternary climate change. Quat Sci Rev 23:1001–1012